A HISTONE METHYLATION-MAPK SIGNALING AXIS DRIVES DURABLE EPITHELIAL-MESENCHYMAL TRANSITION IN HYPOXIC PANCREAS CANCER

Brooke A. Brown[1], Paul J. Myers[1], Sara J. Adair[2], Jason R. Pitarresi[3], Shiv K. Sah-Teli[4], Logan A. Campbell[5], William S. Hart[1], Michelle C. Barbeau[6], Kelsey Leong[7], Nicholas Seyler[1], William Kane[2], Kyoung Eun Lee[8], Edward Stelow[9], Marieke Jones[10], M. Celeste Simon[11,12], Peppi Koivunen[4], Todd W. Bauer[2], Ben Z. Stanger[3], Matthew J. Lazzara[1,5]

[1] Department of Chemical Engineering, University of Virginia, Charlottesville, VA 22903, USA,
[2] Department of Surgery, University of Virginia, Charlottesville, VA 22903, USA
[3] Department of Medicine, University of Pennsylvania, Philadelphia, PA 19104, USA
[4] Faculty of Biochemistry and Molecular Medicine, Biocenter Oulu, University of Oulu, Oulu, FIN-90014, Finland
[5] Department of Biomedical Engineering, University of Virginia, Charlottesville, VA 22903, USA
[6] Biomedical Sciences, University of Virginia, Charlottesville, VA 22903, USA
[7] Engineering Science, University of Virginia, Charlottesville, VA 22903, USA
[8] Department of Pharmacology, University of Michigan, Ann Arbor, MI 48109, USA
[9] Department of Pathology, University of Virginia, Charlottesville, VA 22903, USA
[10] Claude Moore Health Sciences Library, University of Virginia, Charlottesville, VA 22903, USA
[11] Abramson Family Cancer Research Institute, University of Pennsylvania, Philadelphia, PA 19104, USA,
[12] Department of Cell and Developmental Biology, University of Pennsylvania, Philadelphia, PA 19104, USA

Running Title: Hypoxia Drives EMT in Pancreas Cancer

Keywords: extracellular signal-regulated kinases, JUN kinase, hypoxia-inducible factors, E-cadherin, vimentin, PP2A, PP2C

Abbreviations: Clinical Proteomic Tumor Analysis Consortium (CPTAC); epithelial-mesenchymal transition (EMT); gene set variation analysis (GSVA); Kyoto Encyclopedia of Genes and Genomes (KEGG); *Kras*$^{LSL\text{-}G12D}$, p53$^{LSL\text{-}R172H}$, Pdx1-Cre, Rosa26$^{LSL\text{-}YFP}$ (KPCY); mitogen-activated protein kinase (MAPK); pancreatic ductal adenocarcinoma (PDAC); patient-derived xenograft (PDX); The Cancer Genome Atlas (TCGA)

Conflicts of interest: The authors declare no conflicts of interest.

Corresponding Author:
Matthew J. Lazzara
385 McCormick Road
Charlottesville, VA 22903
Phone: 434-243-9767
E-mail: mlazzara@virginia.edu

ABSTRACT

The tumor microenvironment in pancreatic ductal adenocarcinoma (PDAC) plays a key role in tumor progression and response to therapy. The dense PDAC stroma causes hypovascularity, which leads to hypoxia. Here, we showed that hypoxia drives long-lasting epithelial-mesenchymal transition (EMT) in PDAC primarily through a positive-feedback histone methylation-MAPK signaling axis. Transformed cells preferentially underwent EMT in hypoxic tumor regions in multiple model systems. Hypoxia drove a cell-autonomous EMT in PDAC cells which, unlike EMT in response to growth factors, could last for weeks. Furthermore, hypoxia reduced histone demethylase KDM2A activity, suppressed PP2 family phosphatase expression, and activated MAPKs to post-translationally stabilize histone methyltransferase NSD2, leading to an H3K36me2-dependent EMT in which hypoxia-inducible factors played only a supporting role. Hypoxia-driven EMT could be antagonized *in vivo* by combinations of MAPK inhibitors. Collectively, these results suggest hypoxia promotes durable EMT in PDAC by inducing a histone methylation-MAPK axis that can be effectively targeted with multi-drug therapies, providing a potential strategy for overcoming chemoresistance.

STATEMENT OF SIGNIFICANCE

Integrated regulation of histone methylation and MAPK signaling by the low-oxygen environment of pancreatic cancer drives long-lasting EMT that promotes chemoresistance and shortens patient survival and that can be pharmacologically inhibited.

INTRODUCTION

The pancreatic ductal adenocarcinoma (PDAC) microenvironment exerts complex regulation of tumor progression and response to therapy. A well described feature of the PDAC stroma is its characteristic hypovascularity, which gives rise to low-oxygen subdomains (1,2). Hypoxic regions are found in most human PDAC, with oxygen tensions as low as 0.4% compared to 6.8% in adjacent normal tissue (1). Evidence of hypoxia is found at the pancreatic intraepithelial neoplasia (PanIN) stage, and sparse mature vasculature or pronounced hypoxia signatures portend shorter patient survival (2-4). Hypovascularity limits tumor access to systemic therapies and immune cells (2) and correlates with spontaneous metastasis (5). Hypoxia is also a purported driver of epithelial-mesenchymal transition (EMT) (6,7), which occurs as early as the late PanIN stage and is linked to chemoresistance and poor differentiation (8,9). All common PDAC classification systems identify an especially aggressive subtype enriched for mesenchymal characteristics (10-13).

Cytokines including transforming growth factor β (TGFβ), activin-A, and hepatocyte growth factor (HGF) are the best known EMT drivers (14,15). Beyond the ability of TGFβ to induce expression of EMT transcription factors, complete TGFβ-mediated EMT in PDAC cells also requires H3K36 dimethylation mediated by loss of histone lysine demethylase KDM2A and augmented expression of histone methyltransferase NSD2 (16). Hypoxia also promotes histone methylation (17), but the impact on EMT is unexplored. KDM5A and KDM6A are markedly inactivated by low oxygen (18,19), raising the possibility of an entirely intracellular mechanism for EMT in hypoxia.

Direct mechanistic evidence for hypoxia-driven EMT in PDAC is limited. Hypoxia-inducible factors (HIFs) may participate by driving *Twist* expression (6) or Wnt/β-catenin crosstalk (7), and *HIF1A* expression correlates with EMT transcriptomic signatures (20). The connection between hypoxia and specific EMT-promoting signaling pathways is largely unexplored. MAPKs are critical regulators of growth factor-driven EMT (14,21), but the potential

relevance of MAPKs in hypoxic PDAC cells and tumors for EMT has not been thoroughly investigated.

Here, we demonstrate that hypoxia promotes a *bona fide* EMT in PDAC via an integrated histone methylation and MAPK signaling mechanism. Human patient data show that the relationship between low oxygen and PDAC EMT is so typical that statistically significant relationships between EMT and hypoxia gene signatures exist. In mouse and cell culture models, hypoxia-mediated EMT occurs, can proceed in cell-autonomous fashion, and is more durable than growth factor-mediated EMT. The identification of MAPK signaling as indispensable for hypoxia-mediated EMT nominates specific targeted inhibitors for combination therapy approaches that could promote PDAC chemoresponse.

MATERIALS & METHODS

Data Analytics and Computational Modeling

Software and pre-processing of published publicly available data

R version 4.1.2 was used for analysis. See **Supp Table S1** for details on software packages used. See *Data Availability* for information on how data were obtained. For CPTAC proteomics, imputation was performed for proteins with non-missing values in ≥ 50% of samples using *DreamAI*. TCGA PAAD RNA-seq gene expression data were converted from $\log_2$(RSEM+1) normalized counts to transcripts per million (TPM) and then to $\log_2$(TPM+1). For TCGA PAAD phenotype and survival data, only PDAC tumors were retained (150 tumors), based on histological annotations.

Gene sets and signatures

Pan-cancer EMT (pcEMT) (22) or HIF target (23) signatures were used for most clustering. Gene sets from the Molecular Signatures Database and Kyoto Encyclopedia of

Genes and Genomes (KEGG) were accessed in R using *msigdbr* and *clusterProfiler*, respectively.

Clustering

Non-negative matrix factorization (NMF) of bulk tumor data from TCGA and CPTAC was performed with expression data for all available genes or proteins, respectively, based on the pcEMT signature using the *NMF* package. For CPTAC, data were used with imputation. Optimal NMF factorization rank *k* was selected as discussed in Supplementary Data. scRNA-seq data (24) was clustered through sequential 2D UMAP projection using pcEMT mesenchymal gene expression data (*umap* R package, nearest neighbors setting of 30, minimum distance of 0.01) followed by consensus clustering (*ConsensusClusterPlus* using Euclidean distance, Ward's linkage for subsampling and linkage method, and partitioning around medoids (PAM) algorithm).

Gene set enrichment and pathway overdispersion analysis

Gene set variation analysis (GSVA) was used to calculate enrichment scores using CPTAC PDAC global proteome and TCGA PAAD RNA-seq data (*GSVA* R package). For CPTAC data, global proteome data were used without imputation. For TCGA PAAD data, $\log_2$(TPM+1) expression values were used. Pathway and gene set overdispersion analysis (Pagoda2) was used to calculate gene set enrichment scores for ductal cell scRNA-seq data (24) using *Pagoda2*.

Overrepresentation analysis

Gene-equivalent protein phosphorylation data (all phosphosites, as provided by CPTAC) were filtered to retain kinases (358). Spearman rank correlation coefficients were calculated for kinase phosphorylation levels and Hallmark Hypoxia GSVA scores computed from CPTAC global proteomics. KEGG pathway overrepresentation analysis was then performed on

positively and significantly ($p < 0.05$) correlated phospho-kinases using *clusterProfiler*. Only the available kinases in CPTAC phosphoproteomics data were used for testing overrepresentation. *p* values were adjusted for multiple comparisons by controlling the false discovery rate. Spearman correlations and *p* values were calculated using *Hmisc*.

Statistical analyses and data visualization using R

ggstatsplot was used to perform Mann-Whitney U and Kruskal-Wallis tests, and the *survival* and *survminer* packages were used for log-rank test *p* values and survival curves, respectively. *ggplot2*, *tidyHeatmap*, *ComplexHeatmap* and *cowplot* were used for figures. UpSet plots were created using *ggupset*.

Additional computational methods information

Additional computational methods references are provided in Supplementary Data. Information on R packages is provided in **Supp Table S1**. The KEGG signaling pathways used for analyses are listed in **Supp Table S2**.

Experimental Methods

Patient-derived xenografts

PDAC tumor sample MAD12-395 was generated from a human pathology specimen coordinated through the UVA Biorepository and Tissue Research Facility (25). Tumors were passaged in mice, sewn orthotopically into 6-7-week-old female athymic nude mice (Envigo, Indianapolis, IN), and allowed to grow for 6 weeks until palpable. Dosing with inhibitors is described in Supplementary Data.

Autochthonous models and subcutaneous tumors using KPCY cell lines

For autochthonous studies, female and male *Kras*$^{LSL\text{-}G12D}$*, p53*$^{LSL\text{-}R172H}$*, Pdx1-Cre, Rosa26*$^{LSL\text{-}YFP}$ (KPCY) mice (8) were used. Mice were palpated and examined for morbidity twice per week. For subcutaneous tumors, female C57BL/6J (stock no. 000664) or NOD.SCID (stock no. 001303) mice were obtained from The Jackson Laboratory. C57BL/6J (7160c2) or mixed genetic background (PD7591) KPCY cell lines were previously described (9). 2×10^5 cells were injected subcutaneously and grew for 2-6 weeks, with 6 weeks used unless noted.

HPAF-II hypoxia fate-mapping orthotopic tumors

HPAF-II cells were engineered with a fate mapping system that enables an irreversible switch from DsRed to GFP expression in hypoxia (26) (Danielle Gilkes, Johns Hopkins). Cell engineering and clonal selection are described in Supplementary Data. To create tumors, 1×10^6 hypoxia fate-mapping HPAF-II cells were injected orthotopically in 8 week-old male athymic nude mice (Envigo, Indianapolis, IN). Mice were sacrificed 5 weeks later. Animal studies and procedures were approved by the University of Virginia Institutional Animal Care and Use Committee. Following sacrifice, tumor pieces were dissociated on ice followed by flow sorting, as described in Supplementary Data.

Detecting hypoxia in tumors

For all mouse tumor studies probing for hypoxia, pimonidazole was injected (IP, 60 mg/kg; Hypoxyprobe, catalog no. HP7-100) 90 min prior to tumor harvest.

Pathologic assessment of human tumors

Tumors were fixed in zinc-buffered formalin for 24 hr and paraffin-embedded. H&E staining was performed, and a board-certified pathologist (E.S.) assessed differentiation as “well”, “moderate”, or “poor”.

Cell culture

HPAF-II cells (Carl June, University of Pennsylvania) and PDX-derived cell lines (25) were maintained in RPMI. MiaPaca2 cells (Paolo Provenzano, University of Minnesota) were maintained in DMEM. Murine KPCY cells derived from *Kras*$^{LSL\text{-}G12D}$*, p53*$^{LSL\text{-}R172H}$*, Pdx1-Cre, Rosa26*$^{LSL\text{-}YFP}$ mice (2838c3, 6499c4, 6556c6, and 7160c2; all clonal) or *Kras*$^{LSL\text{-}G12D}$, *p53*$^{loxP/+}$, *Pdx1-Cre*, *Rosa26*$^{LSL\text{-}YFP}$ mice (PD798 and PD7591) were maintained in DMEM + GlutaMAX. Media were supplemented with 10% FBS, 1 mM L-glutamine, 100 units/mL penicillin, and 100 µg/mL streptomycin. Murine cell media was also supplemented with 8.66 µg/mL gentamicin. Mycoplasma testing of HPAF-II and PDX cell line stocks was done using the MycoAlert PLUS Detection Kit (Lonza) (July-October 2020). HPAF-II cells were authenticated by the Genetic Resources Core Facility at Johns Hopkins University by short tandem repeat profiling (February 2022). Cells were used within 15 passages of thawing frozen vials. Cells were maintained at 5% CO_2 and 37ºC in a Thermo Scientific Forma Steri-Cycle i160 incubator (21% O_2) or Tri-Gas Steri-Cycle i160 (1% or 7% O_2). For hypoxia experiments, cells were moved to 1% O_2 16 hr after plating, and medium was changed after 72 hr, or every 48 hr when growth factors or inhibitors were used. Cells were treated with inhibitors immediately prior to hypoxic culture.

Fluorescence microscopy (cell culture and tissues) and automated image analysis

Slides were imaged on a Zeiss Axiovert Observer.Z1 fluorescence microscope, using a 10, 20, or 40× objective and ZEN software. Comparisons used identical exposure times and image settings. For each replicate coverslip, four frames were taken randomly, and at least 1000 cells were quantified. For immunohistochemistry, ≥ 8 frames per tumor section were taken. CellProfiler v3.1.9 (Broad Institute) (27) was used to quantify signal intensity and localization. See Supplementary Data for additional details.

Statistical analyses

Graphpad Prism 9 for macOS was used for statistical analyses. Vimentin/E-cadherin linear least squares regression was performed without weighting with F test comparison to a line of zero slope. Cell scatter logistic least squares regressions were performed with F test comparison between 21% and 1% O_2. For two-way ANOVA, Tukey's multiple comparisons or Sidak's multiple comparisons tests were used when considering all conditions or only specific conditions, respectively. For single-cell protein measurements, a mixed-effects model was used where the number of biological replicates taken as the *n* value and individual cells were treated as repeated measurements within biological replicates.

Additional experimental methods information

Additional information on methods and reagents, including methodological references, are in the Supplementary Data. Primer sequences for quantitative real-time PCR are provided in **Supp Table S3**.

Ethics

All animal work conformed to standards of good research practice, and animals were maintained in compliance with NIH guidelines. For autochthonous and subcutaneous tumor models, experiments were approved by the University of Pennsylvania Institutional Animal Care and Use Committee. PDX studies in mice were approved by the UVA Institutional Animal Care and Use Committee. Collection of human PDAC specimens was performed with approval of the Institutional Review Board at the University of Virginia in coordination with the Biorepository and Tissue Research Facility. All patients provided written informed consent for participation.

Data Availability

The data generated in this study are publicly available via the Gene Expression Omnibus dataset GSE252909. All other raw data are available upon request from the corresponding author. CPTAC PDAC Discovery Study clinical and histology data were obtained from the publication (4). Proteomics data were downloaded from the LinkedOmics data portal. TCGA PAAD RNA-seq gene expression data (data set ID: TCGA.PAAD.sampleMap/HiSeqV2; version: 2017-10-13) were downloaded from the UCSC Xena Browser. TCGA PAAD phenotype and survival data were also downloaded from UCSC Xena. Annotated, pre-processed PDAC scRNA-seq data (24) were provided by Dr. David Tuveson (Cold Spring Harbor Laboratory). Links to data repositories are provided in **Supp Table S1**. Code for the analysis of publicly available data is available at: https://github.com/lazzaralab/Brown-et-al_PDAC-hypoxia-EMT.

RESULTS

EMT correlates with hypoxia in human PDAC.

We first investigated a relationship between EMT and hypoxia in human PDAC using CPTAC mass spectrometry (4). Tumor clustering based on a pan-cancer EMT (pcEMT) signature (22) identified mesenchymal-high (M-high) and -low (M-low) groups **(Figure 1A)**. pcEMT was used because, unlike PDAC subtype signatures (10,11,13), it includes many typical EMT genes **(Supp Figure S1A,B)**, while also being useful for predicting disease-free survival **(Figure 1B)**. GSVA Hallmark Hypoxia enrichment scores were higher for M-high tumors **(Figure 1C)**. Importantly, only *COL5A1* is shared between Hallmark Hypoxia and pcEMT **(Supp Figure S1C)**, minimizing concerns about spurious correlations. High stromal tumor content (28) raises a potential concern for bulk analyses, but the mesenchymal-hypoxic relationship was preserved even when controlling for that issue **(Figure 1D)**. Repeating the analysis using a HIF target gene signature with no pcEMT overlap (23) also demonstrated that EMT preferentially occurs in hypoxic tumors **(Supp Figure S2A,B)**. We note that hypoxia was predictive of poor survival in the CPTAC PDAC cohort (4), and the mesenchymal pcEMT signature is enriched in hypoxic

CPTAC study tumors **(Supp Figure S2C)**. Despite little overlap between pcEMT and PDAC subtype signatures, M-high tumors largely align with Collisson quasi-mesenchymal, Moffitt basal-like, and Bailey squamous subtypes **(Figure 1A, Supp Figure S2D)**. Quasi-mesenchymal, basal-like, or squamous tumors are also enriched in Hallmark Hypoxia and HIF signatures **(Supp Figure S1D, Supp Figure S2E,F)**. Similar findings were obtained using TCGA RNA-sequencing **(Supp Figure S3A-G)**. Enrichment for hypoxia transcripts was predictive of lower disease-specific survival **(Supp Figure S3H)**, consistent with CPTAC PDAC study conclusions (4).

To study ductal cells specifically, we analyzed single-cell RNA-sequencing (scRNA-seq) from six human PDAC tumors (24) via two-dimensional UMAP and consensus clustering **(Figure 1E)**. Two groups emerged with markedly different mesenchymal gene expression **(Figure 1F)**. Hallmark Hypoxia **(Figure 1G)** and HIF target **(Supp Figure S4A)** signatures were significantly enriched in more mesenchymal cells. Ductal cells from a *Kras*$^{+/LSL\text{-}G12D}$, *Trp53*$^{+/LSL\text{-}R172H}$, *Pdx1-Cre* mouse model (24) exhibited similar relationships **(Supp Figure S4B-E)**. Thus, hypoxia and EMT are correlated in PDAC tumors.

Hypoxia promotes EMT in multiple PDAC model systems.

To explore the possibility of cell-autonomous hypoxia-mediated EMT, HPAF-II human PDAC cells were cultured for 120 hr in 21%, 7%, or 1% O_2. HPAF-II cells are baseline epithelial (29) and harbor three prevalent PDAC mutations (*Kras*^{G12D}, *TP53*, and *CDKN2A*) (30). Selected oxygen concentrations align with conditions in conventional cell culture (21%), normal pancreas (6.8%), and PDAC tumors (0.4%) (1,31). E-cadherin loss was robust by 120 hr in hypoxic culture, but hypoxia-inducible factor (HIF)-1α expression peaked at earlier times **(Supp Figure S5A,B)**. Early E-cadherin increases likely resulted from establishment of cell-cell contacts. At 1% O_2, ~25-30% of HPAF-II cells underwent EMT, based on increased vimentin expression and associated E-cadherin losses **(Figure 2A)**. Meaningful differences were not observed between

21% and 7% O_2, so subsequent experiments compared 21% and 1% O_2. For 1% O_2, E-cadherin and vimentin were inversely related **(Figure 2A)**, as expected, and vimentin was subsequently used as the primary EMT marker.

Other observations also suggested a *bona fide* EMT in hypoxia. In 1% O_2, GFP-expressing HPAF-II cell exhibited reduced cluster circularity and increased scatter **(Figure 2B)**, consistent with responses to growth factors (21). HPAF-II cells in 1% O_2 also exhibited increased expression of hypoxia markers *PGK1* and *SLC2A1* and mesenchymal transcripts *VIM*, *SNAI1*, and *TWIST1*, and decreased *CDH1* expression **(Figure 2C)**. Decreased *HIF1A* expression is consistent with prior reports (32).

PDX- and murine tumor-derived cells were also tested for cell-autonomous hypoxia-mediated EMT. For PDXs, we first confirmed by RNA-sequencing and tumor grading that mesenchymal genes were enriched in cells from poorly differentiated tumors **(Supp Figure S5C,D)**. Based on screening for epithelial traits by tissue microarray **(Supp Figure S5E-G)**, six PDX cell lines were evaluated. Cells from PDXs 366, 395, and 449 exhibited increased scatter or loss of epithelial morphology in 1% O_2 **(Supp Figure S5H)**. PDX 395 cells were studied further because they exhibited anticipated E-cadherin and vimentin changes. In pilot screening of six baseline epithelial KPCY cells, every line exhibited increased vimentin positivity in 1% O_2 **(Supp Figure S6A)**. 7160c2 was among those with an obvious morphology change and was used for further studies.

To investigate a hypoxia-EMT correlation *in vivo*, we confirmed the presence of hypoxic tumor regions in a mouse PDAC model using pimonidazole (Hypoxyprobe, HYP). Pilot studies showed abundant HYP tumor staining by six weeks **(Supp Figure S6B)**. Compared to normal mouse pancreas, a PDX tumor exhibited low CD31 endothelial and elevated HYP staining **(Figure 2D)**. CD31-positive capillary beds were non-overlapping with HYP-positive cells **(Figure 2E)**. To assess the EMT-hypoxia relationship, we used orthotopic PDX, KPCY autochthonous, and subcutaneous KPCY cell line models. Human COXIV or YFP was used to identify ductal

cells in PDX or implanted/autochthonous tumors, respectively **(Figure 2F-I, Supp Figure S6C-H)**. Because PDX 395 tumors are devoid of human fibroblasts (33), COXIV+ cells were identified as human ductal cells. In PDX tumors, COXIV+/HYP+ cells were primarily vimentin+ **(Figure 2F)**. Similarly, in KPCY and subcutaneous tumors, more YFP+/HYP+ cells were vimentin+ than were YFP+/HYP- **(Figure 2G,H, Supp Figure S6G)**. In KPCY subcutaneous tumors, YFP+/HYP+ cells exhibited reduced E-cadherin expression **(Figure 2I, Supp Figure S6H)**. Thus, hypoxic tumor regions are enriched for ductal cell EMT.

Hypoxia-driven EMT is more durable than growth factor-driven EMT.

To make a hypoxia comparison against growth factors, we combined TGFβ and HGF because both potently promote EMT. In HPAF-II cells, growth factors generated more than twice as many vimentin+ cells as hypoxia **(Figure 3A)**. E-cadherin expression was reduced by both growth factors and hypoxia **(Supp Figure S7A)**. By immunofluorescence microscopy, growth factors were again observed to be more potent in HPAF-II cells, but hypoxia and growth factors had comparable effects in PDX and KPCY cells **(Figure 3B)**.

To explore the time scales of mesenchymal persistence for different conditions, HPAF-II cells exposed to growth factors or 1% O_2 were replated in complete medium at 21% O_2. Interestingly, vimentin loss occurred more slowly for once-hypoxic cells than those treated with growth factors **(Figure 3C)**. Similar trends were observed in KPCY and PDX cell lines **(Supp Figure S7B,C)**. Replating KPCY and PDX cells after EMT induction caused a temporary spike in vimentin, potentially related to cytoskeletal adhesions. Despite this effect, more persistent vimentin expression was apparent for hypoxia.

Prolonged vimentin maintenance in once-hypoxic cells suggests a heritable trait. To test this, we quantified nuclei with a morphology indicative of mitosis 120 hr after relief of EMT-induction. The once-hypoxic population contained more actively dividing, vimentin-positive cells than those treated with growth factors, as determined by counting mitotic or Ki67-positive nuclei

(Figure 3D, Supp Figure S7D). Preferential vimentin persistence after hypoxia was still observable five weeks after treatment **(Supp Figure S7E)**.

To explore the implications of durable hypoxia-mediated EMT in tumors, HPAF-II cells were engineered with a HIF-regulated fate-mapping system that stably converts hypoxic cells from DsRed to GFP expression (26). Validation of the clonally selected transductant is described in **Supp Figure S7F**,**G**. Orthotopic tumors formed from the selected clone exhibited more vimentin+/HYP+ tumor cells than vimentin+/HYP- cells **(Supp Figure S7H)**, as expected. Surprisingly, there were equivalent numbers of GFP+/vimentin+ cells that were HYP+ or HYP- **(Figure 3E)**, potentially indicating that cells can maintain a hypoxia-driven mesenchymal state outside hypoxic domains. Five-color confocal imaging revealed similar vimentin positivity for DsRed+ and GFP+ cells **(Supp Figure S7H)**, suggesting that factors other than hypoxia (e.g., cytokines) drove EMT. To test the mesenchymal durability of GFP+ cells, explanted tumors were dissociated and flow-sorted into DsRed+, GFP+, and DsRed+/GFP+ populations, which were subsequently cultured in 21% O_2. Double-positive cells arise due to slow DsRed turnover, and very few collected cells were solely GFP+. 12 days after dissociation, more DsRed+/GFP+ cells were vimentin+ than were DsRed+ cells **(Figure 3F)**. Combined with Figure 3C results, this suggests that hypoxia-mediated EMT contributed substantially to vimentin expression in DsRed+/GFP+ cells.

MAPK and SFK signaling promote hypoxia-mediated EMT and are activated by impaired phosphatase expression.

To identify mechanisms that promote EMT in hypoxia, we first analyzed CPTAC proteomics (4). Reported overall kinase phosphorylation scores were extracted and Spearman rank correlation coefficients with Hallmark Hypoxia enrichment scores were calculated. The kinase list was then pared for an overrepresentation analysis of KEGG signaling pathways **(Supp Table S2)** by retaining kinases whose phosphorylation correlated positively and

significantly ($p < 0.05$) with Hallmark Hypoxia enrichment. The MAPK gene set had the largest number and fraction of phosphokinases present **(Figure 4A, Supp Figure S1E)**.

For scRNA-seq data (24), we developed a linear model of Hallmark Hypoxia enrichment dependence on KEGG signaling ontologies in ductal cells. We used LASSO regression for automatic variable selection, followed by ordinary least squares regression with variable selection by Akaike information criterion (AIC) minimization. Of the 30 KEGG signaling gene sets that were sufficiently overdispersed to obtain Pagoda2 scores, 19 were retained by LASSO, and 16 of these were retained by AIC. The final model was statistically significant and identified MAPK as the most predictive gene set **(Figure 4B)**. Identical analyses of mouse scRNA-seq (24) identified HIF-1 and MAPK signatures as most predictive of hypoxia enrichment **(Supp Figure S8A)**. We pursued MAPKs first based on this and returned to HIFs later.

We tested p38, JNK, and ERK1/2 inhibitors for antagonism of hypoxia-mediated EMT. Concentrations were chosen for their ability to impact EMT without causing cell death. MEK and JNK inhibitors suppressed vimentin and promoted E-cadherin expression in hypoxia **(Figure 4C, Supp Figure S8B,C)**. Surprisingly, p38 inhibition promoted vimentin expression, which could indicate a p38 role in EMT suppression (34). Combined inhibition of MEK and JNK had an additive effect, suggesting pathway cooperation. An additive effect was also seen for protein markers in PDX 395 cells **(Figure 4D)** and transcripts in HPAF-II cells **(Supp Figure S8D)**.

MAPKs play a prominent role in growth factor-driven EMT (21,35), and we compared MAPK induction for growth factors and hypoxia. For growth factors, c-Jun (a common name for the protein encoded by *JUN*), pc-Jun, and pERK abundances were increased by 24 hr and returned to baseline by 120 hr. In hypoxia, elevated c-Jun expression and ERK phosphorylation persisted at 120 hr, with concomitant E-cadherin reduction **(Figure 4E, Supp Figure S8E).** Because c-Jun expression changes were more robustly detected than phosphorylation changes at the latest time, expression was typically used as a JNK activity proxy. This choice is sensible because JNK activity promotes c-Jun expression (36) **(Supp Figure S8F)** and ERK1/2

knockdown does not alter c-Jun abundance **(Supp Figure S8G)**. siRNA-mediated knockdown of ERK1/2 and/or c-Jun **(Supp Fig S8G,H)** or stable shRNA-mediated knockdown of *ERK2* and *JUN* **(Supp Figure S8I-K)** also impeded hypoxia-mediated EMT.

To identify the MAPK signaling driver in hypoxia, two kinase arrays were used **(Supp Figure S9A,B)**. Both detected increased Src family kinase (SFK) phosphorylation. SFK inhibition antagonized nuclear c-Jun accumulation and ERK phosphorylation **(Figure 4F,G)**, consistent with known SFK roles, and antagonized hypoxia-driven EMT **(Figure 4H)**. Although hypoxia promotes TGFβ-dependent EMT in some settings (37), TGFβ receptor I (TGFβRI) inhibition had no effect on hypoxia-mediated EMT in HPAF-II cells **(Supp Figure S9C)**. Furthermore, TGFβ signaling was not nominated by analyses of patient data **(Figure 4A,B)**. A screen for cytokines (Luminex) did not identify any EMT-promoting candidates that were upregulated in hypoxic HPAF-II cells (Supp Figure S9D).

Lacking signaling-initiating cytokine leads, we hypothesized that hypoxia suppresses phosphatase expression and specifically considered protein phosphatase 2A (PP2A) due to its regulation of MAPK and SFK signaling (38). In patient scRNA-seq data (24), transcripts for subunits of PP2A, as well as PP2C and PP1A, were negatively correlated with the HIF gene signature **(Supp Figure S10)**. In HPAF-II cells, transcripts for multiple phosphatase subunits were decreased by hypoxia but not growth factors **(Figure 4I).** Furthermore, PP2A or PP2Cδ inhibition at 21% O_2 promoted vimentin expression **(Figure 4J)** and c-Jun and ERK nuclear accumulation **(Supp Figure S9E-G)**.

We next probed the relevance of MAPK signaling in mouse models. In KPCY and subcutaneous tumors, nuclear c-Jun was elevated in hypoxic YFP+ cells **(Figure 5A,B)**. In PDX tumors, nuclear c-Jun was also more abundant in hypoxic cells, and nuclear c-Jun was found preferentially in vimentin-positive cells **(Figure 5C)**. PDX tumors also exhibited elevated pERK in vimentin-positive cells **(Figure 5D)**. Interestingly, hypoxia-mediated EMT, while durable, was reversible via MEK and JNK inhibition in cell culture **(Figure 5E, Supp Figure S9H,I)**.

To investigate the ability of MAPK antagonism to abrogate EMT *in vivo*, MEK and JNK inhibitors were tested in orthotopic PDX 395 tumors. For both HYP+ and HYP- cells, MEK or JNK inhibition reduced vimentin positivity, but the effect was only significant with combined MEK and JNK inhibition **(Figure 5F, Supp Figure S9J,K)**. Thus, ERK and JNK cooperate to drive EMT in hypoxic tumor cells, and kinase inhibitors can interrupt and reverse this process even in poorly vascularized tissue.

HIFs play a supporting role in hypoxia-driven EMT.

To test the role of HIFs, we utilized RNA interference or gene knockouts. Transient knockdown of *HIF1A* (HIF-1α) and/or *EPAS1* (HIF-2α) in HPAF-II cells antagonized vimentin expression in hypoxia **(Figure 6A, Supp Figure S11A)**. However, there was no significant effect of HIF knockdown on *VIM*, *SNAI1*, or *CDH1* transcripts at 1% O_2 **(Figure 6B)**. Vimentin post-translational regulation (39) could account for the discrepancy, which was also observed with JNK inhibition **(Supp Figure S8D)**. Stable knockdown of both transcripts failed to reduce vimentin expression significantly **(Figure 6C, Supp Figure S11B)**. In tumor sections from a pancreas-specific, *Kras*-mutant *Hif1a*-knockout (*Kras*^{G12D}*Hif1a*^{KO}) mouse (3), we observed an insignificant change in vimentin-positivity in *Hif1a*^{KO} versus *Hif1a*-replete tumors **(Supp Figure S11C)**. Because MAPKs regulate HIF expression (40), we tested the effects of MEK and JNK inhibitors on HIF abundance. Each inhibitor antagonized HIF-1α accumulation, and the combination of inhibitors was even more effective **(Figure 6D)**. *HIF1A* transcripts were unaffected **(Figure 6E)**, pointing to a post-translational stabilization by MAPKs. Collectively, these data suggest that HIFs play a supporting, but not indispensable, role in hypoxia-mediated EMT.

Hypoxia-driven EMT depends on histone methylation.

Due to the durable nature of hypoxia-driven EMT, we hypothesized that epigenetic modifications could be involved. TGFβ-mediated EMT requires histone H3 lysine 36 dimethylation (H3K36me2) and ensuing *Zeb1* and *Snai1* expression (16), and we thus focused on that mark. H3K36me2 abundance was significantly increased in HPAF-II cells treated with growth factors or 1% O_2 **(Figure 7A)**. Furthermore, H3K36me2 persisted longer in once-hypoxic cells than growth factor-treated cells **(Supp Figure S12A)**.

We next investigated effects on the lysine demethylase KDM2A and methyltransferase NSD2, which regulate H3K36me2 (16). Activities of the Jumonji C family lysine demethylases KDM5A and KDM6A are highly oxygen-dependent (18,19). We characterized the oxygen-dependent activity of KDM2A **(Supp Figure S12B-G)** and found a KDM2A-H3K36me2 interaction strength consistent with other demethylase/histone pairs (K_M = 108 ± 12 μM) and an O_2 K_M = 57 ± 17 μM **(Figure 7B,C, Supp Figure S12H)**. While this O_2 K_M is several-fold lower than those for KDM5A and KDM6A (18,19), it clearly falls between oxygen concentrations observed in normal pancreas (1.21-12.05%, or 11.9-118.6 μM) and PDAC tumors (0-0.69%, or 0-6.78 μM) (1,41). Thus, KDM2A activity should be substantially compromised in hypoxic PDAC tissue. Interestingly, *KDM2A* transcripts were slightly elevated by hypoxia **(Supp Figure S12I)**. While KDM2A expression is HIF-1α-dependent in some settings, this relationship was absent in HPAF-II cells **(Supp Figure S12I)**. KPCY cell lines (16) also displayed increased H3K36 dimethylation, accompanied by increased vimentin expression, in hypoxia **(Figure 7D, Supp Figure S12J)**.

We also found that NSD2 expression was augmented at 1% O_2 **(Figure 7E)**. Interestingly, *NSD2* transcripts were partially depleted by hypoxia, consistent with observations in patient scRNA-seq data **(Supp Figure S13A,B)**. Changes in *NSD2* abundance in hypoxia were insensitive to HIF-1α and HIF-2α knockdown or MEK and JNK inhibition **(Supp Figure S13C,D)**. Searching for possible post-translational mechanisms, we noted that dephosphorylation by PP2Cδ promotes NSD2 degradation (42) and recalled that *PPM1D*, which

encodes PP2Cδ, was depleted in hypoxia **(Figure 4I)**. Consistent with the implied mechanism, NSD2 expression was elevated by PP2Cδ inhibition, and to a lesser degree by PP2A inhibition **(Figure 7F)**. While NSD2 knockdown impeded H3K36 dimethylation in response to hypoxia or growth factors, it preferentially antagonized EMT in response to hypoxia **(Figure 7G, Supp Figure S13E)**. Hypoxia-mediated EMT and H3K36 dimethylation were also Nsd2- and Kdm2a-dependent in KPCY cell lines (16) **(Supp Figure S13F,G)**. Previously reported RNA-sequencing of these cell lines (16) reveals that PP2A and PP2C subunits, and dual-specificity phosphatases, were altered by *Kdm2a* or *Nsd2* knockout, providing a mechanistic link between histone methylation and MAPK activation. We further found that MEK and JNK inhibition antagonized H3K36 dimethylation and NSD2 expression in 1% O_2, but that NSD2 expression could be rescued by PP2Cδ co-inhibition **(Figure 7H)**. HIF-1α and/or HIF-2α knockdown also antagonized H3K36 dimethylation in 1% O_2 **(Supp Figure S13H).** Collectively, these results suggest that hypoxia reduces KDM2A activity, suppressing serine/threonine phosphatases and stabilizing NSD2.

DISCUSSION

Our results show that hypoxia and EMT are so typically related in PDAC that statistically significant relationships can be determined from three types of patient data and four mouse models. In the mechanism we propose **(Figure 8)**, hypoxia reduces KDM2A activity, resulting in H3K36 dimethylation and decreased protein phosphatase expression. Loss of phosphatases, such as PP2A, promotes SFK and MAPK signaling, which cooperates with reduced PP2Cδ activity to stabilize NSD2, creating a reinforcing, positive feedback that leads to durable EMT. ERK and JNK also stabilize HIF-1α, which plays a supporting role. Collectively, ERK, JNK, and H3K36me2 promote expression of c-Jun, HIF-1α and other EMT transcription factors.

Uncertainty remains about the rate-limiting step for epithelial reversion after hypoxic cells are returned to a normoxic environment. Previously hypoxic cells revert to an epithelial state

quickly after kinase inhibitors are applied. Thus, one possibility is that hypoxic mesenchymal cells become stuck in a pseudo-equilibrium that can be reversed by severe intervention. That pseudo-equilibrium state may arise preferentially for hypoxia because of the extreme loss of KDM2A activity that occurs. Interestingly, EMT exhibits path-dependent bistable or tristable states (43), but this effect has not previously been reported for hypoxia. MAPK (44) and HIF-1α (45) signaling also exhibit bistability.

Previous work identified MAPK pathways as targets for PDAC combination therapy. MEK/ERK inhibitors have been combined with PD-L1 antibodies (46) and PI3K inhibitors (47), and low-dose “vertical inhibition” of RAF and ERK promotes epithelial characteristics in KRAS-mutant PDAC (48). ERK1/2 inhibitor monotherapy for PDAC is ineffective due to an autophagic response, but combined ERK and autophagy inhibition suppresses tumor growth (49). JNK signaling is activated in PDAC by 5-fluorouracil plus leucovorin (5-FU+LEU) or FOLFOX (5-FU+LEU plus oxaliplatin), and JNK inhibition reduces FOLFOX chemoresistance (50). Our findings motivate pursuing combinations of MAPK inhibitors for antagonism of hypoxia-mediated EMT, which may increase chemoresponse.

Epigenetic changes other than H3K36me2, including histone 3 lysine 4 acetylation (H3K4Ac), H3K4me2, and H3K27me3, regulate EMT genes (51,52). We focused on H3K36me2 given its known role in PDAC EMT (16). Enzymes that modify epigenetic marks are also being tested as drugs targets, with early-phase trials in solid tumors (53). Inhibitors have been identified against methyltransferases (54), the methyltransferase enhancer EZH2 (53), and histone deacetylases (HDAC) (55). HDAC inhibition alone is ineffective in PDAC (56), but combined HDAC and MEK inhibitors hold promise (57). NSD2 inhibitors target the methyl-transferring SET domain are also in development (58).

While the hypoxic NSD2 accumulation we observed was post-translationally regulated, others have reported HIF-1α-dependent *NSD2* accumulation in melanoma cells (59). Thus, different mechanisms may regulate NSD2 abundance in hypoxia. Several core HIF-binding sites

(5'-RCGTG-3') (60) exist in the *NSD2* promoter. However, other transcription factors cooperate with HIFs in a tissue- and gene-specific manner (61), which may explain why HIFs do not universally regulate *NSD2* (60). Hypoxia can also regulate NSD2 through downregulation of PP2Cδ, which dephosphorylates and destabilizes NSD2 (42), and through MAPK activity. The latter effect may occur via NSD2 PEST domains, which can slow protein turnover when phosphorylated (62). The online tool ePESTfind reports that NSD2 has two regions (531 – 546 and 615 – 656) with high PEST scores (>5). The online iGPS algorithm (63) with a lenient threshold predicts that JNK and ERK phosphorylate NSD2 threonine 544 and serines 631 and 639.

Hypoxia also promotes metabolic changes that contribute to aggressive disease (64), and metabolic reprogramming can be accompanied by EMT (65). Hypoxia-mediated expression of the mesenchymal protein N-cadherin is glucose- and glutamine-dependent, indicating that glycolytic and glutaminolytic activity influence hypoxia-mediated EMT (66). Further, MEK and JNK are involved in the Warburg effect by interacting with key metabolic regulators in glycolysis (67), and some epigenetic modifiers respond to altered intracellular energy levels (68). Potential metabolic dependencies in the mechanism we elucidated should be explored.

Finally, the durable nature of hypoxia-mediated EMT could make this mechanism especially likely to contribute to metastatic dissemination. At the same time, our finding that hypoxia-driven EMT can persist for weeks may challenge the typical view that a mesenchymal-epithelial transition is required for metastatic outgrowth. Additional work is needed to investigate these issues.

ACKNOWLEDGEMENTS

The authors thank Danielle Gilkes (Johns Hopkins) for the hypoxia fate-mapping plasmids and technical discussions, David Tuveson (Cold Springs Harbor Laboratory) for sharing annotated scRNAseq data, John Tobias (University of Pennsylvania) and Shayn Peirce-Cottler (UVA) for technical discussions, Yi Zhang (Harvard) for creating the *KDM2A* plasmid, Jing-Yi Chen (I-Shou University) for sharing the *KDM2A* plasmid, Kevin Janes (UVA) for the eGFP plasmid, Carl June (University of Pennsylvania) and Paolo Provenzano (University of Minnesota) for cell lines, Robert Norgard (University of Pennsylvania) for assistance providing KPCY tumor sections, Mark Yeager (UVA) for the pFastBac1 plasmid, and CPTAC PDAC Discovery Study senior authors for technical discussions. Figure 8 was created with BioRender.com.

FUNDING

This work was supported by NCI U01 CA243007 (MJL), NSF 1716537 (MJL), NSF 1700687 (MJL), NSF Graduate Research Fellowship 1842490 (BAB), UVA Cancer Training Program T32CA009109, UVA Biomedical Data Sciences Training Program T32LM012416, and UVA Cancer Center Support Grant NCI P30CA044579.

REFERENCES

1. Koong AC, Mehta VK, Le QT, Fisher GA, Terris DJ, Brown JM*, et al.* Pancreatic tumors show high levels of hypoxia. Int J Radiat Oncol Biol Phys **2000**;48:919-22
2. Katsuta E, Qi Q, Peng X, Hochwald SN, Yan L, Takabe K. Pancreatic adenocarcinomas with mature blood vessels have better overall survival. Sci Rep **2019**;9:1310
3. Lee KE, Spata M, Bayne LJ, Buza EL, Durham AC, Allman D*, et al.* Hif1a Deletion Reveals Pro-Neoplastic Function of B Cells in Pancreatic Neoplasia. Cancer Discov **2016**;6:256-69
4. Cao L, Huang C, Cui Zhou D, Hu Y, Lih TM, Savage SR*, et al.* Proteogenomic characterization of pancreatic ductal adenocarcinoma. Cell **2021**;184:5031-52 e26
5. Chang Q, Jurisica I, Do T, Hedley DW. Hypoxia predicts aggressive growth and spontaneous metastasis formation from orthotopically grown primary xenografts of human pancreatic cancer. Cancer Res **2011**;71:3110-20
6. Chen S, Chen JZ, Zhang JQ, Chen HX, Yan ML, Huang L*, et al.* Hypoxia induces TWIST-activated epithelial-mesenchymal transition and proliferation of pancreatic cancer cells in vitro and in nude mice. Cancer Lett **2016**;383:73-84
7. Zhang Q, Lou Y, Zhang J, Fu Q, Wei T, Sun X*, et al.* Hypoxia-inducible factor-2alpha promotes tumor progression and has crosstalk with Wnt/beta-catenin signaling in pancreatic cancer. Mol Cancer **2017**;16:119
8. Rhim AD, Mirek ET, Aiello NM, Maitra A, Bailey JM, McAllister F*, et al.* EMT and dissemination precede pancreatic tumor formation. Cell **2012**;148:349-61
9. Aiello NM, Maddipati R, Norgard RJ, Balli D, Li J, Yuan S*, et al.* EMT Subtype Influences Epithelial Plasticity and Mode of Cell Migration. Dev Cell **2018**;45:681-95 e4
10. Bailey P, Chang DK, Nones K, Johns AL, Patch AM, Gingras MC*, et al.* Genomic analyses identify molecular subtypes of pancreatic cancer. Nature **2016**;531:47-52
11. Collisson EA, Sadanandam A, Olson P, Gibb WJ, Truitt M, Gu S*, et al.* Subtypes of pancreatic ductal adenocarcinoma and their differing responses to therapy. Nat Med **2011**;17:500-3
12. Dijk F, Veenstra VL, Soer EC, Dings MPG, Zhao L, Halfwerk JB*, et al.* Unsupervised class discovery in pancreatic ductal adenocarcinoma reveals cell-intrinsic mesenchymal features and high concordance between existing classification systems. Sci Rep **2020**;10:337
13. Moffitt RA, Marayati R, Flate EL, Volmar KE, Loeza SG, Hoadley KA*, et al.* Virtual microdissection identifies distinct tumor- and stroma-specific subtypes of pancreatic ductal adenocarcinoma. Nat Genet **2015**;47:1168-78
14. Lu W, Kang Y. Epithelial-Mesenchymal Plasticity in Cancer Progression and Metastasis. Dev Cell **2019**;49:361-74
15. Bashir M, Damineni S, Mukherjee G, Kondaiah P. Activin-A signaling promotes epithelial-mesenchymal transition, invasion, and metastatic growth of breast cancer. NPJ Breast Cancer **2015**;1:15007
16. Yuan S, Natesan R, Sanchez-Rivera FJ, Li J, Bhanu NV, Yamazoe T*, et al.* Global Regulation of the Histone Mark H3K36me2 Underlies Epithelial Plasticity and Metastatic Progression. Cancer Discov **2020**;10:854-71
17. Losman JA, Koivunen P, Kaelin WG, Jr. 2-Oxoglutarate-dependent dioxygenases in cancer. Nat Rev Cancer **2020**;20:710-26
18. Chakraborty AA, Laukka T, Myllykoski M, Ringel AE, Booker MA, Tolstorukov MY*, et al.* Histone demethylase KDM6A directly senses oxygen to control chromatin and cell fate. Science **2019**;363:1217-22
19. Batie M, Frost J, Frost M, Wilson JW, Schofield P, Rocha S. Hypoxia induces rapid changes to histone methylation and reprograms chromatin. Science **2019**;363:1222-6

20. Chen B, Li L, Li M, Wang X. HIF1A expression correlates with increased tumor immune and stromal signatures and aggressive phenotypes in human cancers. Cell Oncol (Dordr) **2020**;43:877-88
21. Buonato JM, Lan IS, Lazzara MJ. EGF augments TGFbeta-induced epithelial-mesenchymal transition by promoting SHP2 binding to GAB1. J Cell Sci **2015**;128:3898-909
22. Mak MP, Tong P, Diao L, Cardnell RJ, Gibbons DL, William WN*, et al.* A Patient-Derived, Pan-Cancer EMT Signature Identifies Global Molecular Alterations and Immune Target Enrichment Following Epithelial-to-Mesenchymal Transition. Clin Cancer Res **2016**;22:609-20
23. Li B, Qiu B, Lee DS, Walton ZE, Ochocki JD, Mathew LK*, et al.* Fructose-1,6-bisphosphatase opposes renal carcinoma progression. Nature **2014**;513:251-5
24. Elyada E, Bolisetty M, Laise P, Flynn WF, Courtois ET, Burkhart RA*, et al.* Cross-Species Single-Cell Analysis of Pancreatic Ductal Adenocarcinoma Reveals Antigen-Presenting Cancer-Associated Fibroblasts. Cancer Discov **2019**;9:1102-23
25. Walters DM, Stokes JB, Adair SJ, Stelow EB, Borgman CA, Lowrey BT*, et al.* Clinical, molecular and genetic validation of a murine orthotopic xenograft model of pancreatic adenocarcinoma using fresh human specimens. PLoS One **2013**;8:e77065
26. Godet I, Shin YJ, Ju JA, Ye IC, Wang G, Gilkes DM. Fate-mapping post-hypoxic tumor cells reveals a ROS-resistant phenotype that promotes metastasis. Nat Commun **2019**;10:4862
27. Stirling DR, Swain-Bowden MJ, Lucas AM, Carpenter AE, Cimini BA, Goodman A. CellProfiler 4: improvements in speed, utility and usability. BMC Bioinformatics **2021**;22:433
28. Dhani NC, Serra S, Pintilie M, Schwock J, Xu J, Gallinger S*, et al.* Analysis of the intra- and intertumoral heterogeneity of hypoxia in pancreatic cancer patients receiving the nitroimidazole tracer pimonidazole. Br J Cancer **2015**;113:864-71
29. Rajasekaran SA, Gopal J, Espineda C, Ryazantsev S, Schneeberger EE, Rajasekaran AK. HPAF-II, a cell culture model to study pancreatic epithelial cell structure and function. Pancreas **2004**;29:e77-83
30. Moore PS, Sipos B, Orlandini S, Sorio C, Real FX, Lemoine NR*, et al.* Genetic profile of 22 pancreatic carcinoma cell lines. Analysis of K-ras, p53, p16 and DPC4/Smad4. Virchows Arch **2001**;439:798-802
31. McKeown SR. Defining normoxia, physoxia and hypoxia in tumours-implications for treatment response. Br J Radiol **2014**;87:20130676
32. Lin Q, Cong X, Yun Z. Differential hypoxic regulation of hypoxia-inducible factors 1alpha and 2alpha. Mol Cancer Res **2011**;9:757-65
33. Stokes JB, Adair SJ, Slack-Davis JK, Walters DM, Tilghman RW, Hershey ED*, et al.* Inhibition of focal adhesion kinase by PF-562,271 inhibits the growth and metastasis of pancreatic cancer concomitant with altering the tumor microenvironment. Mol Cancer Ther **2011**;10:2135-45
34. Strippoli R, Benedicto I, Foronda M, Perez-Lozano ML, Sanchez-Perales S, Lopez-Cabrera M*, et al.* p38 maintains E-cadherin expression by modulating TAK1-NF-kappa B during epithelial-to-mesenchymal transition. J Cell Sci **2010**;123:4321-31
35. Buonato JM, Lazzara MJ. ERK1/2 blockade prevents epithelial-mesenchymal transition in lung cancer cells and promotes their sensitivity to EGFR inhibition. Cancer Res **2014**;74:309-19
36. Kayahara M, Wang X, Tournier C. Selective regulation of c-jun gene expression by mitogen-activated protein kinases via the 12-o-tetradecanoylphorbol-13-acetate-responsive element and myocyte enhancer factor 2 binding sites. Mol Cell Biol **2005**;25:3784-92

37. Matsuoka J, Yashiro M, Doi Y, Fuyuhiro Y, Kato Y, Shinto O*, et al.* Hypoxia stimulates the EMT of gastric cancer cells through autocrine TGFbeta signaling. PLoS One **2013**;8:e62310
38. Hu X, Wu X, Xu J, Zhou J, Han X, Guo J. Src kinase up-regulates the ERK cascade through inactivation of protein phosphatase 2A following cerebral ischemia. BMC Neurosci **2009**;10:74
39. Snider NT, Omary MB. Post-translational modifications of intermediate filament proteins: mechanisms and functions. Nat Rev Mol Cell Biol **2014**;15:163-77
40. Furcht CM, Buonato JM, Skuli N, Mathew LK, Munoz Rojas AR, Simon MC*, et al.* Multivariate signaling regulation by SHP2 differentially controls proliferation and therapeutic response in glioma cells. J Cell Sci **2014**;127:3555-67
41. Ast T, Mootha VK. Oxygen and mammalian cell culture: are we repeating the experiment of Dr. Ox? Nat Metab **2019**;1:858-60
42. Lv N, Jin S, Liang Z, Wu X, Kang Y, Su L*, et al.* PP2Cdelta Controls the Differentiation and Function of Dendritic Cells Through Regulating the NSD2/mTORC2/ACLY Pathway. Front Immunol **2021**;12:751409
43. Jia D, Jolly MK, Tripathi SC, Den Hollander P, Huang B, Lu M*, et al.* Distinguishing mechanisms underlying EMT tristability. Cancer Converg **2017**;1:2
44. Legewie S, Schoeberl B, Bluthgen N, Herzel H. Competing docking interactions can bring about bistability in the MAPK cascade. Biophys J **2007**;93:2279-88
45. Fabian Z, Taylor CT, Nguyen LK. Understanding complexity in the HIF signaling pathway using systems biology and mathematical modeling. J Mol Med (Berl) **2016**;94:377-90
46. Henry KE, Mack KN, Nagle VL, Cornejo M, Michel AO, Fox IL*, et al.* ERK Inhibition Improves Anti-PD-L1 Immune Checkpoint Blockade in Preclinical Pancreatic Ductal Adenocarcinoma. Mol Cancer Ther **2021**;20:2026-34
47. Alagesan B, Contino G, Guimaraes AR, Corcoran RB, Deshpande V, Wojtkiewicz GR*, et al.* Combined MEK and PI3K inhibition in a mouse model of pancreatic cancer. Clin Cancer Res **2015**;21:396-404
48. Ozkan-Dagliyan I, Diehl JN, George SD, Schaefer A, Papke B, Klotz-Noack K*, et al.* Low-Dose Vertical Inhibition of the RAF-MEK-ERK Cascade Causes Apoptotic Death of KRAS Mutant Cancers. Cell Rep **2020**;31:107764
49. Bryant KL, Stalnecker CA, Zeitouni D, Klomp JE, Peng S, Tikunov AP*, et al.* Combination of ERK and autophagy inhibition as a treatment approach for pancreatic cancer. Nat Med **2019**;25:628-40
50. Lipner MB, Peng XL, Jin C, Xu Y, Gao Y, East MP*, et al.* Irreversible JNK1-JUN inhibition by JNK-IN-8 sensitizes pancreatic cancer to 5-FU/FOLFOX chemotherapy. JCI Insight **2020**;5
51. Lin YT, Wu KJ. Epigenetic regulation of epithelial-mesenchymal transition: focusing on hypoxia and TGF-beta signaling. J Biomed Sci **2020**;27:39
52. Wu MZ, Tsai YP, Yang MH, Huang CH, Chang SY, Chang CC*, et al.* Interplay between HDAC3 and WDR5 is essential for hypoxia-induced epithelial-mesenchymal transition. Mol Cell **2011**;43:811-22
53. Chen Y, Ren B, Yang J, Wang H, Yang G, Xu R*, et al.* The role of histone methylation in the development of digestive cancers: a potential direction for cancer management. Signal Transduct Target Ther **2020**;5:143
54. Dong B, Qiu Z, Wu Y. Tackle Epithelial-Mesenchymal Transition With Epigenetic Drugs in Cancer. Front Pharmacol **2020**;11:596239
55. Dovzhanskiy DI, Arnold SM, Hackert T, Oehme I, Witt O, Felix K*, et al.* Experimental in vivo and in vitro treatment with a new histone deacetylase inhibitor belinostat inhibits the growth of pancreatic cancer. BMC Cancer **2012**;12:226

56. Nguyen AH, Elliott IA, Wu N, Matsumura C, Vogelauer M, Attar N*, et al.* Histone deacetylase inhibitors provoke a tumor supportive phenotype in pancreatic cancer associated fibroblasts. Oncotarget **2017**;8:19074-88
57. Chao MW, Chang LH, Tu HJ, Chang CD, Lai MJ, Chen YY*, et al.* Combination treatment strategy for pancreatic cancer involving the novel HDAC inhibitor MPT0E028 with a MEK inhibitor beyond K-Ras status. Clin Epigenetics **2019**;11:85
58. Wang S, Yang H, Su M, Lian F, Cong Z, Wei R*, et al.* 5-Aminonaphthalene derivatives as selective nonnucleoside nuclear receptor binding SET domain-protein 2 (NSD2) inhibitors for the treatment of multiple myeloma. Eur J Med Chem **2021**;222:113592
59. Xu Y, Guo J, Liu J, Xie Y, Li X, Jiang H*, et al.* Hypoxia-induced CREB cooperates MMSET to modify chromatin and promote DKK1 expression in multiple myeloma. Oncogene **2021**;40:1231-41
60. Schodel J, Oikonomopoulos S, Ragoussis J, Pugh CW, Ratcliffe PJ, Mole DR. High-resolution genome-wide mapping of HIF-binding sites by ChIP-seq. Blood **2011**;117:e207-17
61. Wenger RH, Stiehl DP, Camenisch G. Integration of oxygen signaling at the consensus HRE. Sci STKE **2005**;2005:re12
62. Day EK, Campbell A, Pandolf A, Rogerson T, Zhong Q, Xiao A*, et al.* ERK-dependent suicide gene therapy for selective targeting of RTK/RAS-driven cancers. Mol Ther **2021**;29:1585-601
63. Song C, Ye M, Liu Z, Cheng H, Jiang X, Han G*, et al.* Systematic analysis of protein phosphorylation networks from phosphoproteomic data. Mol Cell Proteomics **2012**;11:1070-83
64. Vasseur S, Tomasini R, Tournaire R, Iovanna JL. Hypoxia induced tumor metabolic switch contributes to pancreatic cancer aggressiveness. Cancers (Basel) **2010**;2:2138-52
65. Jia D, Park JH, Kaur H, Jung KH, Yang S, Tripathi S*, et al.* Towards decoding the coupled decision-making of metabolism and epithelial-to-mesenchymal transition in cancer. Br J Cancer **2021**;124:1902-11
66. Guillaumond F, Leca J, Olivares O, Lavaut MN, Vidal N, Berthezene P*, et al.* Strengthened glycolysis under hypoxia supports tumor symbiosis and hexosamine biosynthesis in pancreatic adenocarcinoma. Proc Natl Acad Sci U S A **2013**;110:3919-24
67. Papa S, Choy PM, Bubici C. The ERK and JNK pathways in the regulation of metabolic reprogramming. Oncogene **2019**;38:2223-40
68. Teperino R, Schoonjans K, Auwerx J. Histone methyl transferases and demethylases; can they link metabolism and transcription? Cell Metab **2010**;12:321-7

FIGURE LEGENDS

Figure 1. EMT and hypoxia marker enrichment are correlated in human PDAC tumors and ductal cells. (A) CPTAC PDAC tumor samples were clustered using non-negative matrix factorization (NMF) of protein data for the pcEMT signature. Heatmap entries indicate z-scored expression. Left vertical side bar (green, purple) indicates assigned NMF cluster. The next three vertical side bars indicate Collisson, Moffit, and Bailey classifications (4). Horizontal side bar (red, blue) indicates phenotype associated with each protein (22). **(B)** Kaplan-Meier analysis for CPTAC PDAC patient survival, stratifying based on pcEMT with log-rank test. **(C)** Hallmark Hypoxia protein enrichment was calculated using GSVA and compared between M-high and -low tumors, with Mann-Whitney U test. **(D)** Partial rank correlation coefficients (PRCCs) of indicated variables were calculated with respect to mesenchymal pcEMT (pcEMT-M) enrichment. Hallmark Hypoxia enrichment from calculations in (C). Tissue content estimates were from CPTAC data. Error bars denote PRCC 95% confidence intervals. **(E)** Consensus clustering of human ductal cell scRNA-seq data (24) was performed on a 2D UMAP based on pcEMT-M features, resulting in groupings with shared epithelial features but differentially enriched for mesenchymal features (E+/M- and E+/M+). **(F)** Heatmap showing ductal cell pcEMT gene expression (normalized UMIs), annotated by clusters from (E). **(G)** mRNA enrichment of Hallmark Hypoxia signature (Pagoda2 scores) was computed and compared between E+/M+ and E+/M- ductal cells, Mann-Whitney U test.

Figure 2. Hypoxia drives a *bona fide* EMT in PDAC. (A) HPAF-II cells were cultured at 21%, 7%, or 1% O_2 for 120 hr, and immunofluorescence microscopy was performed as indicated, n = 3. One-way ANOVA with Tukey's multiple comparison test (vimentin). Mixed-effects analysis with Tukey's multiple comparison test (E-cadherin). Linear regression for E-cadherin and vimentin described in *Methods*. **(B)** GFP-expressing HPAF-II cells were cultured in 21% or 1% O_2 for 96 hr. Fluorescence microscopy was performed, and cluster shape factors were calculated. Data represented as mean ± s.e.m. $p < 0.0001$ for slopes comparison, see *Methods*. **(C)** HPAF-II cells were cultured for 120 hr in 21% or 1% O_2, and qRT-PCR was performed for indicated markers, with *CASC3* used for normalization. n = 3, with t test per transcript. **(D)** H&E and immunohistochemistry for Hypoxyprobe (HYP) and CD31 was performed for murine normal pancreas and PDX tumors. Representative image shown, n = 3. **(E)** Sections of normal mouse pancreas or PDX 395 tumors were stained as indicated. Image analysis was performed for PDX 395 tumors and quantified for the percent CD31+ cells that were HYP+/-. n = 3, t test. **(F)** PDX 395 tumor sections were stained to quantify COXIV+/vimentin+ cells that were HYP+/-. n = 4, t test. Dotted line separates HYP+/- regions. **(G)** KPCY tumor sections were stained as indicated, and image analysis was performed to quantify YFP+/vimentin+ cells that were HYP+/-. Data represented as fold-change due to variability across mice for the spontaneous model. n = 4, t test. **(H)** Subcutaneous PD7591 cell tumors were stained as indicated, with quantification of YFP+/vimentin+ cells that were HYP+/-. n = 6, t test. **(I)** PD7591 cell subcutaneous tumor sections were stained as indicated, with quantification for YFP+/HYP+ cells that were $Ecad^{high/low}$. Arrow denotes an HYP+/$Ecad^{low}$ cell. n = 4, with t test. * $p < 0.05$, ** $p < 0.01$, *** $p < 0.001$, **** $p < 0.0001$

Figure 3. Hypoxia-driven EMT occurs heterogeneously and is more durable than growth factor-driven EMT. (A) HPAF-II cells were cultured in 21% O_2 ± 10 ng/mL TGFβ and 50 ng/mL HGF or cultured in 1% O_2 for 120 hr. Vimentin flow cytometry was performed. Representative histograms for single replicates are shown, with data for n = 3 in the bar plot. One-way ANOVA with Tukey's pairwise comparisons against the 21% O_2 control. **(B)** PDAC cells from three backgrounds were cultured as in (A). Immunofluorescence microscopy was performed as indicated. n = 3, two-way ANOVA with Tukey's multiple comparisons test. **(C)** HPAF-II cells

were cultured as in (A), re-plated on coverslips, and cultured in 21% O_2 without growth factors for ≤ 120 hr. At indicated times, immunofluorescence microscopy was performed as indicated. *n* = 3, data represented as mean ± s.e.m. $p < 0.0001$ for nonlinear regression comparing slopes. **(D)** 120 hr after treatment withdrawal from 10 ng/mL TGFβ + 50 ng/mL HGF or 1% O_2 culture. HPAF-II cells were stained to quantify dividing, vimentin+ cells (examples encircled). *n* = 3, with t test. **(E)** Orthotopic HPAF-II hypoxia fate-mapping tumor sections were stained as indicated. Image analysis quantified fraction of GFP+ (once-hypoxic) cells that were vimentin+ and Hypoxyprobe-negative (HYP-) or positive (HYP+). *n* = 6, with t test. **(F)** Explanted tumors described in (E) were disaggregated and flow-sorted based on DsRed and GFP. Indicated populations were cultured in 21% O_2 for 12 days, then stained with indicated antibodies. *n* = 4, with t test. * $p < 0.05$, ** $p < 0.01$, **** $p < 0.0001$

Figure 4. Hypoxia promotes EMT through MAPK signaling initiated by suppressed phosphatase expression. (A) Overrepresentation analysis for indicated KEGG pathways based on kinases described in the text. Analysis based on CPTAC PDAC Discovery Study data (4). Kinase count and ratio indicate the number and fraction in each gene set with significant, positive correlations with Hallmark Hypoxia enrichment. **(B)** Coefficients are shown for regularized linear regression of Hallmark Hypoxia Pagoda2 score based on KEGG signaling pathway Pagoda2 scores for scRNA-seq data (24). Error bars denote 95% confidence intervals. **(C)** HPAF-II cells were cultured for 120 hr in 21% or 1% O_2 with 1 μM CI-1040 (MEKi), 10 μM SP600125 (JNKi), 10 μM SB203580 (p38i), or DMSO. *n* = 3, two-way ANOVA with Sidak's multiple comparisons test. **(D)** PDX 395 cells were cultured in 1% O_2 with 1 μM CI-1040 (MEKi), 10 μM SP600125 (JNKi), a combination, or DMSO for 120 hr. Cells were stained as indicated, and immunofluorescence microscopy and image analysis were performed. *n* = 3, one-way ANOVA with Dunnett's multiple comparison test. **(E)** HPAF-II cells were cultured in 21% O_2 ± 10 ng/mL TGFβ + 50 ng/mL HGF, or in 1% O_2, and lysed 24 and 120 hr after treatment. Immunoblotting was performed as indicated. *n* = 3, one-way ANOVA with Tukey's multiple comparisons test. **(F)** HPAF-II cells were cultured for 120 hr in 21 or 1% O_2 with 10 μM PP2 (Src family kinase inhibitor, SFKi) or DMSO, and immunofluorescence microscopy was performed for nuclear c-Jun. *n* = 3, mixed-effects analysis with Tukey's multiple comparisons test. **(G)** HPAF-II cells were treated as in (F), and lysates were analyzed by immunoblotting as indicated. *n* = 3**,** two-way ANOVA with Sidak's multiple comparison test. **(H)** HPAF-II cells were cultured in 21% O_2 ± 10 ng/mL TGFβ and 50 ng/mL HGF or in 1% O_2 for 120 hr. Cells were pre-treated with 10 μM PP2 or DMSO 24 hr prior to hypoxia or growth factor treatment. *n* = 3, two-way ANOVA with Sidak's multiple comparison test. **(I)** qRT-PCR was performed for PP1A, PP2A, and PP2C subunit transcripts for HPAF-II cells treated as in (D) for 120 hr, with *CASC3* used for normalization. *n* = 3, one-way ANOVA with Tukey's multiple comparisons test. **(J)** HPAF-II cells were cultured for 120 hr in 21% O_2 with 5 μM LB100 (PP2Ai), 1.5 μM sanguinarine chloride (PP2Cδi), or DMSO. *n* = 3, one-way ANOVA with Tukey's multiple comparisons test. * $p < 0.05$, ** $p < 0.01$, *** $p < 0.001$, **** $p < 0.0001$

Figure 5. Hypoxic PDAC tissue is enriched for MAPK markers, and MAPK inhibition prevents hypoxic cell EMT. (A) KPCY tumor sections were stained as indicated, and YFP+/c-Jun+ cells that were Hypoxyprobe (HYP) +/- were quantified and reported as fold-changes from HYP- to HYP+. *n* = 3, with t test. Dotted line separates HYP+/- regions. **(B)** 7160c2 subcutaneous tumor sections were stained as indicated, and image analysis was performed as in (A). *n* = 4, with t test. **(C)** PDX 395 orthotopic tumor sections were stained as indicated, and c-Jun+ cells that were HYP+/- or vimentin+/- were quantified. c-Jun+ data reported as fold-change in percent c-Jun+ cells that were HYP+/-. *n* = 3, with t test. **(D)** PDX 395 tumor sections were stained as indicated, and the percent of vimentin+/- cells that were pERK+ was quantified. *n* = 3, with t test. **(E)** HPAF-II cells were cultured in 21% O_2 ± 10 ng/mL TGFβ + 50 ng/mL HGF

or in 1% O_2 for 120 hr. Cells were re-plated for 120 hr at 21% O_2 without exogenous growth factors and with 1 μM CI-1040 (MEKi) and 10 μM SP600125 (JNKi) or DMSO. At times indicated, cells were stained for vimentin. Immunofluorescence microscopy was performed to quantify percentage of vimentin+ cells. *n* = 3, two-way ANOVA with Tukey's multiple comparisons test. **(F)** Mice bearing orthotopic PDX 395 tumors were treated for nine days with selumetinib (MEKi), SP600125 (JNKi), selumetinib+SP600125, or vehicle. Tumor sections were stained for COXIV, HYP, and vimentin, and image analysis was performed. *n* = 5 - 6, two-way ANOVA with Tukey's multiple comparisons test. * $p < 0.05$, ** $p < 0.01$, *** $p < 0.001$, **** $p < 0.0001$

Figure 6. HIFs play a supporting role in hypoxia-mediated EMT. (A,B) HPAF-II cells were transfected with HIF-1α or HIF-2α siRNA, both siRNAs, or control siRNA. 24 hr later, cells were switched to 1% O_2 or maintained in 21% O_2 for 120 hr. **(A)** Immunofluorescence microscopy was performed, with quantification for vimentin+ cells. *n* = 3, two-way ANOVA with Tukey's multiple comparisons test. **(B)** qRT-PCR was performed for indicated transcripts, with *CASC3* used for normalization. *n* = 3, two-way ANOVA with Tukey's multiple comparisons test. **(C)** Immunofluorescence microscopy was performed on HPAF-II cells stably expressing HIF-1α and HIF-2α or control shRNAs. Cells were cultured in 21% or 1% O_2 for 120 hr prior to fixing and staining as indicated. *n* = 3, two-way ANOVA with Tukey's multiple comparisons test. **(D)** HPAF-II cells were pre-treated with 1 μM CI-1040 (MEKi), 10 μM SP600125 (JNKi), a combination, or DMSO for 24 hr, then cultured in 21 or 1% O_2 for 4 hr. *n* = 3, two-way ANOVA with Tukey's multiple comparisons test. **(E)** *HIF1A* qRT-PCR was performed for HPAF-II cells cultured for 120 hr in 21% or 1% O_2 with 1 μM CI-1040 (MEKi),10 μM SP600125 (JNKi), a combination, or DMSO. *CASC3* used as normalization control. *n* = 3, two-way ANOVA with Tukey's multiple comparisons test, comparisons against controls. * $p < 0.05$, ** $p < 0.01$, *** $p < 0.001$, **** $p < 0.0001$

Figure 7. Hypoxia reduces KDM2A activity and stabilizes NSD2 to promote histone methylation-dependent EMT. (A) HPAF-II cells were cultured in 21% O_2 ± 10 ng/mL TGFβ + 50 ng/mL HGF or in 1% O_2 for 120 hr, and H3K36 dimethylation (H3K36me2) was measured by immunofluorescence microscopy. *n* = 3, mixed-effects analysis with Tukey's multiple comparisons test. **(B-C)** Michaelis-Menten saturation curves were created with Lineweaver-Burk plots for KDM2A binding kinetics for **(B)** H3K36me2 and **(C)** oxygen, with velocity (*V*) reported as disintegration parts per minute (dpm). Data shown for a representative run, with solid lines corresponding to model fits. **(D)** KPCY-derived cell lines 3077c4, 6419c5, and 6694c2 were cultured in 21% or 1% O_2 for 120 hr. Cells were then fixed and stained as indicated, and immunofluorescence microscopy was performed. *n* = 3, mixed-effects analysis for H3K36me2 per cell line. **(E)** Immunofluorescence microscopy was performed for NSD2 expression in HPAF-II cells treated as in (A). *n* = 3, mixed-effects analysis with Tukey's multiple comparisons test. **(F)** HPAF-II cells were cultured for 120 hr in 21% O_2 with 5 μM LB100 (PP2Ai), 1.5 μM sanguinarine chloride (PP2Cδi), or DMSO. Immunofluorescence microscopy was performed for NSD2. *n* = 3, mixed-effects analysis with Tukey's multiple comparisons. **(G)** HPAF-II cells were transfected with control or NSD2 siRNA. 24 hr later, cells were treated as in (A) for 120 hr. Immunofluorescence microscopy was performed as indicated. *n* = 3, two-way ANOVA for vimentin positivity with Sidak's multiple comparisons test and mixed-effects analysis for H3K36me2 with Tukey's multiple comparisons test. **(H)** HPAF-II cells were cultured in 1% O_2 with 1 μM CI-1040 (MEKi), 10 μM SP600125 (JNKi), and 1.5 μM sanguinarine chloride (PP2Cδi), or DMSO for 120 hr. *n* = 3, mixed-effects analysis with Tukey's multiple comparisons test. * $p < 0.05$, ** $p < 0.01$, *** $p < 0.001$

Figure 8. Hypoxia promotes EMT through an integrated histone methylation and MAPK mechanism. Hypoxia suppresses KDM2A activity resulting in dimethylation of H3K36, which in turn suppresses expression of protein phosphatase subunits. Decreased protein phosphatase expression promotes SFK and MAPK signaling to stabilize NSD2, HIF-1α, and nuclear c-Jun expression. Elevated NSD2 expression further promotes H3K36 dimethylation, reinforcing the integrated kinase signaling/histone methylation regulatory loop. Collectively, this promotes expression of EMT-regulating genes.

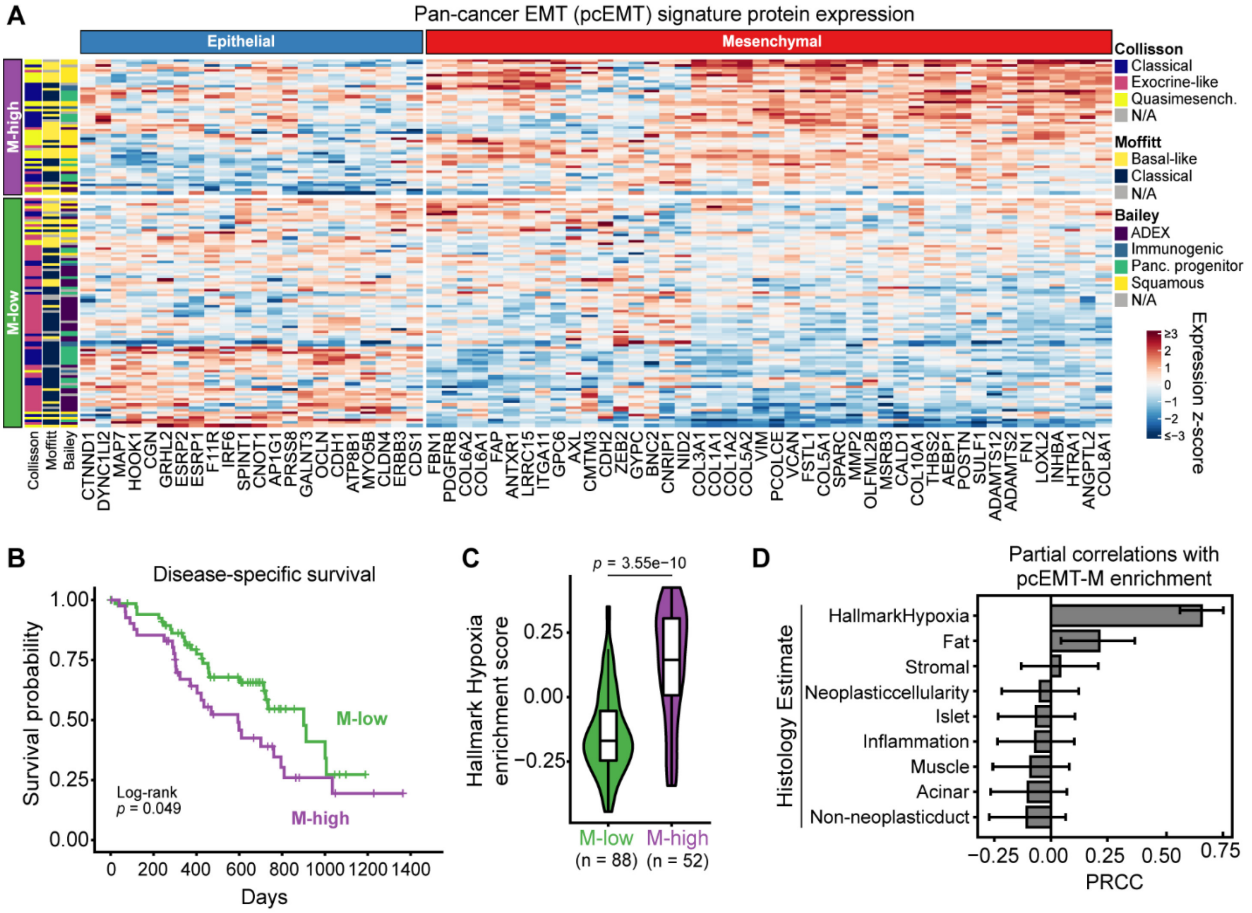
A
Pan-cancer EMT (pcEMT) signature protein expression
Epithelial
Mesenchymal
M-high
M-low
Collisson
Classical
Exocrine-like
Quasimesench.
N/A
Moffitt
Basal-like
Classical
N/A
Bailey
ADEX
Immunogenic
Panc. progenitor
Squamous
N/A
Expression z-score
B
Disease-specific survival
Survival probability
Log-rank p = 0.049
M-low
M-high
Days
C
p = 3.55e−10
Hallmark Hypoxia enrichment score
M-low (n = 88)
M-high (n = 52)
D
Partial correlations with pcEMT-M enrichment
Histology Estimate
HallmarkHypoxia
Fat
Stromal
Neoplasticcellularity
Islet
Inflammation
Muscle
Acinar
Non-neoplasticduct
PRCC

Single-Cell RNA-Sequencing: Human Ductal Cells
E
pcEMT−M signature
Consensus cluster
E+/M−
E+/M+
UMAP2
UMAP1
F
pcEMT signature mRNA expression
Epithelial
Mesenchymal
E+/M+
E+/M-
Normalized UMIs
G
p = 9.19e−32
Hallmark Hypoxia Pagoda2 score
E+/M- (n = 342)
E+/M+ (n = 861)

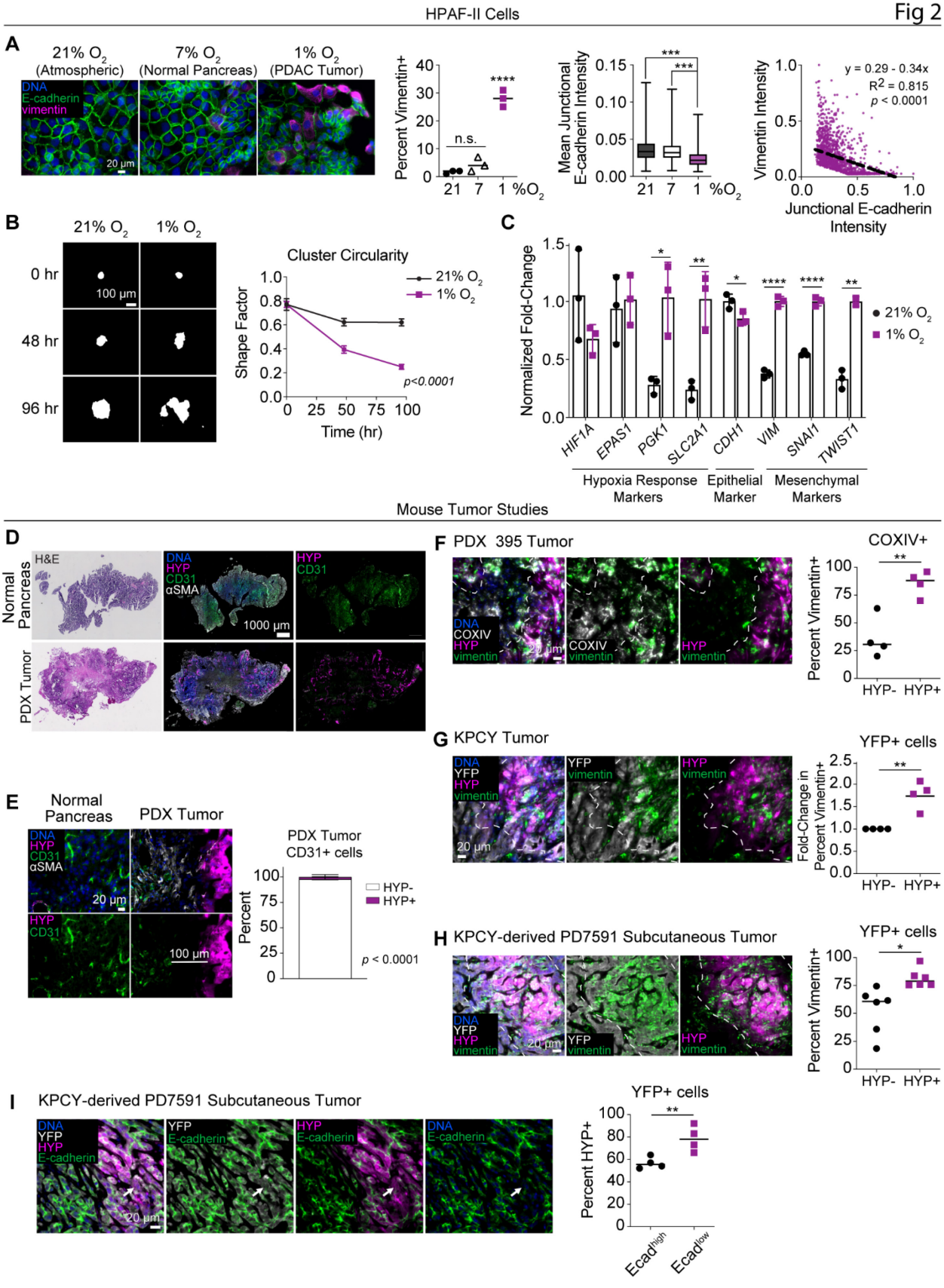
HPAF-II Cells
A
21% O2 (Atmospheric)
7% O2 (Normal Pancreas)
1% O2 (PDAC Tumor)
DNA
E-cadherin
vimentin
20 μm
Percent Vimentin+
n.s.
****
21 7 1 %O2
Mean Junctional E-cadherin Intensity
***
***
Vimentin Intensity
y = 0.29 - 0.34x
R2 = 0.815
p < 0.0001
Junctional E-cadherin Intensity
B
21% O2
1% O2
0 hr
48 hr
96 hr
100 μm
Cluster Circularity
Shape Factor
p<0.0001
Time (hr)
C
Normalized Fold-Change
HIF1A
EPAS1
PGK1
SLC2A1
CDH1
VIM
SNAI1
TWIST1
Hypoxia Response Markers
Epithelial Marker
Mesenchymal Markers
Mouse Tumor Studies
D
Normal Pancreas
PDX Tumor
H&E
DNA
HYP
CD31
αSMA
1000 μm
E
Normal Pancreas
PDX Tumor
20 μm
100 μm
PDX Tumor CD31+ cells
Percent
HYP-
HYP+
p < 0.0001
F
PDX 395 Tumor
COXIV
HYP
vimentin
20 μm
COXIV+
Percent Vimentin+
HYP-
HYP+
G
KPCY Tumor
YFP
YFP+ cells
Fold-Change in Percent Vimentin+
H
KPCY-derived PD7591 Subcutaneous Tumor
I
KPCY-derived PD7591 Subcutaneous Tumor
E-cadherin
Percent HYP+
Ecadhigh
Ecadlow

Fig 3

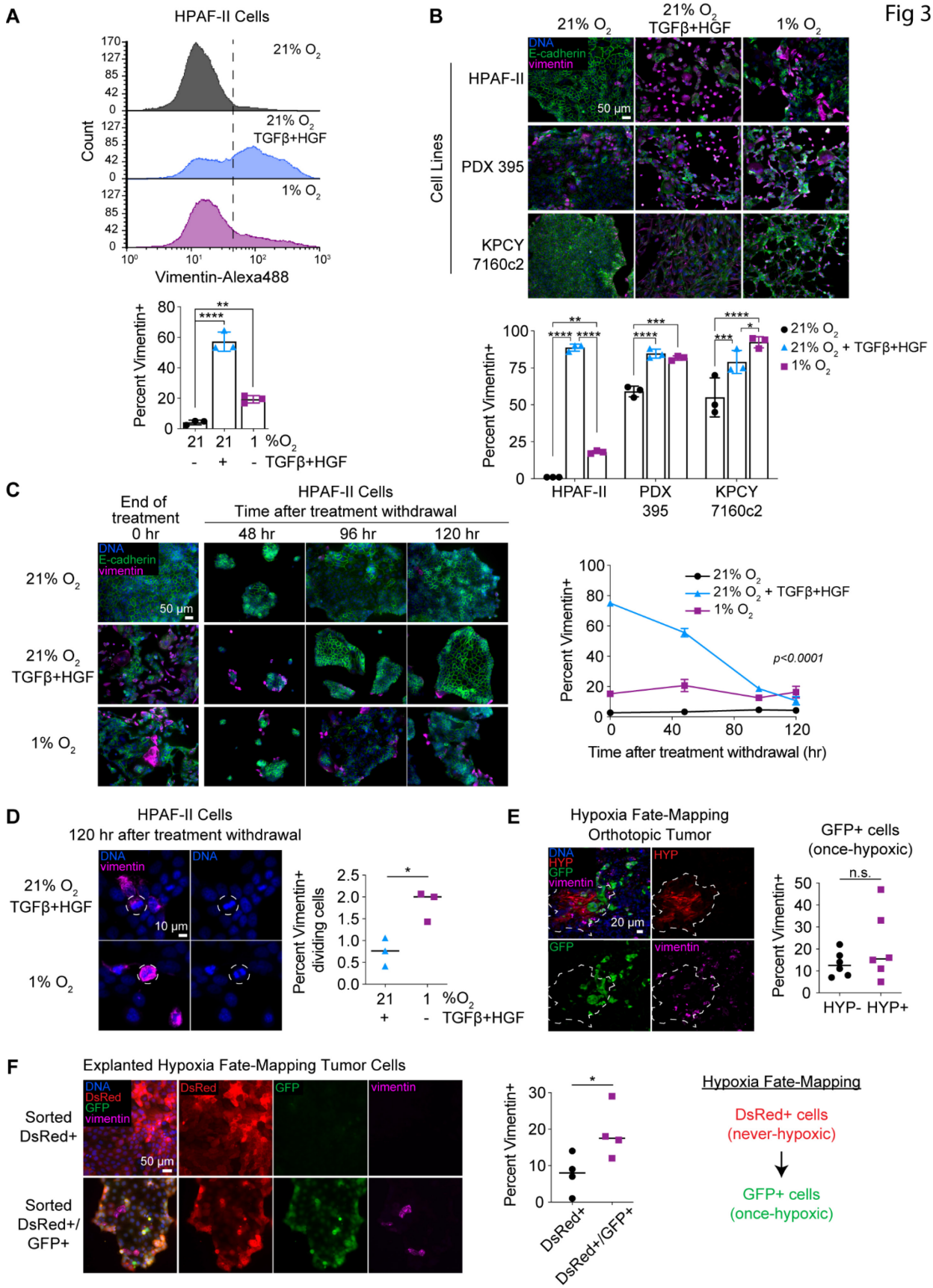
A
HPAF-II Cells
21% O2
21% O2 TGFβ+HGF
1% O2
Count
Vimentin-Alexa488
Percent Vimentin+
21 21 1 %O2
- + - TGFβ+HGF
B
21% O2
21% O2 TGFβ+HGF
1% O2
Cell Lines
HPAF-II
PDX 395
KPCY 7160c2
DNA
E-cadherin
vimentin
50 μm
Percent Vimentin+
21% O2
21% O2 + TGFβ+HGF
1% O2
HPAF-II
PDX 395
KPCY 7160c2
C
End of treatment 0 hr
HPAF-II Cells
Time after treatment withdrawal
48 hr
96 hr
120 hr
21% O2
21% O2 TGFβ+HGF
1% O2
Percent Vimentin+
p<0.0001
Time after treatment withdrawal (hr)
D
HPAF-II Cells
120 hr after treatment withdrawal
DNA
vimentin
10 μm
Percent Vimentin+ dividing cells
21 1 %O2
+ - TGFβ+HGF
E
Hypoxia Fate-Mapping
Orthotopic Tumor
DNA
HYP
GFP
vimentin
20 μm
GFP+ cells
(once-hypoxic)
n.s.
Percent Vimentin+
HYP- HYP+
F
Explanted Hypoxia Fate-Mapping Tumor Cells
Sorted DsRed+
Sorted DsRed+/ GFP+
DNA
DsRed
GFP
vimentin
50 μm
Percent Vimentin+
DsRed+
DsRed+/GFP+
Hypoxia Fate-Mapping
DsRed+ cells
(never-hypoxic)
GFP+ cells
(once-hypoxic)

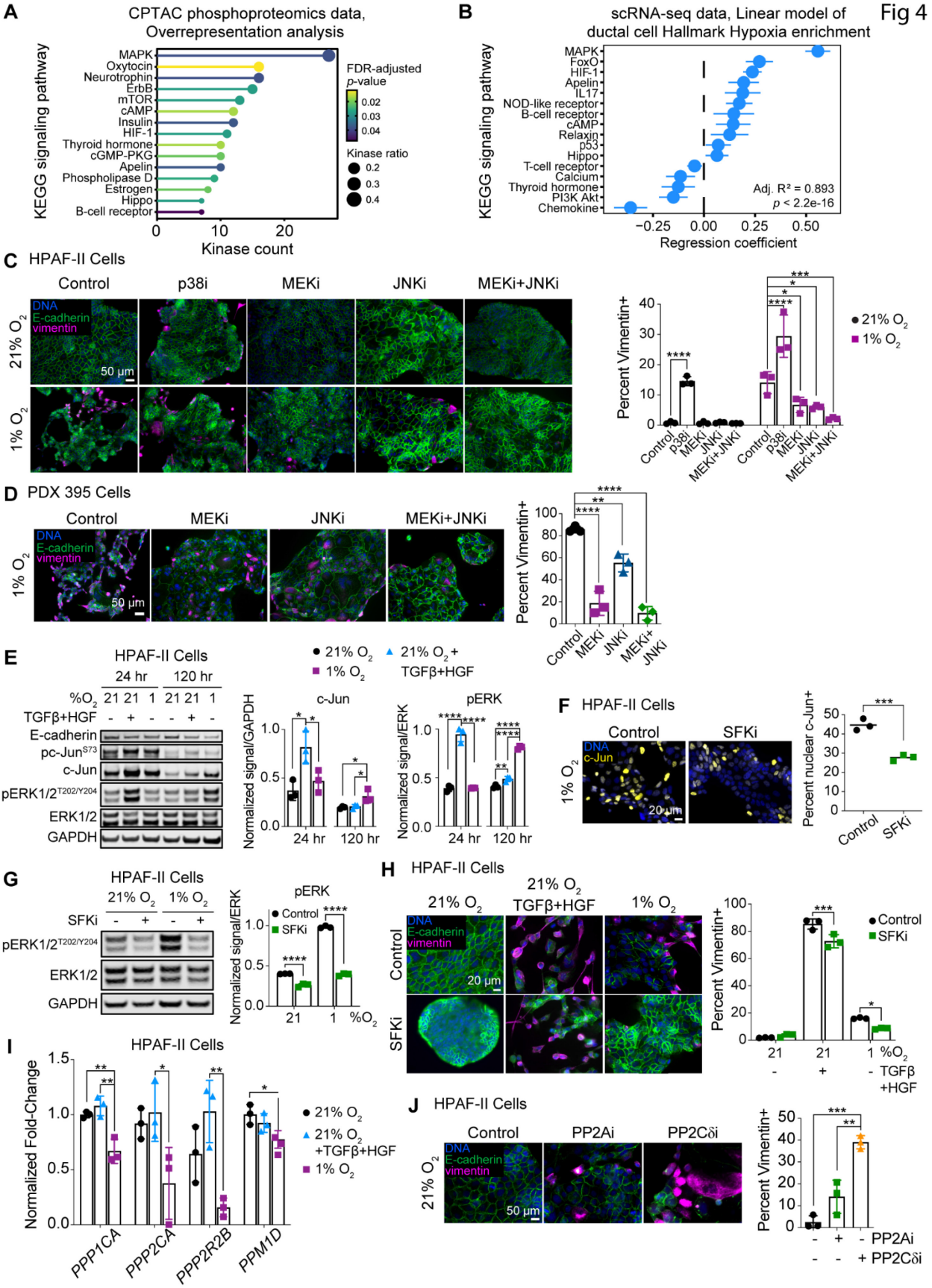
A
CPTAC phosphoproteomics data, Overrepresentation analysis
KEGG signaling pathway
MAPK
Oxytocin
Neurotrophin
ErbB
mTOR
cAMP
Insulin
HIF-1
Thyroid hormone
cGMP-PKG
Apelin
Phospholipase D
Estrogen
Hippo
B-cell receptor
FDR-adjusted p-value
0.02
0.03
0.04
Kinase ratio
0.2
0.3
0.4
0
10
20
Kinase count
B
scRNA-seq data, Linear model of ductal cell Hallmark Hypoxia enrichment
KEGG signaling pathway
MAPK
FoxO
HIF-1
Apelin
IL17
NOD-like receptor
B-cell receptor
cAMP
Relaxin
p53
Hippo
T-cell receptor
Calcium
Thyroid hormone
PI3K Akt
Chemokine
Adj. R² = 0.893
p < 2.2e-16
−0.25
0.00
0.25
0.50
Regression coefficient
C
HPAF-II Cells
Control
p38i
MEKi
JNKi
MEKi+JNKi
21% O2
1% O2
DNA
E-cadherin
vimentin
50 μm
Percent Vimentin+
21% O2
1% O2
D
PDX 395 Cells
Control
MEKi
JNKi
MEKi+JNKi
1% O2
DNA
E-cadherin
vimentin
50 μm
Percent Vimentin+
E
HPAF-II Cells
24 hr
120 hr
%O2 21 21 1 21 21 1
TGFβ+HGF - + - - + -
E-cadherin
pc-Jun S73
c-Jun
pERK1/2 T202/Y204
ERK1/2
GAPDH
21% O2
1% O2
21% O2 + TGFβ+HGF
c-Jun
pERK
Normalized signal/GAPDH
Normalized signal/ERK
24 hr
120 hr
F
HPAF-II Cells
Control
SFKi
1% O2
DNA
c-Jun
20 μm
Percent nuclear c-Jun+
G
HPAF-II Cells
21% O2
1% O2
SFKi - + - +
pERK1/2 T202/Y204
ERK1/2
GAPDH
pERK
Control
SFKi
Normalized signal/ERK
21
1
%O2
H
HPAF-II Cells
21% O2
21% O2 TGFβ+HGF
1% O2
Control
SFKi
DNA
E-cadherin
vimentin
20 μm
Percent Vimentin+
Control
SFKi
21 21 1 %O2
- + - TGFβ +HGF
I
HPAF-II Cells
Normalized Fold-Change
PPP1CA
PPP2CA
PPP2R2B
PPM1D
21% O2
21% O2 +TGFβ+HGF
1% O2
J
HPAF-II Cells
Control
PP2Ai
PP2Cδi
21% O2
DNA
E-cadherin
vimentin
50 μm
Percent Vimentin+
- + - PP2Ai
- - + PP2Cδi

Fig 5

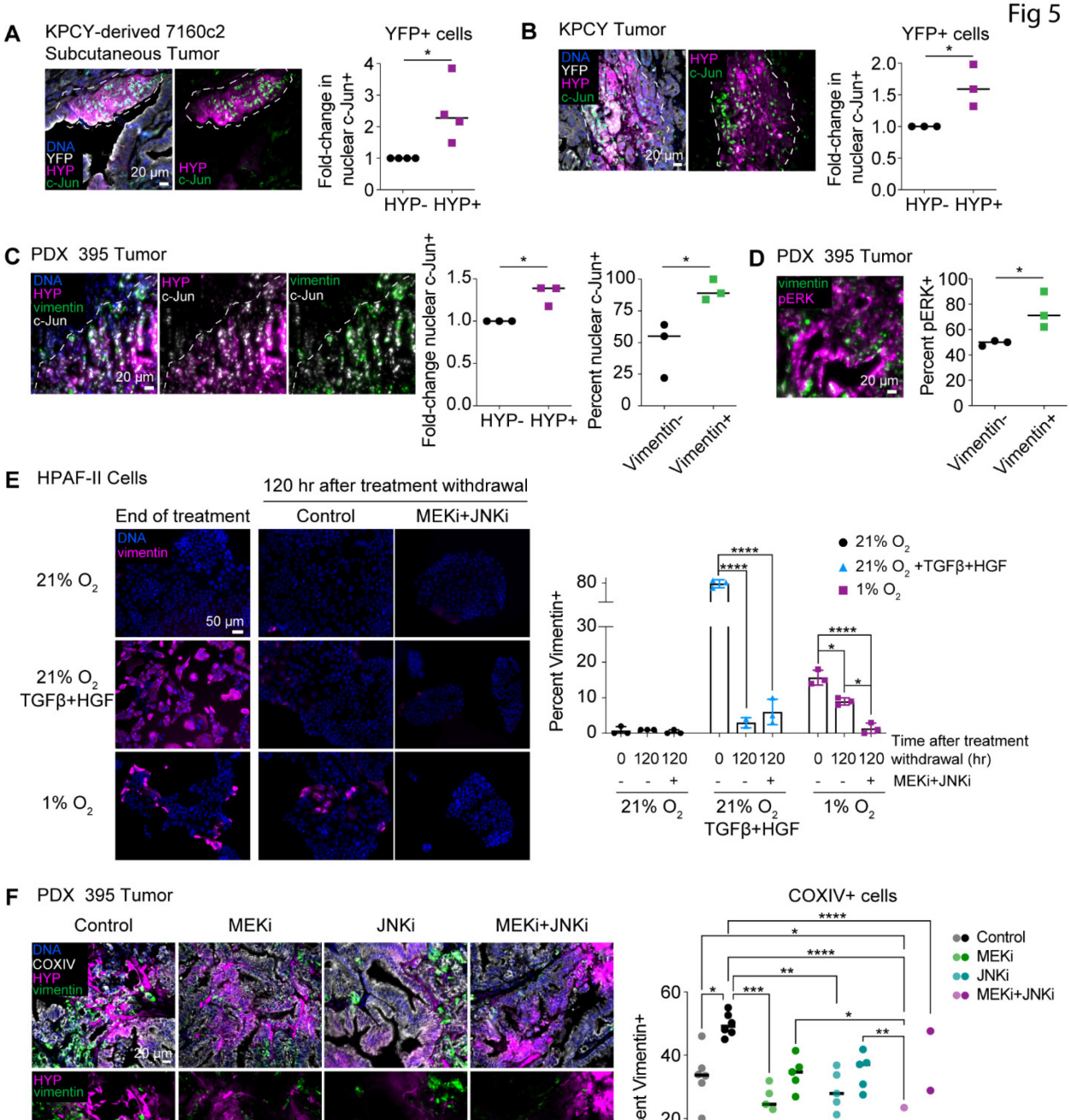
A
KPCY-derived 7160c2
Subcutaneous Tumor
DNA
YFP
HYP
c-Jun
20 μm
HYP
c-Jun
YFP+ cells
Fold-change in nuclear c-Jun+
HYP- HYP+
B
KPCY Tumor
DNA
YFP
HYP
c-Jun
20 μm
HYP
c-Jun
YFP+ cells
Fold-change in nuclear c-Jun+
HYP- HYP+
C
PDX 395 Tumor
DNA
HYP
vimentin
c-Jun
20 μm
HYP
c-Jun
vimentin
c-Jun
Fold-change nuclear c-Jun+
HYP- HYP+
Percent nuclear c-Jun+
Vimentin-
Vimentin+
D
PDX 395 Tumor
vimentin
pERK
20 μm
Percent pERK+
Vimentin-
Vimentin+
E
HPAF-II Cells
120 hr after treatment withdrawal
End of treatment
Control
MEKi+JNKi
DNA
vimentin
50 μm
21% O2
21% O2 TGFβ+HGF
1% O2
21% O2
21% O2 +TGFβ+HGF
1% O2
Percent Vimentin+
Time after treatment withdrawal (hr)
MEKi+JNKi
21% O2
21% O2 TGFβ+HGF
1% O2
F
PDX 395 Tumor
Control
MEKi
JNKi
MEKi+JNKi
DNA
COXIV
HYP
vimentin
20 μm
HYP
vimentin
COXIV+ cells
Control
MEKi
JNKi
MEKi+JNKi
Percent Vimentin+
HYP

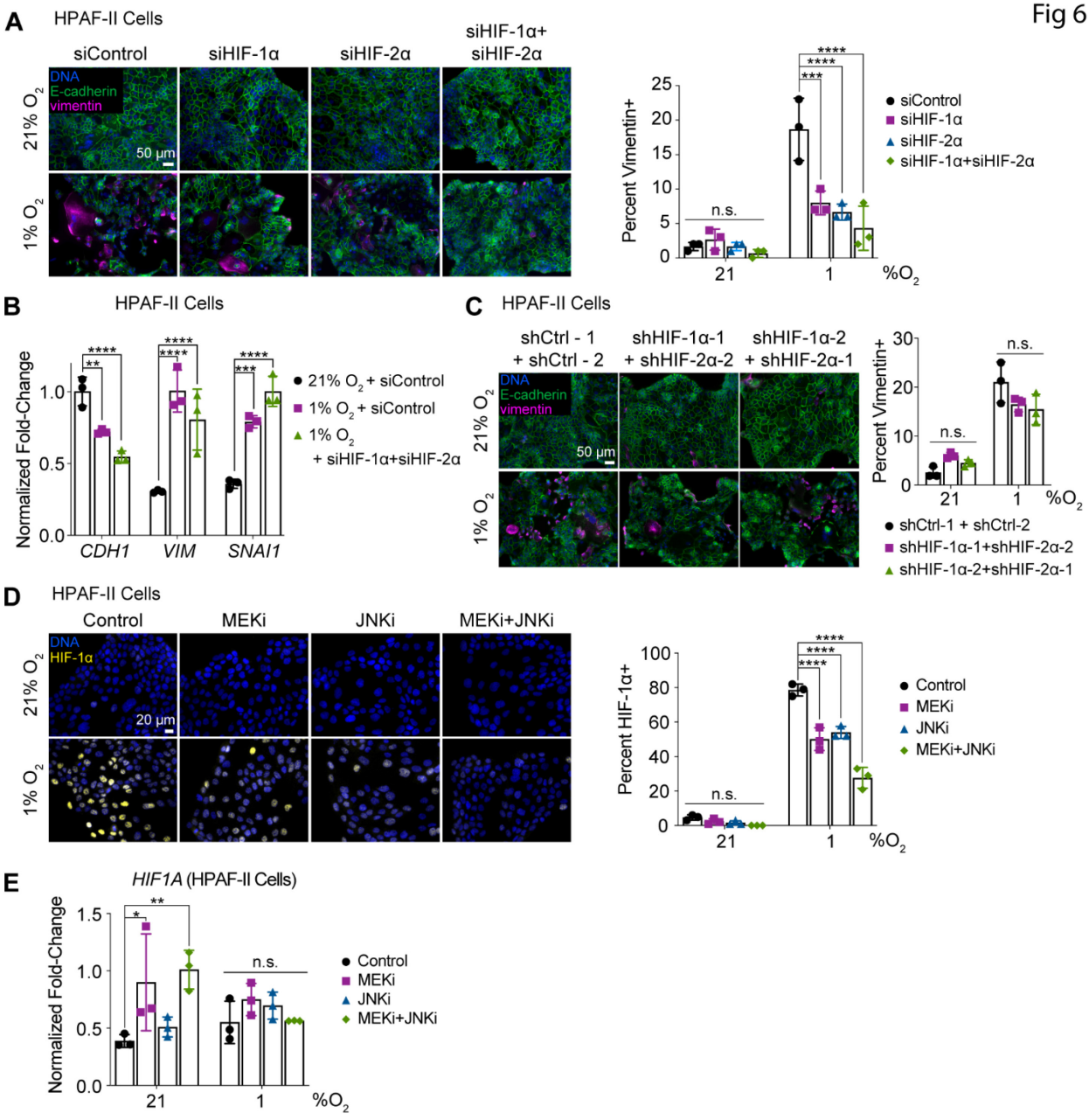
A
HPAF-II Cells
siControl
siHIF-1α
siHIF-2α
siHIF-1α+ siHIF-2α
21% O2
1% O2
DNA
E-cadherin
vimentin
50 μm
Percent Vimentin+
n.s.
%O2
siControl
siHIF-1α
siHIF-2α
siHIF-1α+siHIF-2α
B
HPAF-II Cells
Normalized Fold-Change
CDH1
VIM
SNAI1
21% O2 + siControl
1% O2 + siControl
1% O2 + siHIF-1α+siHIF-2α
C
HPAF-II Cells
shCtrl - 1 + shCtrl - 2
shHIF-1α-1 + shHIF-2α-2
shHIF-1α-2 + shHIF-2α-1
Percent Vimentin+
shCtrl-1 + shCtrl-2
shHIF-1α-1+shHIF-2α-2
shHIF-1α-2+shHIF-2α-1
D
HPAF-II Cells
Control
MEKi
JNKi
MEKi+JNKi
HIF-1α
20 μm
Percent HIF-1α+
E
HIF1A (HPAF-II Cells)
Normalized Fold-Change

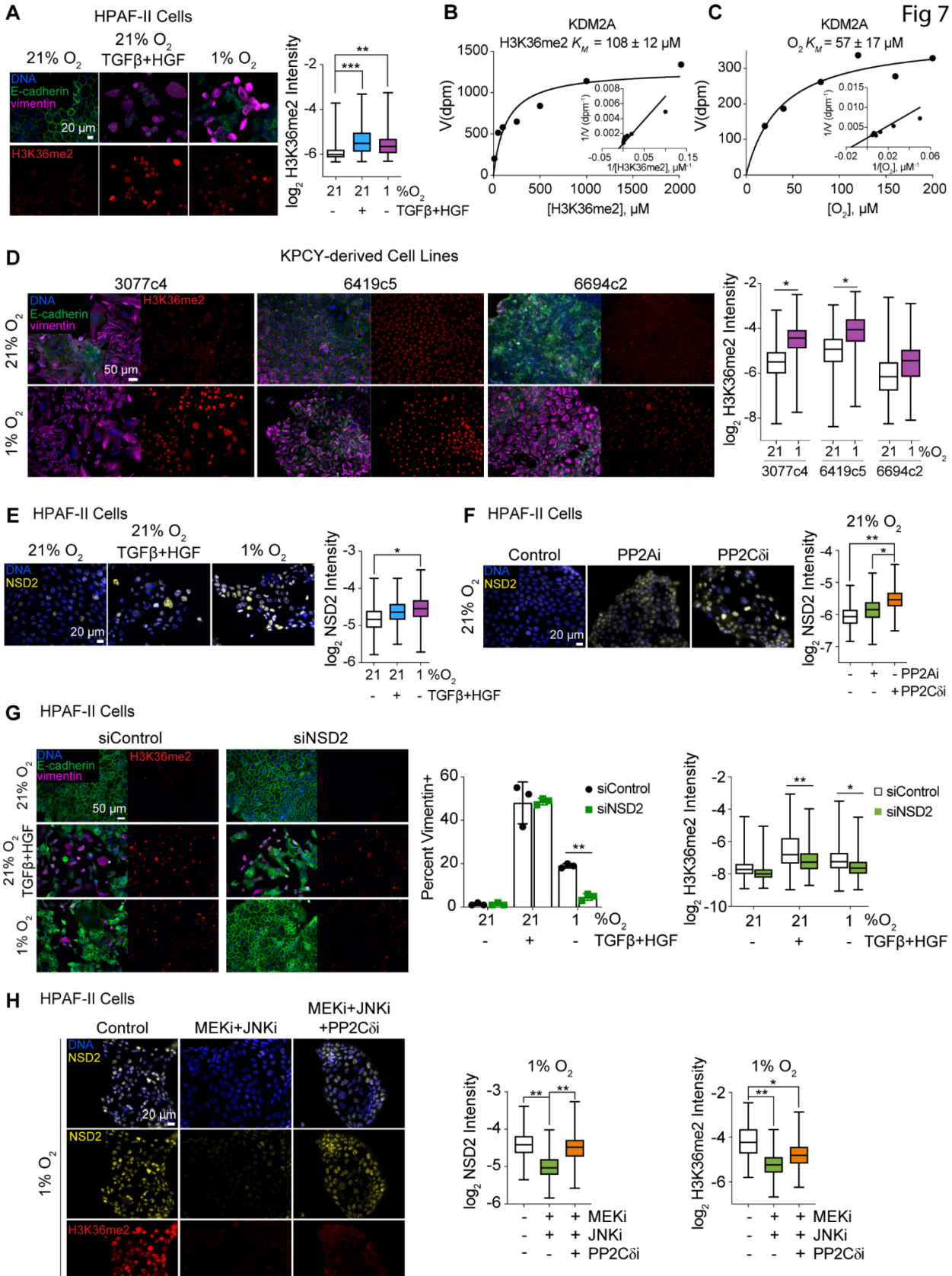
A
HPAF-II Cells
21% O2
21% O2 TGFβ+HGF
1% O2
DNA
E-cadherin
vimentin
20 μm
H3K36me2
log2 H3K36me2 Intensity
21 21 1 %O2
- + - TGFβ+HGF
B
KDM2A
H3K36me2 KM = 108 ± 12 μM
V(dpm)
[H3K36me2], μM
1/V (dpm-1)
1/[H3K36me2], μM-1
C
KDM2A
O2 KM = 57 ± 17 μM
V(dpm)
[O2], μM
1/[O2], μM-1
D
KPCY-derived Cell Lines
3077c4
6419c5
6694c2
21% O2
1% O2
50 μm
log2 H3K36me2 Intensity
21 1 21 1 21 1 %O2
3077c4 6419c5 6694c2
E
HPAF-II Cells
NSD2
log2 NSD2 Intensity
- + - TGFβ+HGF
F
HPAF-II Cells
Control
PP2Ai
PP2Cδi
- + - PP2Ai
- - + PP2Cδi
G
HPAF-II Cells
siControl
siNSD2
21% O2 TGFβ+HGF
Percent Vimentin+
siControl
siNSD2
H
HPAF-II Cells
Control
MEKi+JNKi
MEKi+JNKi +PP2Cδi
1% O2
- + + MEKi
- + + JNKi
- - + PP2Cδi

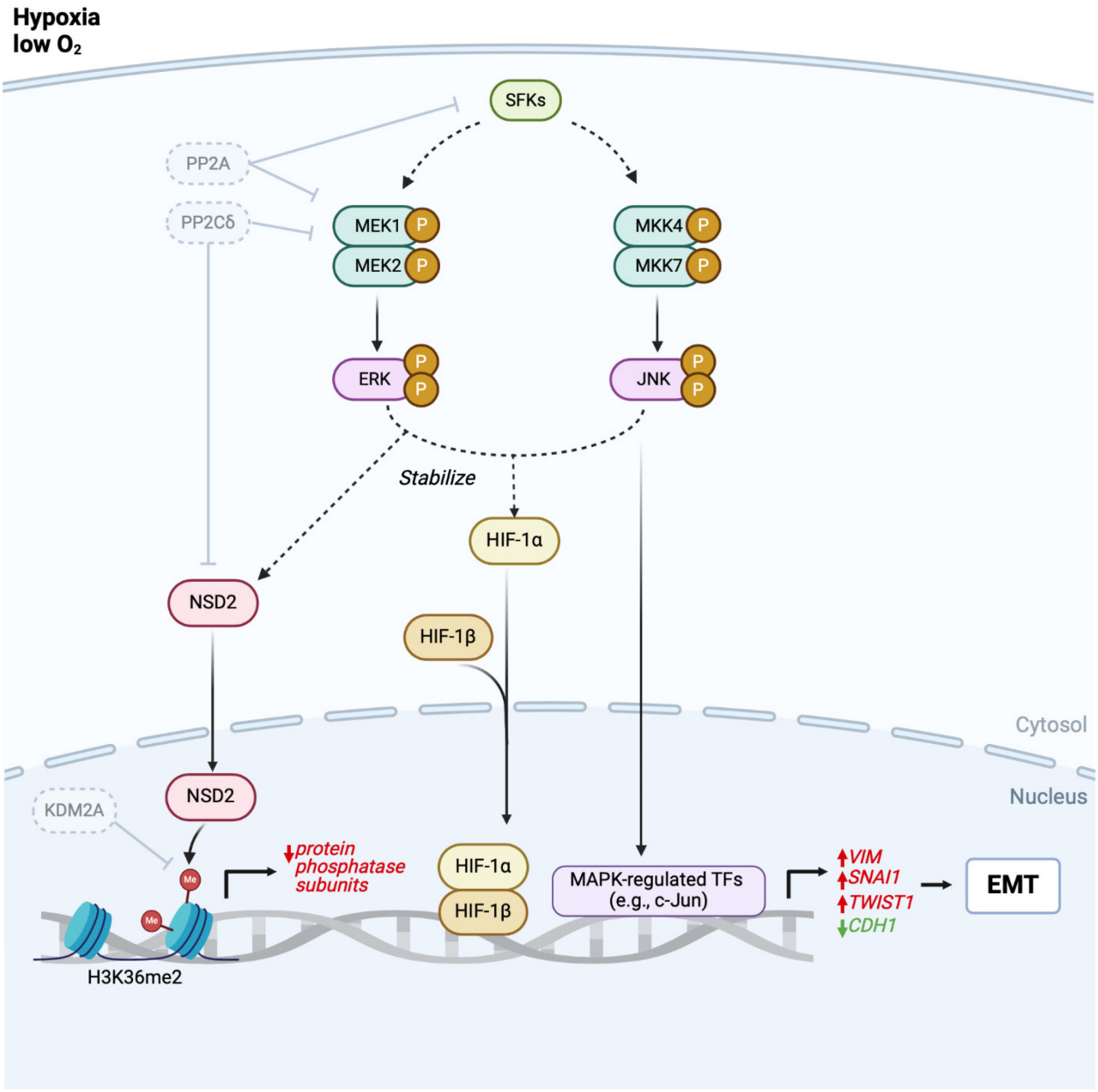
Hypoxia
low O_2
SFKs
PP2A
PP2Cδ
MEK1
MEK2
MKK4
MKK7
ERK
JNK
Stabilize
HIF-1α
NSD2
HIF-1β
Cytosol
Nucleus
NSD2
KDM2A
protein phosphatase subunits
HIF-1α
HIF-1β
MAPK-regulated TFs (e.g., c-Jun)
VIM
SNAI1
TWIST1
CDH1
EMT
H3K36me2

SUPPLEMENTARY DATA

A histone methylation-MAPK signaling axis drives durable epithelial-mesenchymal transition in hypoxic pancreas cancer.

Brooke A. Brown, Paul J. Myers, Sara J. Adair, Jason R. Pitarresi, Shiv K. Sah-Teli, Logan A. Campbell, William S. Hart, Michelle Barbeau, Kelsey Leong, Nicholas Seyler, William Kane, Kyoung Eun Lee, Edward Stelow, Marieke Jones, M. Celeste Simon, Peppi Koivunen, Todd W. Bauer, Ben Z. Stanger, Matthew J. Lazzara

Supplemental Methods – Data Analytics and Computational Modeling

Immune deconvolution of TCGA RNA-seq data

Cell-type-specific immune deconvolution of bulk TCGA PAAD data was performed using *immunedeconv* and the EPIC algorithm to estimate absolute fractions of cell types.

Partial correlations with pan-cancer EMT enrichment

Partial rank correlation coefficients and confidence intervals were computed using *ggstatsplot*. Partial correlations were computed with respect to GSVA scores for the mesenchymal portion of the pcEMT signature, for CPTAC global proteomics or TCGA PAAD RNA-seq data.

Optimal NMF factorization rank

Optimal NMF factorization rank *k* was selected as previously described (1). First, a range of clusters from *k* = 2 to 10 was tested by: (i) performing 100 iterations of NMF with random initializations of the NMF matrices *W* (basis component matrix) and *H* (mixture coefficient matrix); (ii) calculating the product of the cophenetic correlation coefficient, the dispersion coefficient of the consensus matrix, and the average silhouette width of the consensus matrix for each *k*; and (iii) selecting the optimal *k* with the maximum product of the cophenetic, dispersion, and average silhouette coefficients. Then, using the optimal *k*, the final NMF clustering was obtained by repeating the analysis with 500 iterations of random initializations of matrices *W* and *H*. The coefficient matrix *H* was used to assign samples (tumors) to clusters by identifying the cluster (row of *H*) for which each sample (column of *H*) had its maximum mixture coefficient.

Linear modeling of scRNA-seq data

Least absolute shrinkage and selection operator (LASSO) regression was performed using *glmnet*. The regularization parameter λ was determined via cross-validation using the "cv.glmnet" function and by taking the largest λ such that cross-validated mean-squared error (MSE) was within one standard error of the minimum MSE. An ordinary least squares linear regression model was then trained using the LASSO-selected KEGG pathways and subjected to further variable selection by minimizing the Akaike information criterion (AIC) using the "step" R function. Model statistics were calculated using the base R "summary" function and plotted using *ggstatsplot*.

Supplemental Methods – Experimental

Antibodies and nuclear stain

For immunofluorescence, antibodies against HIF-1α (CST, catalog no. 79233, RRID:AB_2799924), vimentin (Santa Cruz Biotechnology, SCBT, catalog no. sc-373717, RRID:AB_10917747), Ki67 (CST, catalog no. 9449, RRID:AB_2797703), H3K36me2 (CST, catalog no. 2901, RRID:AB_1030983), and NSD2 (SCBT, catalog no. sc-365627, RRID:AB_10844830) were used.

For immunoblotting, antibodies against HIF-1α (Novus Biologics, catalog no. NB100-134), HIF-2α (Novus Biologics, catalog no. NB100-122), vimentin (SCBT, catalog no. sc-373717, RRID:AB_10917747), pc-Jun S73 (CST, catalog no. 3270, RRID:AB_2129575), pERK T202/Y204 (CST, catalog no. 4370, RRID:AB_2315112), ERK1/2 (CST, catalog no. 4695, RRID:AB_390779), p-p38 T180/Y182 (CST, catalog no. 4511, RRID:AB_2139682), and GAPDH (SCBT, catalog no. sc-32233, RRID:AB_627679) were used.

Antibodies against E-cadherin (clone ECCD2, Invitrogen, catalog no. 13-1900) and c-Jun (Cell Signal Technology, CST, catalog no. 9165, RRID:AB_2130165) were used for immunofluorescence and immunoblotting.

Alexa488-conjugated vimentin antibody (SCBT, catalog no. sc-373717) was used for flow cytometry and fluorescent immunohistochemistry for PDX and HPAF-II tumors. For KPCY tumors, antibody against vimentin (CST, catalog no. 5741, RRID:AB_10695459) was used.

Antibodies against E-cadherin (clone ECCD2, Takara, catalog no. M108, RRID:AB_2895157), c-Jun (CST, catalog no. 9165, RRID:AB_2130165), pERK T202/Y204 (CST, catalog no. 4370, RRID:AB_2315112), CD-31 (BioLegend, catalog no. 102501, RRID:AB_312908), α-smooth muscle actin (R&D Systems, catalog no. MAB1420, RRID:AB_262054), GFP (Abcam, catalog no. ab6673, RRID:AB_305643), RFP (Rockland, catalog no. 600-401-379, RRID:AB_2209751), podoplanin (BioLegend, catalog no. 127401, RRID:AB_1089187), and Hypoxyprobe™Red549 (Hypoxyprobe, catalog no. HP7-100Kit) were used for immunohistochemistry.

Hoechst 33342 (Invitrogen, catalog no. H1399) was used for nuclear stain.

Immunoblotting

Cells were lysed using a standard cell extraction buffer (Invitrogen, catalog no. FNN0011) with protease and phosphatase inhibitors (Sigma-Aldrich catalog nos. P8340, P5726, P0044). Crude lysates were centrifuged at 14,000 rpm for 10 min at 4°C, and supernatants were removed as clarified lysates. Total protein concentration was determined with a micro-bicinchoninic acid (BCA) assay (Pierce). To prepare samples for electrophoresis, equal protein amounts were combined with 10× NuPAGE reducing agent, 4× LDS sample buffer and MilliQ water to reach equal sample volumes. Samples were then heated at 100°C for 10 min and loaded onto 1.5 mm NuPAGE gradient (4-12%) gels (Invitrogen, catalog no. NP0336BOX). Gels were transferred to 0.2 μm nitrocellulose membranes using the TransBlot Turbo Transfer System (BioRad). Membranes were blocked with diluted IBB for 1 hr on an orbital shaker. Membranes were incubated with primary antibodies at 1:1000 in IBB overnight at 4°C. GAPDH was used as a loading control. Membranes were washed with shaking three times for 5 min with 0.1% Tween-20 in PBS and then incubated with secondary antibodies at 1:10,000 in IBB with

shaking for 2 hr at room temperature. For HIF-1α and HIF-2α antibodies, 5% non-fat milk in 1× Tris-buffered saline + 0.1% Tween-20 was used for blocking and antibody dilution. Membranes were washed with 0.1% Tween-20 in PBS prior to imaging on a LICOR Odyssey CLx. Membranes were stripped with 0.2 M NaOH, with confirmation by re-imaging. Image Studio (LICOR, Version 5.2.5) was used for densitometry.

Coverslip immunofluorescence

Cells were grown on 18-mm glass coverslips, fixed with 4% paraformaldehyde in PBS for 20 min, and permeabilized with 0.25% Triton X-100 in PBS for 5 min. Coverslips were incubated with primary antibodies in a humidified chamber overnight at 4°C. Following five washes with 0.1% Tween 20 in PBS, coverslips were incubated for 1 hr at 37°C in a humidified chamber with Alexa Fluor secondary antibodies and Hoechst. Antibodies were used at manufacturer-recommended dilutions in IBB, with minor exceptions. For immunofluorescence, E-cadherin and vimentin antibodies were used at 1:500 and 1:250 dilutions, respectively. Washed coverslips were mounted on glass slides with ProLong Gold Antifade Mountant.

Fluorescence microscopy and image analysis

Individual cells were identified based on a nuclear primary object. For junctional E-cadherin, mean edge intensities were measured. For percent-positive measurements (e.g., vimentin), a threshold for positive signal was based on a secondary-only control applied to all images. To measure cell neighbors, the *Measure Object Neighbors* module was applied based on E-cadherin signal, and percentages of neighbors were binned based on inspection of a histogram into “low”, “medium”, and “high”, with the plots displaying the percentage of cells with a low number of neighbors, as defined by less than half of the cell border touching another cell. For intensity measurements, the mean intensity per positive object was quantified.

Quantitative reverse transcription PCR (qRT-PCR)

RNA was extracted using the RNeasy Kit (Qiagen) and reverse-transcribed using High-Capacity cDNA Reverse Transcription Kit (Applied Biosciences). qRT-PCR was performed using PowerUp SYBR Green (Applied Biosciences) per manufacturer protocol using a QuantStudio3 system (Applied Biosystems). TaqMan™ Array Human Endogenous Control (Applied Biosciences) with 32 potential housekeeping genes was run in triplicate with RNA from HPAF-II cells cultured in 21 or 1% O_2 for 120 hr. This showed that *CASC3* did not change significantly in response to hypoxia. Measurements were analyzed with the ddCt method. Data are displayed as normalized fold-changes, using *CASC3* as a housekeeping gene. Primer sequences are provided in **Supp Table S3**.

Cell scatter measurements

Cell scatter measurements were based on changes in the shape factor of clusters of HPAF-II cells engineered with constitutive GFP expression and using an approach previously described (2). GFP-expressing HPAF-II cells were engineered via second-generation lentiviral transfection of LX293T cells (Takara) using pLX302-EGFP plasmid (Kevin Janes, University of Virginia), with pCMV-VSVG and pCMV-delta8.2 packaging plasmids. Cells were sparsely seeded in a 24-well plate. 48 hr later, t = 0 images were taken, and samples were maintained in

21% O_2 or moved to 1% O_2 for 96 hr. Individual cell clusters (≤ 20 cells by endpoint) were imaged over time, six wells per condition. Using ImageJ (Fiji for Mac OS X, Version 2.1.0), GFP signal was used to create a binary cluster mask to determine area and perimeter and quantify the shape factor = 4π(area/perimenter^2), where a circle = 1.

Embedding and sectioning of murine tumors

PDX tumors -- Most sections shown come from tumors that were fixed in 10% zinc-buffered formalin for 24 hr, transferred to 70% ethanol, then paraffin embedded. For sections stained for CD31, frozen sections were prepared by fixing tumors in 4% paraformaldehyde for 1-3 hr, incubating in 30% sucrose overnight, and embedding in OCT. 4-5 µm sections were cut on charged slides for paraffin-embedded or frozen tumors. The UVA Research Histology Core performed embedding, sectioning, and Hematoxylin/eosin (H&E) staining.

Autochthonous KPCY and subcutaneous tumors -- For both tumor types, excised tissues were fixed in zinc formalin and paraffin-embedded prior to staining.

HPAF-II hypoxia fate-mapping tumors -- Paraffin embedding and sectioning were performed as described for PDX tumors. The UVA Research Histology Core performed embedding, sectioning, and H&E staining.

Immunohistochemistry

Slides were antigen-retrieved at the UVA Biorepository and Tissue Research Facility, permeabilized with 0.1% Triton X-100 in PBS for 20 min and blocked with Intercept Blocking Buffer (IBB) (LICOR) for 1 hr. Slides were incubated with primary antibodies diluted in IBB overnight at 4°C and then PBS-washed and incubated with secondary antibodies in IBB for 2 hr at room temperature. For E-cadherin, blocking was with 5% donkey serum in 0.3% Triton X-100 in PBS. Slides were then washed twice with 0.1% Tween-20 in PBS for 5 min each, incubated with secondary antibodies for 1 hr at room temperature, and then washed again with 0.1% Tween-20 in PBS for 5 min in the dark. Washed slides were mounted with ProLong Gold Antifade Mountant (Invitrogen).

Flow cytometry for vimentin

Cytometry was performed on a BD/Cytek FACS Calibur at the UVA Flow Cytometry Core Facility. FCS Express 7 was used for data analysis. Cells were dissociated with 0.25% Trypsin EDTA, fixed in 4% paraformaldehyde, and permeabilized with 0.25% Triton X-100. Washed cells were then incubated with conjugated antibody for 30 min in the dark, and cells were resuspended in 0.1% FBS in PBS. Forward and side scatter were used to identify intact single cells, and main figure data represent only single-cell events. 20,000 cells were counted per biological replicate, with gates based on unstained controls.

RNA extraction and RNA-sequencing of patient-derived xenografts

Human pancreatic cancer samples were obtained in accordance with a University of Virginia IRB for Health Sciences Research under the direction of Dr. Todd Bauer. Primary PDX tumors were grown, as previously described (3). Upon harvest, tumors were stored in Qiagen AllProtect at -80°C. Samples were processed using Qiagen Tissuelyser LT along with Qiagen AllPrep DNA/RNA extraction kit. Samples were quantified and quality control was performed

before libraries were prepared using polyA capture and cDNA reverse transcription. Libraries were sequenced on Illumina platform PE150 at a read depth of 40 million reads (Novogene Corp., Chula Vista, CA).

Patient-derived xenograft tissue microarray

A tissue microarray was created by the UVA Biorepository & Tissue Research Facility using paraffin-embedded PDX tumors, PDX-derived cell lines, HPAF-II cells, MiaPaca2 cells, and normal pancreas. Antigen retrieval was performed by the UVA Biorepository & Tissue Research Facility, and the slide was stained per the immunohistochemistry protocol previously described. The microarray was imaged using Cytation5 (BioTek) with a 10× objective.

Cell engineering for hypoxia fate mapping

LX293T cells were transfected with the CMV-loxp-DsRed-loxp-eGFP or 4xHRE-MinTK-CRE-ODD plasmid and the psPAX2 and pMD2.G packaging plasmids. CMV-loxp-DsRed-loxp-eGFP and 4xHRE-MinTK-CRE-ODD were created by Dr. Daniele Gilkes (Addgene plasmid #141148 and #141147; RRID:Addgene_141148 and RRID:Addgene_141147). psPAX2 and pMD2.G were provided by Dr. Didier Trono (Addgene plasmid #12260 and #12259; RRID:Addgene_12260 and RRID:Addgene_12259). Polyjet (SignaGen) was used to increase transfection efficiency. HPAF-II cells were first transduced with filtered viral supernatant from LX293T cells transfected with CMV-loxp-DsRed-loxp-eGFP and 8 μg/mL polybrene. After selection in zeocin (Gibco), cells were transduced with filtered viral supernatant from LX293T cells transfected with 4xHRE-MinTK-CRE-ODD and 8 μg/mL polybrene. HPAF-II cells were then cultured in 5% O_2 and single-cell sorted into 96-well plates, with removal of any GFP+ cells, using a Becton Dickinson Influx Cell Sorter by the UVA Flow Cytometry Core Facility. Parental HPAF-II cells were used to set gates. Single-cell clones were grown in medium conditioned by parental HPAF-II cells and supplemented with an additional 10% fresh FBS. Confluent clone-containing wells were split into three plates, maintained at 21, 3, or 1% O_2. Plates were imaged using a Cytation5 (BioTek, 10× objective) to screen for clones exhibiting increased GFP at 1% O_2 only. The selected clone was confirmed in larger well format to lose DsRed in 1% O_2 and to express vimentin in response to hypoxia or growth factors as observed in parental HPAF-II cells.

Dissociation and cytometry for HPAF-II hypoxia fate-mapping tumors

For 50 mg of tumor reserved on ice, 2 mL of protease solution [5mM $CaCl_2$, 10 mg/mL *Bacillus Licheniformis* protease, and 125 U/mL DNAseI in Dulbecco's phosphate-buffered saline (DPBS)] was used. Tumors were minced over ice in solution and then mechanically dissociated for 8 min using a 1 mL pipet. Samples were transferred to Miltenyi C-tubes and run on the gentleMACS tumor_01 program three times. Afterwards, cells were mechanically dissociated for 2 min using a 1 mL pipet. Cells were suspended in 10% FBS and EDTA in DPBS and centrifuged at 1200 g and 4°C for 5 min. Resuspended viable (ToPro3-negative) cells were sorted using a Becton Dickinson Influx Cell Sorter at the UVA Flow Cytometry Core Facility, with parental HPAF-II cells and engineered HPAF-II hypoxia fate-mapping cells as controls. For each tumor, cells were sorted into DsRed+, GFP+, and DsRed+/GFP+ populations and plated in complete RPMI following sorting.

Five-channel confocal microscopy

Image acquisition was performed on a Zeiss LSM 880 confocal microscope using 405, 488, 561, and 633 nm laser lines and a Plan-Apochromat 20×/0.8 M27 objective. Signals were deconvoluted using spectral unmixing based on lambda stacks of singly-stained and unstained tissue sections. The gallium arsenide phosphide (GaAsP) spectral array detector was tuned to 8.9 nm to obtain 32-channel images ranging from 411 to 696 nm from which emission spectra for each of the fluorochromes were obtained. The spectral fingerprints from each of the fluorophores and from tissue autofluorescence were then used in the “online fingerprinting” mode of the ZEN Black imaging software.

Growth factors

Recombinant human HGF and TGFβ were from Peprotech. Complete medium containing growth factors was replenished every 48 hr.

Inhibitors

Inhibitors and concentrations were as follows: 10 μM SFK inhibitor PP2 (Sigma-Aldrich), 5 μM PP2A inhibitor LB-100 (Selleck Chem), 1.5 μM PP2Cδ inhibitor sanguinarine chloride (MedChemExpress), 1 μM MEK inhibitor CI-1040 (LC Laboratories), 10 μM JNK inhibitor SP600125 (LC Laboratories), 10 μM p38 inhibitor SB203580 (LC Laboratories), and 10 μM TGFβRI inhibitor galunisertib (Selleck Chem). Inhibitor stocks were prepared in DMSO.

Dosing of PDX tumor-bearing mice with kinase inhibitors

Where kinase inhibitors were used, mice were treated with selumetinib (2.5 mg/kg, orally, twice daily; Selleck Chem), SP600125 (12 mg/kg, IP, twice daily; LC Laboratories), selumetinib+SP600125, or vehicle control. For oral dosing, vehicle was 0.5% hydroxypropylmethylcellulose + 0.1% Tween 80 in water. For IP dosing, vehicle was 5% DMSO + 15% Tween 20 in water.

Phospho-kinase and receptor tyrosine kinase arrays

The Proteome Profiler Human Phospho-Kinase Array, which covers 37 phosphorylated kinases and 2 total proteins, was purchased from R&D Systems (catalog no. ARY003C). Lysates were prepared per manufacturer protocol. The array was developed on film at multiple exposures (30 sec, 1 min, 3 min, 5 min, 7.5 min, 10 min) and imaged using a GS-800 Densitometer (Bio-Rad). The Human Receptor Tyrosine Kinase Phosphorylation Array, which covers 71 targets, was purchased from RayBiotech (catalog no. AAH-PRTK-G1). Lysates were prepared per manufacturer protocol. After incubation with cell lysates, the array was shipped to RayBiotech for scanning and data extraction.

Luminex

HPAF-II cells were cultured for 120 hr in 21% or 1% O_2. Media was collected and passed through a 0.4 μm filter. A Luminex assay of human cytokines was performed on the conditioned media by the UVA Flow Cytometry Core Facility.

siRNA-mediated knockdowns

siRNAs against HIF-1α (catalog no. sc-35561), EPAS-1/HIF-2α (catalog no. sc-35316), c-Jun (catalog no. sc-29223), and NSD2 (catalog no. sc-61233) and a control siRNA (catalog no. sc-37007) were purchased from Santa Cruz Biotechnology. siRNA against ERK 1/2 (catalog no. 6560) was from Cell Signal Technology. Lipofectamine RNAiMAX (Thermo Fisher) was used per manufacturer recommendations. Cells were transfected 24 hr after plating and subjected to any treatment or hypoxic culture 24 hr after transfection.

shRNA-mediated knockdowns

pLKO.1 plasmids encoding two non-overlapping shRNAs targeting *HIF1A* (catalog nos. TRCN0000003810 and TRCN0000010819), *EPAS1* (HIF-2α) (catalog nos. TRCN0000003805 and TRCN0000003806), *ERK2* (catalog nos. TRCN0000010040 and TRCN0000010050), *JUN* (catalog nos. TRCN0000010366 and TRCN0000039590), or a scrambled control (catalog no. SHC016), were purchased from Sigma-Aldrich. *HIF1A* and *ERK2* plasmids encoded puromycin resistance, and *EPAS1* and *JUN* plasmids encoded neomycin resistance. Second-generation lentiviral transfection was performed in LX293T cells (Takara) with pCMV-VSVG and pCMV-delta8.2 packaging plasmids. HPAF-II cells were transduced with filtered viral supernatant with 8 μg/mL polybrene for puromycin-containing plasmids and selected, then transduced with viral supernatant for neomycin-containing plasmids and selected.

KDM2A kinetic assays

The *KDM2A* gene fused to an N-terminal FLAG tag was excised from pcDNA-FLAG-KDM2A (Jing-Yi Chen, I-Shou University) by restriction digest with SalI-HF and XbaI, isolated by QIAquick gel extraction (Qiagen), and inserted into pFastBac1 using the same restriction sites (Mark Yeager, University of Virginia). The final plasmid was verified by Sanger sequencing (Eurofins).

Kinetic assays were performed as previously described with some modifications (4). KDM2A bacmids were generated using DH10Bac competent *E.coli* cells with the standard Bac-to-Bac protocol (Invitrogen). Baculoviruses were generated by transducing the bacmid DNA into Sf9 insect cells using the flashBACTM System (Oxford Expression Technologies). Recombinant proteins were produced by infecting Sf21 insect cells with the baculoviruses for 72 hr at 27°C. Cells were homogenized in pH 7.8 buffer containing 10 mM Tris, 150 mM NaCl, 100 mM glycine, 0.1% (v/v) Triton X-100, and a protease inhibitor cocktail tablet without EDTA. Cell lysates were centrifuged at 21,000 g for 30 min, and the soluble fractions containing the FLAG-tagged KDM2A protein were affinity purified using the anti-FLAG M2 affinity gel (Sigma). Gel beads were washed with TBS buffer (50 mM Tris, 150 mM NaCl, pH 7.4, protease inhibitor cocktail tablet without EDTA), and proteins were eluted with TBS buffer containing 150 μg/mL FLAG-peptide. Eluted fractions were analyzed by SDS-PAGE with Coomassie blue and immunoblotting using anti-FLAG M2 antibody (Sigma). Protein concentration was measured by Nanodrop, and protein was aliquoted and stored at -70°C.

Optimum reaction time and pH were first determined for KDM2A-catalyzed reactions. 50 μL reactions consisted of 50 mM Tris-HCl, pH 8.8, 2 mg/mL BSA (Roche), 60 μg/mL catalase (Sigma), 0.1 mM DTT, 2 mM sodium ascorbate, 10% v/v DMSO and 0.4 μM of affinity-purified KDM2A enzyme. To determine K_M for histone peptide substrate H3K36me2 ((NH2-)ATKAARKSAPATGGV-(K-Me2)-KPHRYRP-GG(K-Biotin) (-CONH2)) (Innovagen), 2-oxo [1-

^{14}C] glutarate (2-OG) (Perkin-Elmer), Fe^{2+}, and O_2, enzymatic reactions were carried out by varying the concentration of the component in question while keeping the concentration of others saturating and constant. The experiment to calculate K_M for O_2 was performed at six oxygen concentrations in an InVivo400 hypoxia workstation (Ruskinn). Enzymatic reactions were carried out at 37°C for 30 min, and reactions were stopped with 100 µL of 1 M KH_2PO_4, pH 5. ^{14}C-labeled CO_2 generated during reactions was counted using a Tri-carb 2900TR scintillation device (Perkin-Elmer). K_M values were calculated from Michaelis-Menten saturation curves and Lineweaver-Burk plots using Graphpad Prism. The turnover rate of the enzyme (k_{cat}) was calculated using V_{max} values obtained from Michaelis-Menten curves.

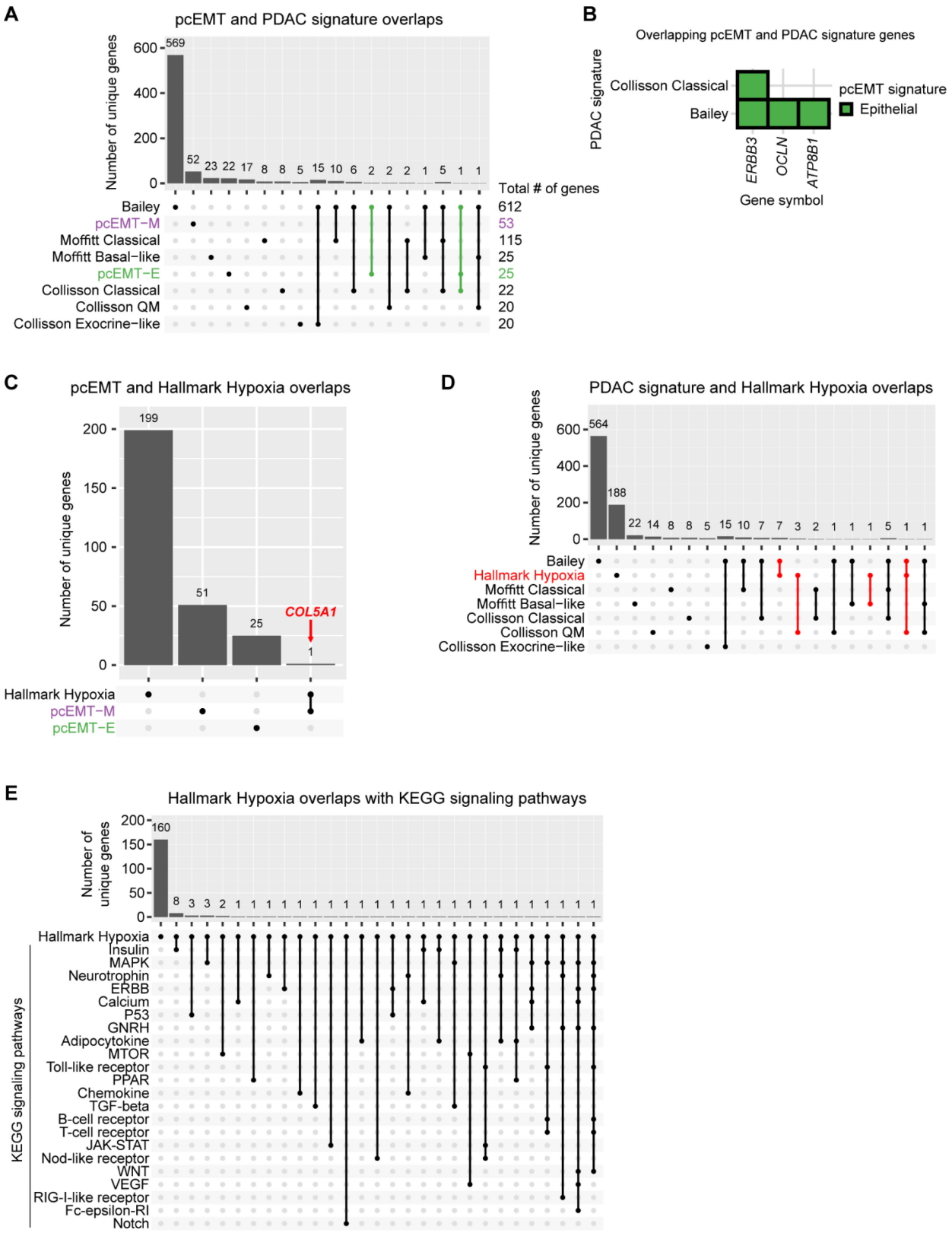

Supp Figure S1. There is little overlap among the pan-cancer EMT (pcEMT), Hallmark Hypoxia, and established PDAC subtype gene signatures. (A) An UpSet plot shows the

number of unique genes for comparisons made among the pcEMT signature and Collisson, Moffitt, and Bailey PDAC signatures. Note that subtypes are not shown for the Bailey PDAC signature because the genes defining each subtype were not explicitly defined by the original authors. UpSet plots were formatted left to right to show entries for single gene sets (which reflect the number of genes unique to those gene sets alone) followed by entries showing intersections across gene sets, with each type of entry arranged in rank order by cardinality. Bars are highlighted in green where at least one other gene set shares one or more gene features with the epithelial component of the pcEMT signature (pcEMT-E). **(B)** pcEMT genes overlapping with the indicated PDAC signatures are shown. **(C)** An UpSet plot was created for the pcEMT-E, pcEMT-M, and Hallmark Hypoxia gene sets Only *COL5A1* is common to the pcEMT-M and Hallmark Hypoxia gene sets. **(D)** An UpSet plot was created for comparisons among the Hallmark Hypoxia, Bailey, Collison, and Moffitt gene sets. Bars are highlighted in red where at least one other gene set shares one or more gene features with the Hallmark Hypoxia gene set. **(E)** An UpSet plot was created for comparisons among the Hallmark Hypoxia and indicated KEGG signaling pathway gene sets.

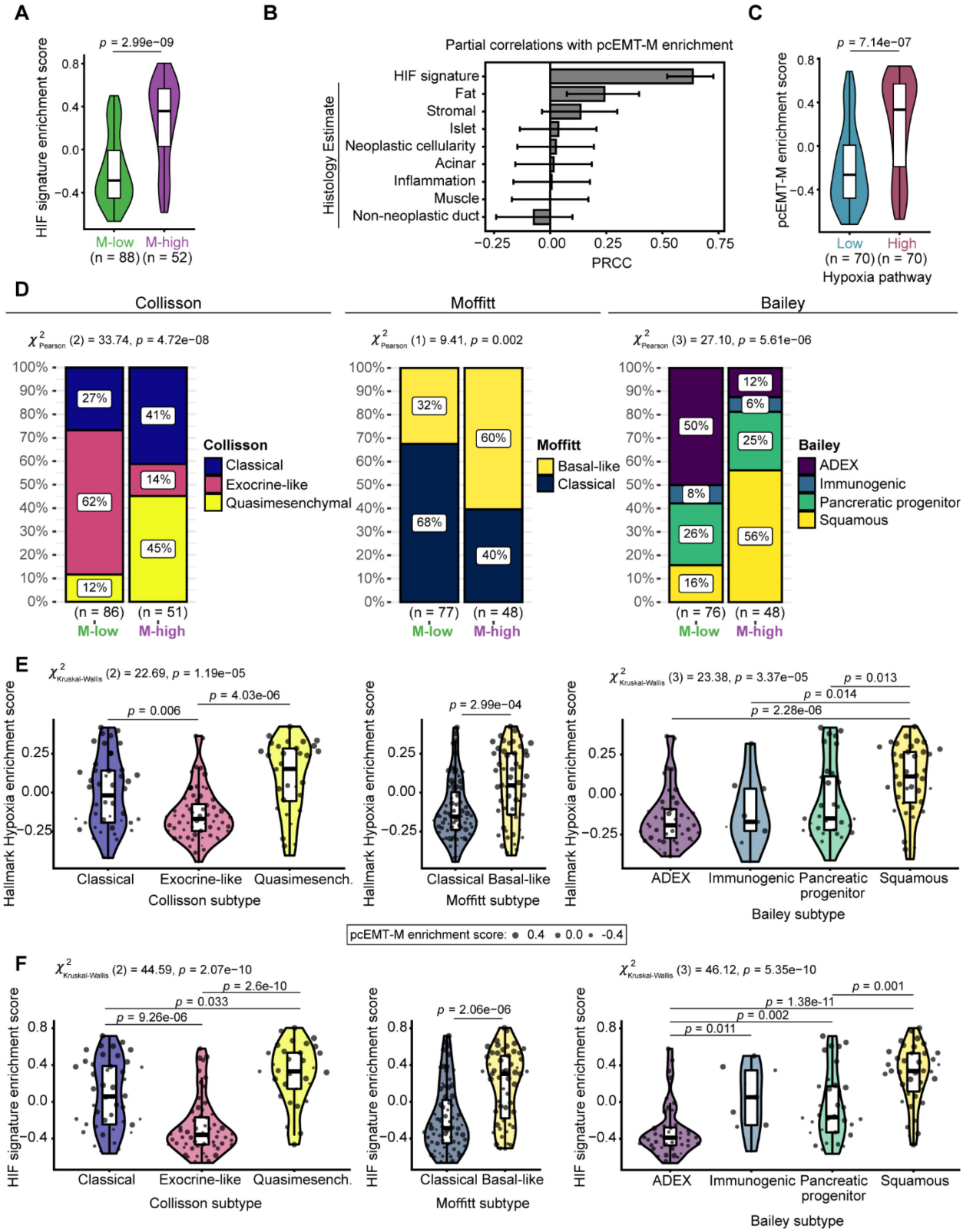
A
p = 2.99e−09
HIF signature enrichment score
M-low
M-high
(n = 88)
(n = 52)
B
Partial correlations with pcEMT-M enrichment
Histology Estimate
HIF signature
Fat
Stromal
Islet
Neoplastic cellularity
Acinar
Inflammation
Muscle
Non-neoplastic duct
PRCC
C
p = 7.14e−07
pcEMT-M enrichment score
Low
High
(n = 70)
(n = 70)
Hypoxia pathway
D
Collisson
Moffitt
Bailey
Collisson
Classical
Exocrine-like
Quasimesenchymal
Moffitt
Basal-like
Classical
Bailey
ADEX
Immunogenic
Pancreatic progenitor
Squamous
M-low
M-high
E
Hallmark Hypoxia enrichment score
Collisson subtype
Moffitt subtype
Bailey subtype
Classical
Exocrine-like
Quasimesench.
Classical Basal-like
ADEX
Immunogenic
Pancreatic progenitor
Squamous
pcEMT-M enrichment score: 0.4 0.0 -0.4
F
HIF signature enrichment score
Collisson subtype
Moffitt subtype
Bailey subtype

Supp Figure S2. Across different classification schemes, aggressive PDAC subtypes are correlated with an increase in hypoxic gene signatures. (A) CPTAC PDAC tumor proteomics data were clustered by non-negative matrix factorization using the protein analogs of the pcEMT signature as features, as shown in Figure 1. HIF signature GSVA enrichment scores were calculated for the resulting clusters of mesenchymal-high (M-high) and mesenchymal-low (M-low) tumors, with a Mann-Whitney U test. **(B)** Partial rank correlation coefficients (PRCCs) of the indicated variables were calculated with respect to protein enrichment (GSVA) scores for the mesenchymal portion of the pcEMT signature (pcEMT-M). HIF signature enrichment scores were calculated from the CPTAC PDAC global proteomics data using GSVA. Histology estimates were used as provided with the CPTAC data. Error bars denote 95% confidence intervals. **(C)** Protein enrichment of pcEMT-M was computed by GSVA and compared between hypoxia-high and hypoxia-low CPTAC PDAC tumors. Hypoxia status was used as previously described (1), with a Mann-Whitney U test. **(D)** Comparisons are shown of Collisson, Moffitt, and Bailey subtype proportions across pcEMT M-low and -high tumor groups for CPTAC PDAC tumors. Collisson, Moffitt, and Bailey subtype classifications were used as reported previously (1). The results of Pearson's chi-squared test comparing the proportions of PDAC subtypes between the two pcEMT groups are shown above each plot. **(E)** Hallmark Hypoxia GSVA enrichment scores were calculated from protein expression of CPTAC PDAC tumors and compared across subtypes within the Collisson, Moffitt, and Bailey classification systems. Results of the Kruskal-Wallis test or Mann-Whitney U test are shown above each plot. Pairwise comparisons for the Collisson and Bailey subtypes were computed using the Dunn test. **(F)** HIF signature GSVA scores were calculated from protein expression of CPTAC PDAC tumors and compared across subtypes within the Collisson, Moffitt, and Bailey classification systems. The size of dots in (E) and (F) indicates the pcEMT-M enrichment score for each tumor. Results of the Kruskal-Wallis test or Mann-Whitney U test are shown above each plot. Pairwise comparisons for the Collisson and Bailey comparisons were computed using the Dunn test.

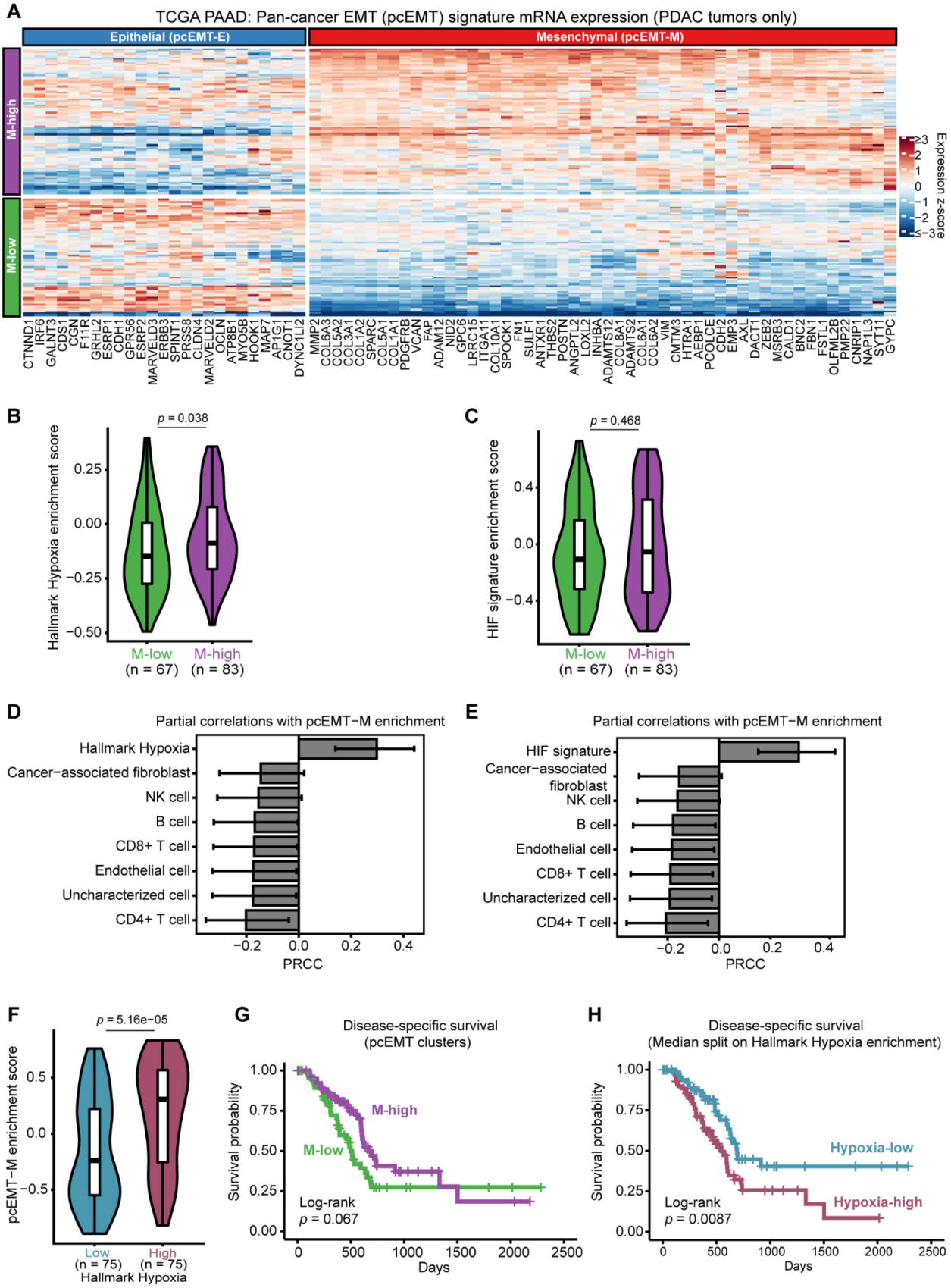
A
TCGA PAAD: Pan-cancer EMT (pcEMT) signature mRNA expression (PDAC tumors only)
Epithelial (pcEMT-E)
Mesenchymal (pcEMT-M)
M-high
M-low
Expression z-score
≥3
2
1
0
−1
−2
≤−3
CTNND1 IRF6 GALNT3 CDS1 CGN F11R GRHL2 ESRP1 CDH1 GPR56 ESRP2 MARVELD3 ERBB3 SPINT1 PRSS8 CLDN4 MARVELD2 OCLN ATP8B1 MYO5B HOOK1 MAP7 AP1G1 CNOT1 DYNC1LI2
MMP2 COL6A3 COL5A2 COL3A1 COL1A2 SPARC COL5A1 COL1A1 PDGFRB VCAN FAP ADAM12 NID2 GPC6 LRRC15 ITGA11 COL10A1 SPOCK1 FN1 SULF1 ANTXR1 THBS2 POSTN ANGPTL2 LOXL2 INHBA ADAMTS12 COL8A1 ADAMTS2 COL6A1 COL6A2 VIM CMTM3 HTRA1 AEBP1 PCOLCE CDH2 EMP3 AXL DACT1 ZEB2 MSRB3 CALD1 BNC2 FBN1 FSTL1 OLFML2B PMP22 CNRIP1 NAP1L3 SYT11 GYPC
B
p = 0.038
Hallmark Hypoxia enrichment score
0.25
0.00
−0.25
−0.50
M-low (n = 67)
M-high (n = 83)
C
p = 0.468
HIF signature enrichment score
0.4
0.0
−0.4
M-low (n = 67)
M-high (n = 83)
D
Partial correlations with pcEMT−M enrichment
Hallmark Hypoxia
Cancer−associated fibroblast
NK cell
B cell
CD8+ T cell
Endothelial cell
Uncharacterized cell
CD4+ T cell
−0.2
0.0
0.2
0.4
PRCC
E
Partial correlations with pcEMT−M enrichment
HIF signature
Cancer−associated fibroblast
NK cell
B cell
Endothelial cell
CD8+ T cell
Uncharacterized cell
CD4+ T cell
−0.2
0.0
0.2
0.4
PRCC
F
p = 5.16e−05
pcEMT−M enrichment score
0.5
0.0
−0.5
Low (n = 75)
High (n = 75)
Hallmark Hypoxia
G
Disease-specific survival
(pcEMT clusters)
Survival probability
1.00
0.75
0.50
0.25
0.00
M-high
M-low
Log-rank
p = 0.067
0
500
1000
1500
2000
2500
Days
H
Disease-specific survival
(Median split on Hallmark Hypoxia enrichment)
Survival probability
1.00
0.75
0.50
0.25
0.00
Hypoxia-low
Hypoxia-high
Log-rank
p = 0.0087
0
500
1000
1500
2000
2500
Days

Supp Figure S3. EMT and hypoxia gene enrichment are correlated in TCGA PDAC tumors. (A) TCGA PAAD tumor samples were clustered using non-negative matrix factorization (NMF) of $\log_2$(TPM+1) expression data for genes from the pan-cancer EMT (pcEMT) signature. Heatmap indicates per-gene, z-scored $\log_2$(TPM+1) expression values. The left vertical side bar indicates the assigned NMF cluster for each tumor. The top horizontal side bar indicates the phenotype associated with each gene as described in the original pcEMT signature (5). **(B)** Hallmark Hypoxia or **(C)** HIF target signature GSVA (enrichment) scores were calculated for TCGA PAAD study PDAC tumors and compared across the NMF-assigned pcEMT clusters. The Mann-Whitney U test indicated that there was a statistically significant difference in medians between the clusters. **(D,E)** Partial rank correlation coefficients (PRCCs) of the indicated TCGA PAAD immune deconvolution cell type estimates (estimated using the EPIC algorithm) and **(D)** Hallmark Hypoxia signature or **(E)** HIF target signature GSVA scores were calculated with respect to GSVA scores for the mesenchymal portion of the pcEMT signature (pcEMT-M). Error bars denote 95% confidence intervals for the indicated PRCCs. **(F)** pcEMT-M GSVA scores were calculated for TCGA PAAD study PDAC tumors and compared when tumors are split into hypoxia-high and hypoxia-low groups based on the median Hallmark Hypoxia GSVA score. **(G)** Kaplan-Meier survival curves were calculated for PDAC patients from the TCGA PAAD study, with stratification based on tumor pcEMT groups from NMF clustering, with log-rank test. **(H)** Kaplan-Meier survival curves were calculated for PDAC patients from the TCGA PAAD study, with stratification based on median Hallmark Hypoxia GSVA score, with log-rank test.

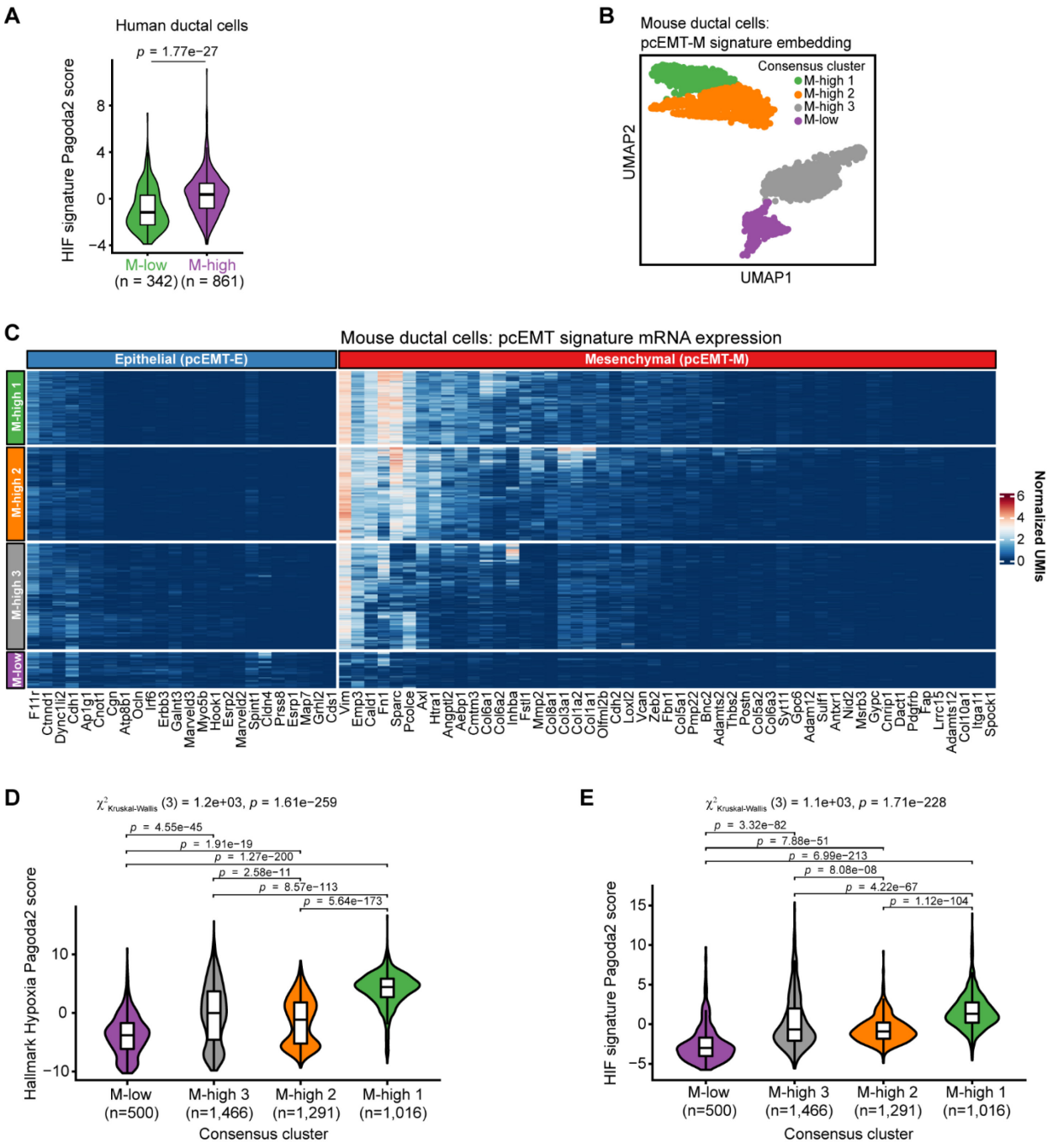

Supp Figure S4. Mesenchymal mouse ductal cells are enriched for hypoxia-associated gene expression. (A) mRNA enrichment of the HIF target signature was compared between M-high and M-low human ductal cells (6) from Figure 1E, with Mann-Whitney U test. **(B)** Mouse ductal cells (6) were projected onto a 2D UMAP embedding of the mesenchymal portion of the pcEMT signature. The UMAP projection was then clustered using consensus clustering, and clusters were labeled by comparing the expression profiles of mesenchymal genes, as shown in (C). **(C)** A heatmap is shown of the consensus cluster-annotated heatmap of mRNA transcript abundances (normalized UMIs) for genes from the full pcEMT signature that are expressed in mouse ductal cells. **(D)** Hallmark Hypoxia Pagoda2 scores were compared across the mouse ductal cell pcEMT consensus clusters. The Kruskall-Wallis test indicated that there was a

statistically significant difference in medians among the distributions. Pairwise comparisons were computed using the Dunn test. **(E)** HIF target signature Pagoda 2 scores were compared across the mouse ductal cell pcEMT consensus clusters. The Kruskall-Wallis test indicated that there was a statistically significant difference in medians among the distributions. Pairwise comparisons in panels (D) and (E) were computed using the Dunn test.

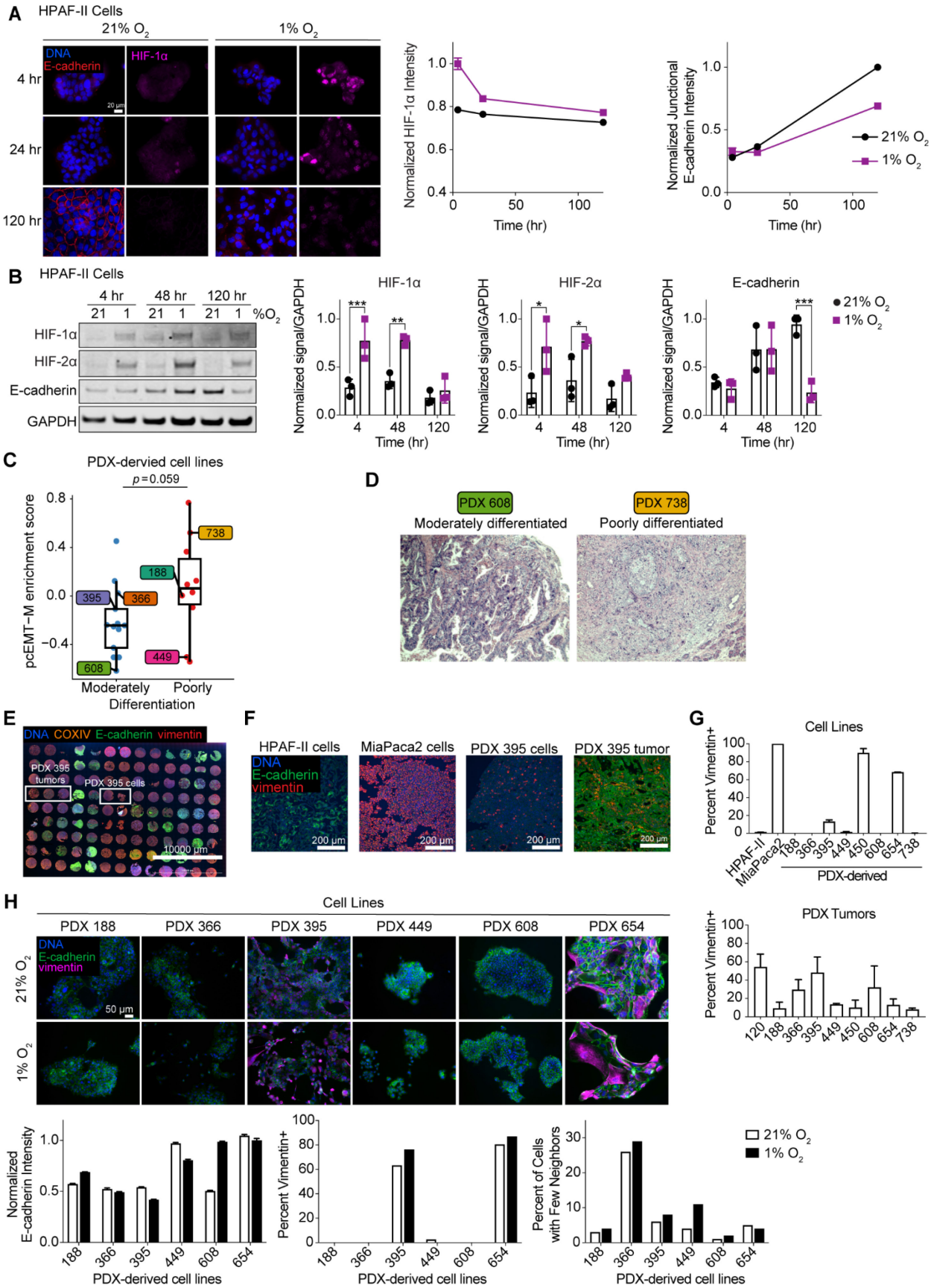
A
HPAF-II Cells
21% O2
1% O2
DNA
E-cadherin
HIF-1α
4 hr
24 hr
120 hr
20 μm
Normalized HIF-1α Intensity
Time (hr)
Normalized Junctional E-cadherin Intensity
21% O2
1% O2
B
HPAF-II Cells
4 hr
48 hr
120 hr
%O2
HIF-1α
HIF-2α
E-cadherin
GAPDH
Normalized signal/GAPDH
Time (hr)
C
PDX-dervied cell lines
p = 0.059
pcEMT−M enrichment score
738
188
395
366
449
608
Moderately Differentiation
Poorly
D
PDX 608
Moderately differentiated
PDX 738
Poorly differentiated
E
DNA COXIV E-cadherin vimentin
PDX 395 tumors
PDX 395 cells
10000 μm
F
HPAF-II cells
MiaPaca2 cells
PDX 395 cells
PDX 395 tumor
DNA
E-cadherin
vimentin
200 μm
G
Cell Lines
Percent Vimentin+
HPAF-II
MiaPaca2
188
366
395
449
450
608
654
738
PDX-derived
PDX Tumors
120
188
366
395
449
450
608
654
738
H
Cell Lines
PDX 188
PDX 366
PDX 395
PDX 449
PDX 608
PDX 654
21% O2
1% O2
DNA
E-cadherin
vimentin
50 μm
Normalized E-cadherin Intensity
Percent Vimentin+
Percent of Cells with Few Neighbors
PDX-derived cell lines
21% O2
1% O2

Supp Figure S5. HIF-1α expression is transient in response to hypoxia, and PDX-derived cell lines exhibit evidence of hypoxia-mediated EMT. (A) HPAF-II cells were cultured in 21% or 1% O_2 for up to 120 hr. At the time points indicated, cells were fixed and stained with antibodies for E-cadherin and HIF-1α. Fluorescence microscopy was performed, with quantitative image analysis for nuclear HIF-1α protein and junctional E-cadherin. Microscopy is shown for three representative time points, *n* = 1, with >1000 cells. A nonlinear regression comparing the parameters for the best fit revealed that one curve could not be used for both datasets, confirming the difference in datasets. **(B)** HPAF-II cells were cultured as in (A) and lysed at the indicated times. Lysates were analyzed by immunoblotting for the indicated proteins, *n* = 3, two-way ANOVA with Sidak's multiple comparisons test to analyze the differences between 21% and 1% O_2 at each time point. **(C)** pcEMT-M signature mRNA enrichment (GSVA scores) was compared for moderately versus poorly differentiated human PDAC patient tumors, with Mann-Whitney U test. GSVA scores were calculated from RNA-seq data obtained from PDX tumors derived from the original patient tumors. **(D)** Representative images of H&E-stained sections of patient tumors used for histological grading of differentiation, with 608 and 738 exemplifying moderately and poorly differentiated tumors, respectively. Images taken with 10× objective, with 10× ocular. **(E)** A tissue microarray of PDX tumors and PDAC cell lines was stained with antibodies for E-cadherin, vimentin, and COXIV (human-specific), and fluorescence microscopy was performed. PDX 395 cell and tumor samples are boxed. **(F)** High-magnification images are shown from the tissue microarray in panel (E) of HPAF-II cells (epithelial baseline), MiaPaca2 cells (mesenchymal baseline), PDX 395 tumor, and the PDX 395-derived cell line. Exposure settings set based on the highest expressing sample to not overexpose; therefore, lower expressing cells may appear to have little to no expression. **(G)** Immunofluorescence microscopy of the tissue microarray was quantified the fraction of COXIV+ cells that were also vimentin+ for both cell lines and PDX tumors. **(H)** PDX-derived cell lines were cultured in 21% or 1% O_2 for 120hr and fixed. Immunofluorescence microscopy was performed for the indicated proteins, and images were quantified for junctional E-cadherin intensity per cell, percent vimentin+ cells, and for percent of cells with low numbers of neighbors (an indication of cell scatter). *n* = 1, with >1000 cells.

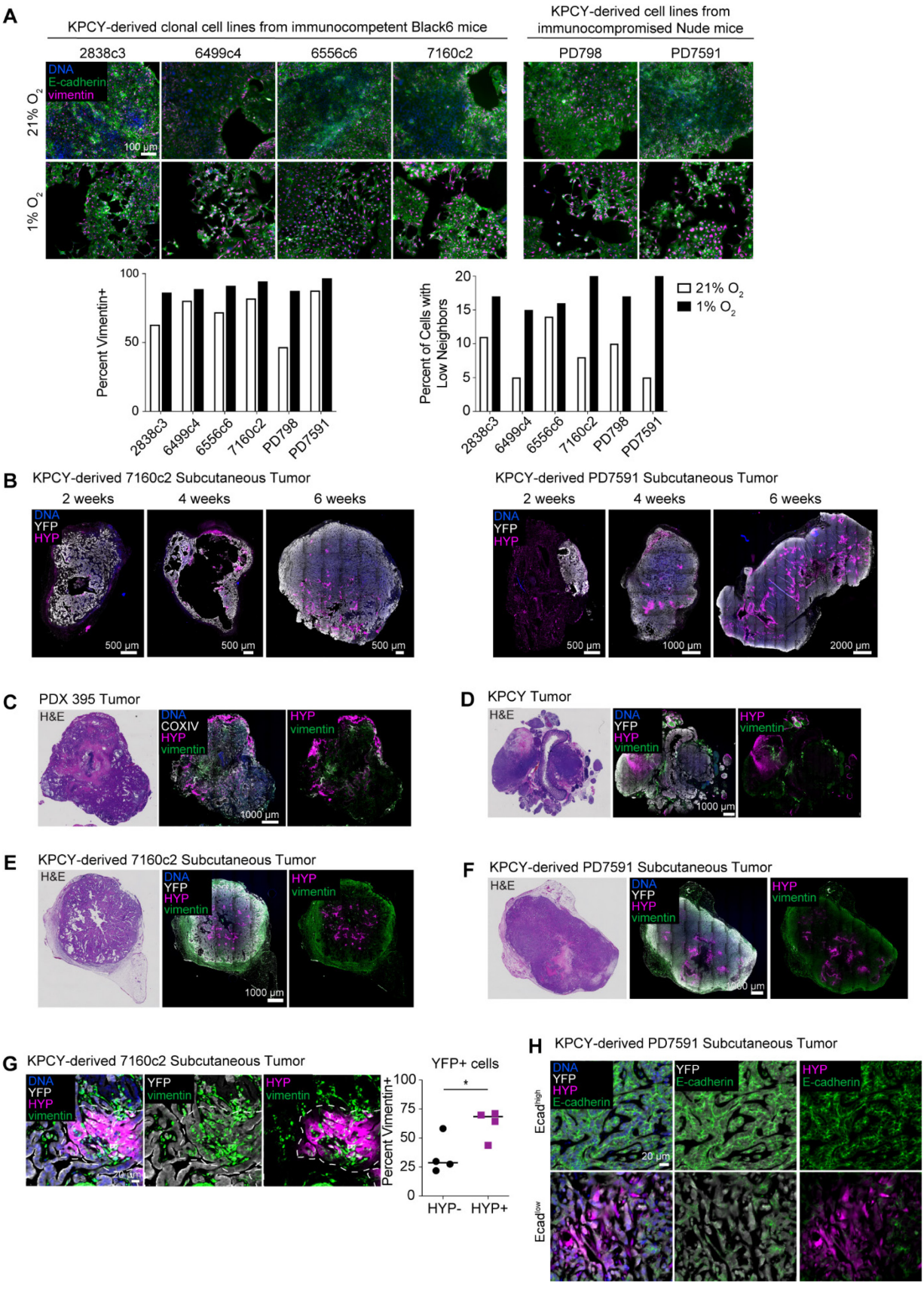
A
KPCY-derived clonal cell lines from immunocompetent Black6 mice
KPCY-derived cell lines from immunocompromised Nude mice
2838c3
6499c4
6556c6
7160c2
PD798
PD7591
DNA
E-cadherin
vimentin
21% O2
1% O2
100 μm
Percent Vimentin+
Percent of Cells with Low Neighbors
21% O2
1% O2
B
KPCY-derived 7160c2 Subcutaneous Tumor
KPCY-derived PD7591 Subcutaneous Tumor
2 weeks
4 weeks
6 weeks
DNA
YFP
HYP
500 μm
1000 μm
2000 μm
C
PDX 395 Tumor
H&E
DNA
COXIV
HYP
vimentin
1000 μm
D
KPCY Tumor
E
KPCY-derived 7160c2 Subcutaneous Tumor
F
KPCY-derived PD7591 Subcutaneous Tumor
G
KPCY-derived 7160c2 Subcutaneous Tumor
YFP+ cells
Percent Vimentin+
HYP-
HYP+
20 μm
H
KPCY-derived PD7591 Subcutaneous Tumor
Ecadhigh
Ecadlow
E-cadherin

Supp Figure S6. KPCY-derived cell lines exhibit evidence of hypoxia-mediated EMT *in vitro* and *in vivo*. (A) KPCY-derived cell lines were cultured in 21% or 1% O_2 for 120 hr, fixed, and stained with antibodies for E-cadherin and vimentin. Immunofluorescence microscopy was performed, with quantitative image analysis to determine the percent of vimentin+ cells and for the percent of cells. with low neighbors, n = 1, with >2000 cells. **(B)** Subcutaneous tumors were formed in mice using KPCY-derived cell lines and allowed to grow for two, four, or six weeks. Fluorescent immunohistochemical staining was performed on tumor sections, which were stained with antibodies for Hypoxyprobe (HYP) and YFP (ductal cells) and imaged, n = 1. **(C)** Sections of orthotopically implanted PDX 395 tumor were subjected to H&E staining or to fluorescent immunohistochemistry using antibodies against COXIV (human specific), vimentin, and HYP. Visible color (H&E) or fluorescence microscopy was performed. Images are representative of n = 4. **(D)** Sections of KPCY autochthonous tumors were subjected to H&E staining and fluorescent immunohistochemistry for YFP, vimentin, and HYP. Microscopy shown is representative of n = 4. **(E, F)** Sections of subcutaneous tumors formed by implanting the KPCY-derived 7160c2 or PD7591 cell line were imaged as described in panel (D). Microscopy shown is representative of n = 4 for 7160c2 or n = 6 for PD7591. **(G)** Sections of subcutaneous tumors generated from 7160c2 cells were stained for HYP, YFP, and vimentin. Fluorescence microscopy was performed, with quantitative image analysis for the fraction of YFP+/HYP- or YFP+/HYP+ cells that were vimentin+. n = 4, t test. * $p < 0.05$ **(H)** Sections of subcutaneous PD7591 tumors were stained for HYP, YFP, and E-cadherin. Representative images show $Ecad^{high}$ and $Ecad^{ow}$ tissue regions, as described in Figure 2I. n = 4.

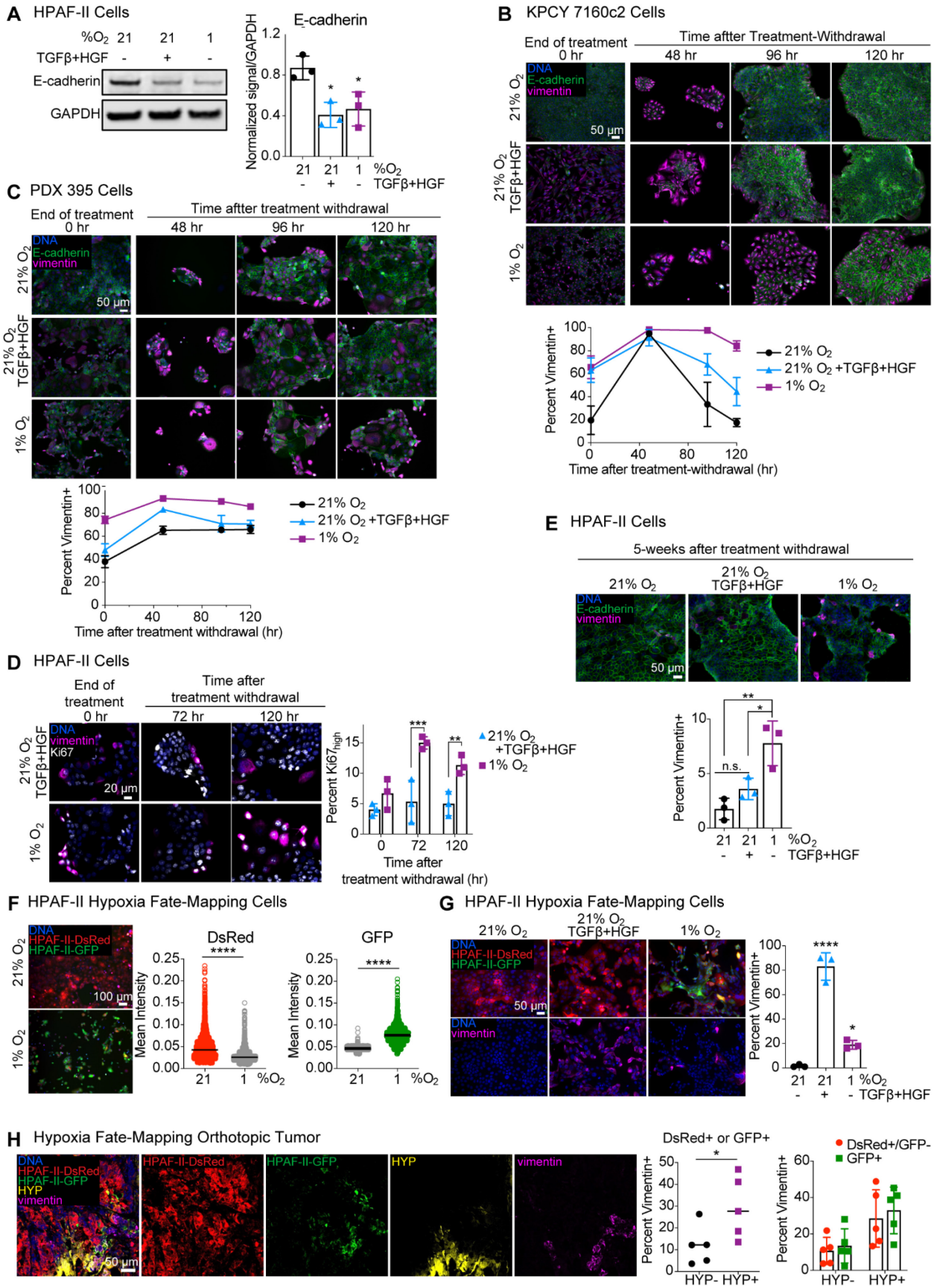
A HPAF-II Cells
%O2 21 21 1
TGFβ+HGF - + -
E-cadherin
GAPDH
E-cadherin
Normalized signal/GAPDH
1.2
0.8
0.4
0.0
21 21 1 %O2
- + - TGFβ+HGF
B KPCY 7160c2 Cells
End of treatment
0 hr
Time aftter Treatment-Withdrawal
48 hr
96 hr
120 hr
DNA
E-cadherin
vimentin
50 μm
21% O2
21% O2 TGFβ+HGF
1% O2
Percent Vimentin+
100
80
60
40
20
0
0 40 80 120
Time after treatment-withdrawal (hr)
21% O2
21% O2 +TGFβ+HGF
1% O2
C PDX 395 Cells
End of treatment
0 hr
Time aftter treatment withdrawal
48 hr
96 hr
120 hr
DNA
E-cadherin
vimentin
50 μm
21% O2
21% O2 TGFβ+HGF
1% O2
Percent Vimentin+
100
80
60
40
20
0
0 40 80 120
Time after treatment withdrawal (hr)
21% O2
21% O2 +TGFβ+HGF
1% O2
D HPAF-II Cells
End of treatment
0 hr
Time after treatment withdrawal
72 hr
120 hr
DNA
vimentin
Ki67
20 μm
21% O2 TGFβ+HGF
1% O2
Percent Ki67high
15
10
5
0
***
**
0 72 120
Time after treatment withdrawal (hr)
21% O2 +TGFβ+HGF
1% O2
E HPAF-II Cells
5-weeks after treatment withdrawal
21% O2
21% O2 TGFβ+HGF
1% O2
DNA
E-cadherin
vimentin
50 μm
Percent Vimentin+
10
5
0
**
*
n.s.
21 21 1 %O2
- + - TGFβ+HGF
F HPAF-II Hypoxia Fate-Mapping Cells
DNA
HPAF-II-DsRed
HPAF-II-GFP
100 μm
21% O2
1% O2
DsRed
****
Mean Intensity
0.25
0.20
0.15
0.10
0.05
0.00
21 1 %O2
GFP
****
Mean Intensity
0.25
0.20
0.15
0.10
0.05
0.00
21 1 %O2
G HPAF-II Hypoxia Fate-Mapping Cells
21% O2
21% O2 TGFβ+HGF
1% O2
DNA
HPAF-II-DsRed
HPAF-II-GFP
50 μm
DNA
vimentin
Percent Vimentin+
100
80
60
40
20
0
****
*
21 21 1 %O2
- + - TGFβ+HGF
H Hypoxia Fate-Mapping Orthotopic Tumor
DNA
HPAF-II-DsRed
HPAF-II-GFP
HYP
vimentin
50 μm
HPAF-II-DsRed
HPAF-II-GFP
HYP
vimentin
DsRed+ or GFP+
Percent Vimentin+
50
40
30
20
10
0
*
HYP- HYP+
DsRed+/GFP-
GFP+
Percent Vimentin+
60
40
20
0
HYP- HYP+

Supp Figure S7. Hypoxia-mediated EMT is more durable than growth factor-driven EMT. **(A)** HPAF-II cells were cultured in 21% O_2, with or without 10 ng/mL TGFβ + 50 ng/mL HGF or in 1% O_2 for 120 hr. Cells lysates were analyzed by immunoblotting for the indicated proteins. *n* = 3, one-way ANOVA with comparison to 21% O_2. **(B)** KPCY 7160c2 and **(C)** PDX 395 cells were cultured as described in (A). Cells were then re-plated and cultured in 21% O_2 without growth factors. At the indicated times, cells were fixed. Cells were stained with antibodies against the indicated proteins, and immunofluorescence microscopy was performed with quantitative image analysis for the percentage of vimentin-positive cells. *n* = 3, data represented as mean ± s.e.m. **(D)** HPAF-II cells were cultured in 21% O_2 with 10 ng/mL TGFβ + 50 ng/mL HGF or in 1% O_2 for 120 hr. Cells were then re-plated on coverslips and cultured in 21% O_2 without growth factors for up to 120 hr. At the indicated times after re-plating, cells were fixed, and immunofluorescence microscopy was performed for Ki67, *n* = 3, two-way ANOVA with Sidak's multiple comparisons test to compare the treatment conditions at each time point. **(E)** HPAF-II cells were treated and re-plated as described in panels (B) and (C). Five weeks after treatment-withdrawal, with passaging as needed to maintain cell health, cells were fixed and stained for the indicated proteins. Immunofluorescence microscopy with quantitative image analysis was performed. *n* = 3, one-way ANOVA with Tukey's multiple comparisons test across all groups. **(F)** HPAF-II engineered with the hypoxia fate-mapping system were cultured in 21% or 1% O_2 for 12 days. Live cells were imaged for DsRed or GFP expression, and quantification of each fluorescent protein per cell was performed. *n* = 3, t-test. **(G)** HPAF-II hypoxia fate-mapping cells were cultured as described in (A). *n* = 3, one-way ANOVA with Dunnett's multiple comparisons test against 21% O_2. **(H)** Fluorescent immunohistochemistry was performed on sections of orthotopic mouse tumors formed using HPAF-II hypoxia fate-mapping cells. Antibody staining for DsRed, GFP, vimentin, and Hypoxyprobe (HYP) was performed, followed by five-color confocal microscopy and quantitative image analysis. *n* = 5, with t test used to compare vimentin+ HPAF-II cells (DsRed+ or GFP+) that were HYP- or HYP+ and two-way ANOVA with Sidak's multiple comparison test used for a similar comparison where DsRed+/GFP- and GFP+ cells were split out separately. * $p < 0.05$, ** $p < 0.01$, *** $p < 0.001$, **** $p < 0.0001$

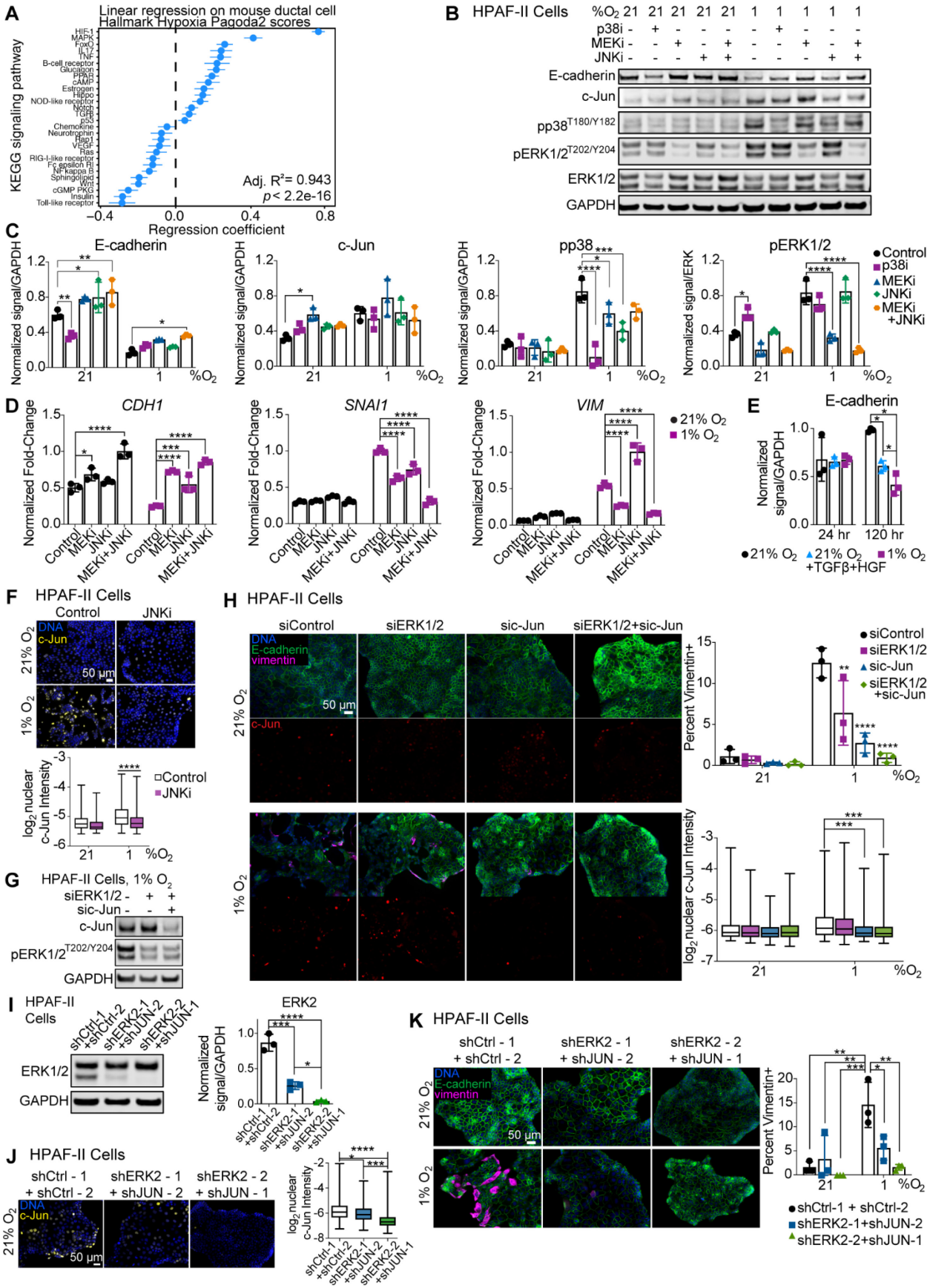
A
Linear regression on mouse ductal cell
Hallmark Hypoxia Pagoda2 scores
KEGG signaling pathway
Adj. R²= 0.943
p< 2.2e-16
Regression coefficient
B
HPAF-II Cells
%O2 21 21 21 21 21 1 1 1 1 1
p38i - + - - - - + - - -
MEKi - - + - + - - + - +
JNKi - - - + + - - - + +
E-cadherin
c-Jun
pp38T180/Y182
pERK1/2T202/Y204
ERK1/2
GAPDH
C
E-cadherin
c-Jun
pp38
pERK1/2
Normalized signal/GAPDH
Normalized signal/ERK
%O2
Control
p38i
MEKi
JNKi
MEKi +JNKi
D
CDH1
SNAI1
VIM
Normalized Fold-Change
21% O2
1% O2
Control
MEKi
JNKi
MEKi+JNKi
E
E-cadherin
Normalized signal/GAPDH
24 hr
120 hr
21% O2
21% O2 +TGFβ+HGF
1% O2
F
HPAF-II Cells
Control
JNKi
DNA
c-Jun
50 μm
log2 nuclear c-Jun Intensity
G
HPAF-II Cells, 1% O2
siERK1/2
sic-Jun
c-Jun
pERK1/2T202/Y204
GAPDH
H
HPAF-II Cells
siControl
siERK1/2
sic-Jun
siERK1/2+sic-Jun
DNA
E-cadherin
vimentin
c-Jun
50 μm
Percent Vimentin+
log2 nuclear c-Jun Intensity
I
HPAF-II Cells
shCtrl-1 +shCtrl-2
shERK2-1 +shJUN-2
shERK2-2 +shJUN-1
ERK1/2
GAPDH
ERK2
Normalized signal/GAPDH
J
HPAF-II Cells
shCtrl - 1 + shCtrl - 2
shERK2 - 1 + shJUN - 2
shERK2 - 2 + shJUN - 1
DNA
c-Jun
50 μm
log2 nuclear c-Jun Intensity
K
HPAF-II Cells
shCtrl - 1 + shCtrl - 2
shERK2 - 1 + shJUN - 2
shERK2 - 2 + shJUN - 1
DNA
E-cadherin
vimentin
50 μm
Percent Vimentin+
shCtrl-1 + shCtrl-2
shERK2-1+shJUN-2
shERK2-2+shJUN-1

Supp Figure S8. Hypoxia-driven EMT is MAPK-dependent. (A) Coefficients for the different KEGG signaling pathways are shown for the best LASSO+AIC-selected linear regression model of Hallmark Hypoxia Pagoda2 scores in mouse ductal cells. Pagoda2 scores for the indicated KEGG signaling pathways as the independent variables in the model. Error bars denote 95% confidence intervals for the indicated regression coefficient estimates. **(B,C)** HPAF-II cells were cultured in 21% or 1% O_2 with 10 μM SB203580 (p38i), 1 μM CI-1040 (MEKi), 10 μM SP600125 (JNKi), or DMSO for 120 hr, with inhibitors replenished every 48 hr. Cell lysates were analyzed by immunoblotting for the indicated proteins. *n* = 3, two-way ANOVA with Tukey's multiple comparison test against the DMSO (control) condition. **(D)** HPAF-II cells were treated as described in panel (C) with the indicated inhibitors. RNA was extracted, and qRT-PCR was performed for the indicated transcripts. *CASC3* was used as a control gene for normalization. *n* = 3, two-way ANOVA with Sidak's multiple comparison test against the untreated (control) condition. **(E)** HPAF-II cells were treated and lysed as described in Figure 4E and quantification was performed for E-cadherin. *n* = 3, one-way ANOVA with Tukey's multiple comparisons test at each time point. **(F)** HPAF-II cells were cultured for 120 hr in 21% or 1% O_2 with 10 μM SP600125 (JNKi) or DMSO, with inhibitor replenished every 48 hr. Cells were fixed and stained for c-Jun, and image analysis was performed. *n* =3, mixed-effects analysis with Tukey's multiple comparisons test. **(G)** HPAF-II cells were transfected with siRNA targeting ERK1/2 and c-Jun or control siRNA and cultured at 1% O_2 for 24 hr. Lysates were analyzed by immunoblotting for the indicated proteins. **(H)** HPAF-II cells were transfected with siRNA targeting ERK1/2 and/or c-Jun or control siRNA. 24 hr later, cells were switched to 1% O_2 or maintained at 21% O_2. 120 hr later, cells were fixed and stained with antibodies against the indicated proteins. Immunofluorescence microscopy was performed with quantitative image analysis for the indicated proteins. *n* = 3, two-way ANOVA for vimentin positivity and mixed-effects analysis for c-Jun expression, with Tukey's multiple comparisons test. **(I)** HPAF-II cells engineered to stably express *ERK2*- and *JUN*-targeting shRNAs or control shRNAs and were cultured in 21% O_2 for 24 hr. Lysates were analyzed by immunoblotting for the indicated proteins. *n* = 3, one-way ANOVA with Tukey's multiple comparisons test. **(J)** HPAF-II cells described in (I) were cultured for 120 hr in 21% O_2, and immunofluorescence microscopy was performed to quantify nuclear c-Jun. *n* = 3, mixed-effects analysis with Tukey's multiple comparisons test. **(K)** HPAF-II cells described in (I) were cultured in 21% or 1% O_2 for 120 hr, and immunofluorescence was performed using antibodies against the indicated proteins. *n* = 3, two-way ANOVA with Tukey's multiple comparisons test. * $p < 0.05$, ** $p < 0.01$, *** $p < 0.001$, **** $p < 0.0001$

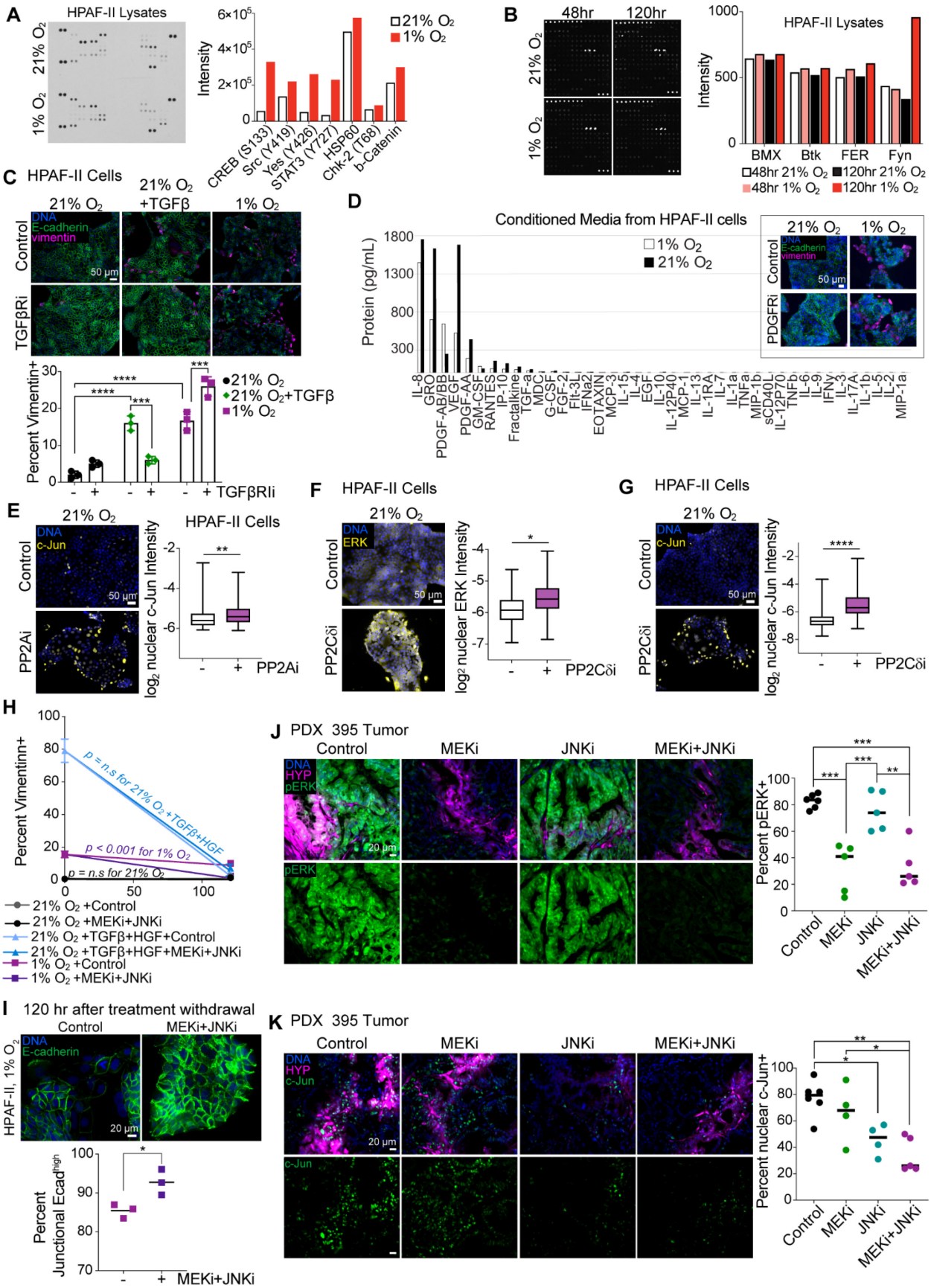
A
HPAF-II Lysates
21% O2
1% O2
Intensity
6×10^5
4×10^5
2×10^5
0
21% O2
1% O2
CREB (S133)
Src (Y419)
Yes (Y426)
STAT3 (Y727)
HSP60
Chk-2 (T68)
b-Catenin
B
48hr
120hr
21% O2
1% O2
HPAF-II Lysates
Intensity
1000
500
0
BMX
Btk
FER
Fyn
48hr 21% O2
120hr 21% O2
48hr 1% O2
120hr 1% O2
C
HPAF-II Cells
21% O2
21% O2 +TGFβ
1% O2
Control
TGFβRi
DNA
E-cadherin
vimentin
50 μm
Percent Vimentin+
30
20
10
0
****
***
21% O2
21% O2+TGFβ
1% O2
- + - + - + TGFβRIi
D
Conditioned Media from HPAF-II cells
Protein (pg/mL)
1800
1300
800
300
1% O2
21% O2
IL-8
GRO
PDGF-AB/BB
VEGF
PDGF-AA
GM-CSF
RANTES
IP-10
Fractalkine
TGF-a
MDC
G-CSF
FGF-2
Flt-3L
IFNa2
EOTAXIN
MCP-3
IL-15
IL-4
EGF
IL-10
IL-12P40
MCP-1
IL-13
IL-1RA
IL-7
IL-1a
TNFa
MIP-1b
sCD40L
IL-12P70
TNFb
IL-6
IL-9
IFNγ
IL-3
IL-17A
IL-1b
IL-5
IL-2
MIP-1a
21% O2
1% O2
Control
PDGFRi
DNA
E-cadherin
vimentin
50 μm
E
21% O2
HPAF-II Cells
Control
PP2Ai
DNA
c-Jun
50 μm
log2 nuclear c-Jun Intensity
-2
-4
-6
**
- + PP2Ai
F
HPAF-II Cells
21% O2
Control
PP2Cδi
DNA
ERK
50 μm
log2 nuclear ERK Intensity
-4
-5
-6
-7
*
- + PP2Cδi
G
HPAF-II Cells
21% O2
Control
PP2Cδi
DNA
c-Jun
50 μm
log2 nuclear c-Jun Intensity
-2
-4
-6
-8
****
- + PP2Cδi
H
Percent Vimentinn+
100
80
60
40
20
0
0
50
100
p = n.s for 21% O2 +TGFβ+HGF
p < 0.001 for 1% O2
p = n.s for 21% O2
21% O2 +Control
21% O2 +MEKi+JNKi
21% O2 +TGFβ+HGF+Control
21% O2 +TGFβ+HGF+MEKi+JNKi
1% O2 +Control
1% O2 +MEKi+JNKi
J
PDX 395 Tumor
Control
MEKi
JNKi
MEKi+JNKi
DNA
HYP
pERK
20 μm
pERK
Percent pERK+
100
80
60
40
20
0
***
***
***
**
Control
MEKi
JNKi
MEKi+JNKi
I
120 hr after treatment withdrawal
Control
MEKi+JNKi
HPAF-II, 1% O2
DNA
E-cadherin
20 μm
Percent Junctional Ecad^high
100
90
80
70
*
- + MEKi+JNKi
K
PDX 395 Tumor
Control
MEKi
JNKi
MEKi+JNKi
DNA
HYP
c-Jun
20 μm
c-Jun
Percent nuclear c-Jun+
100
80
60
40
20
0
**
*
*
Control
MEKi
JNKi
MEKi+JNKi

Supp Figure S9. Hypoxia-mediated EMT is MAPK- and SFK-dependent. (A) The Proteome Profiler Human Phospho-kinase Array (R&D Systems; 37 phosphorylated kinases and 2 total proteins) was used to analyze lysates from HPAF-II cells cultured for 120 hr in 21% or 1% O_2. Quantification for the top seven targets that were preferentially abundant in 1% O_2 is displayed. *n* = 1. **(B)** The Human Receptor Tyrosine Kinase Phosphorylation Array (RayBiotech; 71 targets) was used to analyze lysates from HPAF-II cells cultured for 48 or 120 hr in 21% or 1% O_2. Quantification for the top four targets that were preferentially abundant in 1% O_2 is displayed. *n* = 1. **(C)** HPAF-II cells cultured in 21% O_2 with or without 10 ng/mL TGFβ or in 1% O_2 were treated with 10 μM galunisertib (TGFβRIi) or DMSO. Immunofluorescence microscopy and quantitative image analysis was performed. *n* = 3, two-way ANOVA with Tukey's multiple comparisons test. **(D)** Luminex was performed on conditioned media from HPAF-II cells cultured for 120 hr at 21% or 1% O2. *n* = 1. Inset: To test the possible relevance of PDGF—AB/BB, HPAF-II cells cultured in 21% or 1% O_2 for 120 hr were treated with 1 μM CP-673451 (PDGFRi) or DMSO. Immunofluorescence microscopy was performed for the indicated proteins. **(E)** HPAF-II cells were cultured for 120 hr at 21% O_2 with 5 μM LB100 (PP2Ai) or DMSO, with inhibitors replenished every 48 hr. Cells were fixed and stained for c-Jun. Immunofluorescence microscopy was performed with image analysis for nuclear c-Jun expression. *n* = 3, mixed-effects analysis. **(F, G)** HPAF-II cells were cultured for 120 hr in 21% O_2 with 1.5 μM sanguinarine chloride (PP2Cδi) or DMSO, with inhibitors replenished every 48 hr. Cells were fixed and stained for c-Jun or ERK1/2. Immunofluorescence microscopy was performed with image analysis for nuclear c-Jun or nuclear ERK1/2. *n* = 3, mixed-effects analysis. **(H)** Rate of change in percent vimentin+ cells from Figure 5E. Comparisons were made against the control (DMSO) condition of fitted *y*-intercepts and slopes. The null hypothesis was that a single curve could capture both the control and MEKi+JNKi conditions. MEK and JNK inhibitors defined in Figure 5. The null hypothesis was only rejected for 1% O_2. **(I)** Immunofluorescence microscopy was performed with image analysis for junctional E-cadherin for HPAF-II cells cultured as in Figure 5E. *n* = 3, t test. **(J, K)** PDX 395 tumors were treated twice daily for nine days with selumetinib (MEKi), SP600125 (JNKi), selumetinib+SP600125, or vehicle control, as described in Figure 5F. Tumor sections were stained and quantified for percent **(J)** pERK+ or **(K)** nuclear c-Jun+ cells. *n* = 4 - 6, one-way ANOVA with Tukey's multiple comparisons test. * $p < 0.05$, ** $p < 0.01$, *** $p < 0.001$, **** $p < 0.0001$

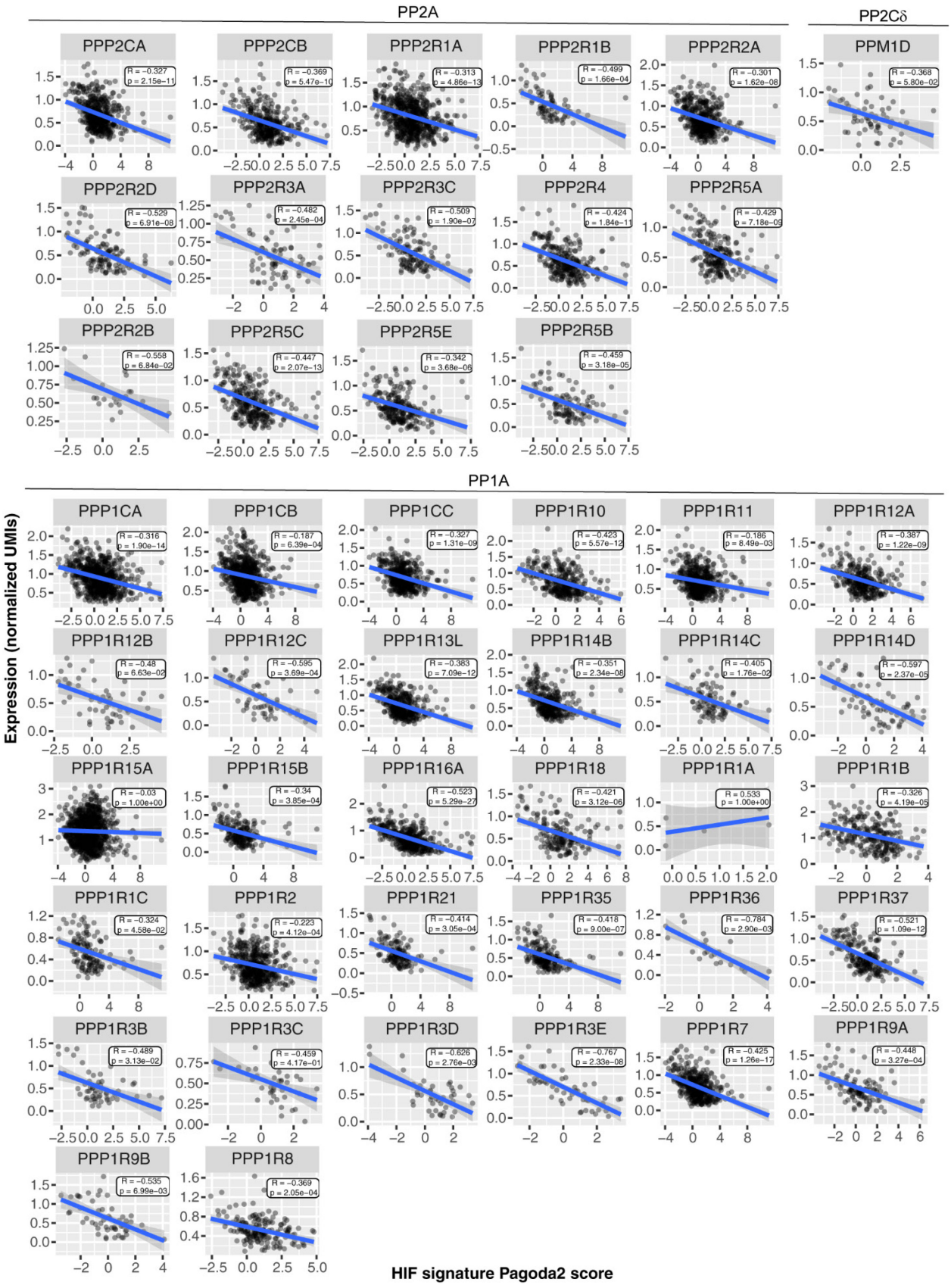
PP2A
PP2Cδ
PPP2CA
R = −0.327
p = 2.15e−11
PPP2CB
R = −0.369
p = 5.47e−16
PPP2R1A
R = −0.313
p = 4.86e−13
PPP2R1B
R = −0.499
p = 1.66e−04
PPP2R2A
R = −0.301
p = 1.62e−08
PPM1D
R = −0.368
p = 5.80e−02
PPP2R2D
R = −0.529
p = 6.91e−08
PPP2R3A
R = −0.482
p = 2.45e−04
PPP2R3C
R = −0.509
p = 1.90e−07
PPP2R4
R = −0.424
p = 1.84e−11
PPP2R5A
R = −0.429
p = 7.18e−09
PPP2R2B
R = −0.558
p = 6.84e−02
PPP2R5C
R = −0.447
p = 2.07e−13
PPP2R5E
R = −0.342
p = 3.68e−06
PPP2R5B
R = −0.459
p = 3.18e−05
PP1A
Expression (normalized UMIs)
PPP1CA
R = −0.316
p = 1.90e−14
PPP1CB
R = −0.187
p = 6.39e−04
PPP1CC
R = −0.327
p = 1.31e−09
PPP1R10
R = −0.423
p = 5.57e−12
PPP1R11
R = −0.186
p = 8.49e−03
PPP1R12A
R = −0.387
p = 1.22e−09
PPP1R12B
R = −0.48
p = 6.63e−02
PPP1R12C
R = −0.595
p = 3.69e−04
PPP1R13L
R = −0.383
p = 7.09e−12
PPP1R14B
R = −0.351
p = 2.34e−08
PPP1R14C
R = −0.405
p = 1.76e−02
PPP1R14D
R = −0.597
p = 2.37e−05
PPP1R15A
R = −0.03
p = 1.00e+00
PPP1R15B
R = −0.34
p = 3.85e−04
PPP1R16A
R = −0.523
p = 5.29e−27
PPP1R18
R = −0.421
p = 3.12e−06
PPP1R1A
R = 0.533
p = 1.00e+00
PPP1R1B
R = −0.326
p = 4.19e−05
PPP1R1C
R = −0.324
p = 4.58e−02
PPP1R2
R = −0.223
p = 4.12e−04
PPP1R21
R = −0.414
p = 3.05e−04
PPP1R35
R = −0.418
p = 9.00e−07
PPP1R36
R = −0.784
p = 2.90e−03
PPP1R37
R = −0.521
p = 1.09e−12
PPP1R3B
R = −0.489
p = 3.13e−02
PPP1R3C
R = −0.459
p = 4.17e−01
PPP1R3D
R = −0.626
p = 2.76e−03
PPP1R3E
R = −0.767
p = 2.33e−08
PPP1R7
R = −0.425
p = 1.26e−17
PPP1R9A
R = −0.448
p = 3.27e−04
PPP1R9B
R = −0.535
p = 6.99e−03
PPP1R8
R = −0.369
p = 2.05e−04
HIF signature Pagoda2 score

Supp Figure S10. PP2A, PP2Cδ, and PP1A subunits are negatively correlated with HIF signature in PDAC patient tumors. Pearson correlation coefficients were computed between HIF signature Pagoda2 enrichment scores and the mRNA expression data of PP2A, PP2Cδ, and PP1A subunits using previously published scRNA-seq data (6). Only cells with non-zero expression of the indicated genes were retained in these analyses. The statistical significance of each correlation is indicated by *p*.

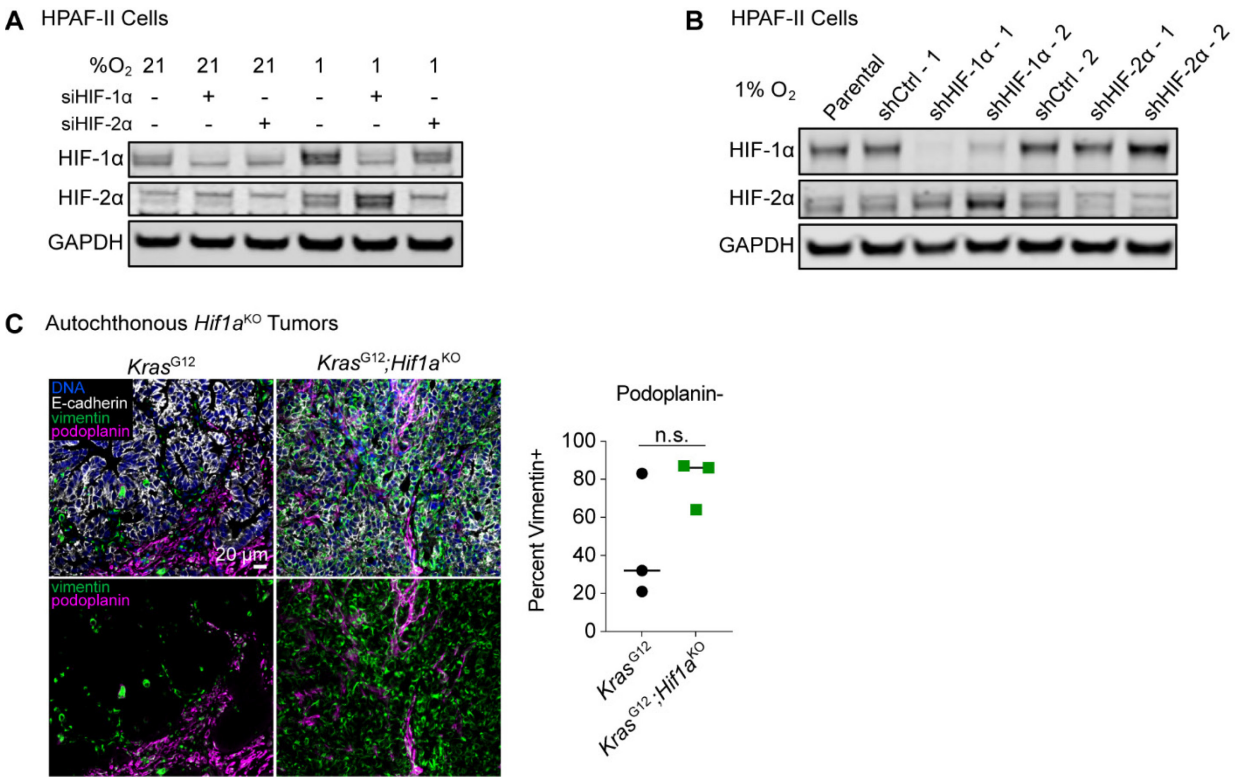

Supp Figure S11. HIFs are involved in hypoxia-mediated EMT but are not the sole regulators. (A) HPAF-II cells were transfected with siRNA targeting HIF-1α or HIF-2α or control siRNA. 24 hr later, cells were switched to 1% O_2 for 4 hr and lysed. Lysates were analyzed by immunoblotting for the indicated proteins. **(B)** HPAF-II cells engineered with stable shRNA-mediated knockdown of HIF-1α and HIF-2α or control shRNAs were cultured in 1% O_2 for 4 hr and lysed. Lysates were analyzed by immunoblotting for the indicated proteins. **(C)** Sections of pancreas tumors from mice harboring tissue-specific *Kras*^{G12D} and *Kras*^{G12D};*Hif1a*^{KO} mutations were stained for E-cadherin, vimentin, and podoplanin (fibroblast marker). Image analysis was performed for vimentin positivity in podoplanin-negative cells. *n* = 3, t test.

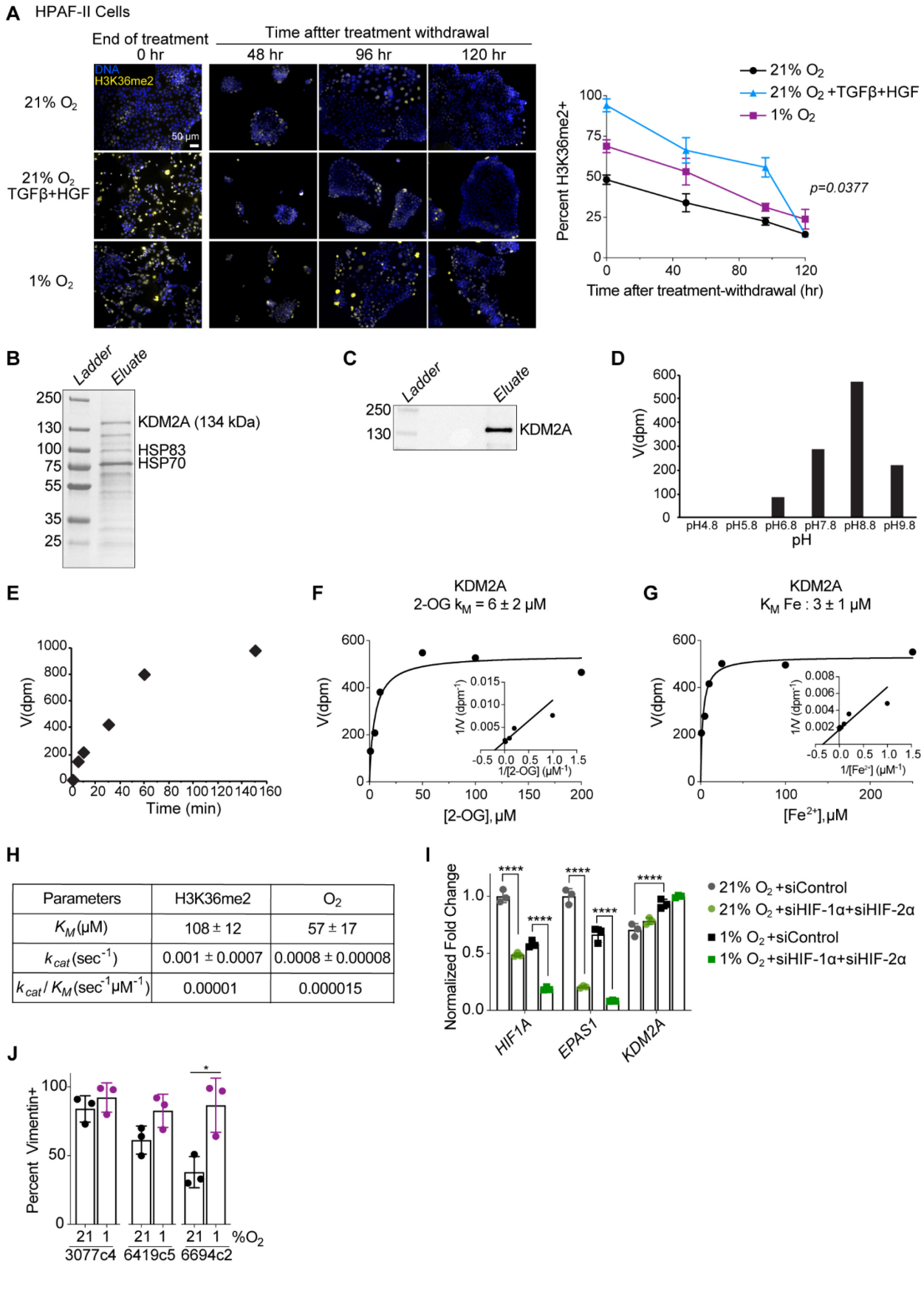
A
HPAF-II Cells
End of treatment
Time aftter treatment withdrawal
0 hr
48 hr
96 hr
120 hr
DNA
H3K36me2
21% O2
21% O2 TGFβ+HGF
1% O2
50 μm
21% O2
21% O2 +TGFβ+HGF
1% O2
Percent H3K36me2+
p=0.0377
Time after treatment-withdrawal (hr)
B
Ladder
Eluate
KDM2A (134 kDa)
HSP83
HSP70
C
Ladder
Eluate
KDM2A
D
V(dpm)
pH4.8 pH5.8 pH6.8 pH7.8 pH8.8 pH9.8
pH
E
V(dpm)
Time (min)
F
KDM2A
2-OG kM = 6 ± 2 μM
V(dpm)
1/V (dpm-1)
1/[2-OG] (μM-1)
[2-OG], μM
G
KDM2A
KM Fe : 3 ± 1 μM
V(dpm)
1/V (dpm-1)
1/[Fe2+] (μM-1)
[Fe2+], μM
H
Parameters | H3K36me2 | O2
KM (μM) | 108 ± 12 | 57 ± 17
kcat (sec-1) | 0.001 ± 0.0007 | 0.0008 ± 0.00008
kcat / KM (sec-1μM-1) | 0.00001 | 0.000015
I
Normalized Fold Change
HIF1A
EPAS1
KDM2A
21% O2 +siControl
21% O2 +siHIF-1α+siHIF-2α
1% O2 +siControl
1% O2 +siHIF-1α+siHIF-2α
J
Percent Vimentin+
%O2
3077c4
6419c5
6694c2

Supp Figure S12. H3K36 dimethylation and KDM2A activity are regulated by oxygen tension. (A) HPAF-II cells were cultured for 120 hr in 21% O_2 with or without 10 ng/mL TGFβ + 50 ng/mL HGF or in 1% O_2. Cells were then re-plated on coverslips and cultured in 21% O_2 without additional growth factors for up to 120 hr. Cells were fixed at the indicated times after re-plating. Cells were then stained with an H3K36me2 antibody, and immunofluorescence microscopy was performed with image analysis for percent H3K36me2-positive cells. $n = 3$, with data represented as mean ± s.e.m. $p = 0.0377$ for nonlinear regression with extra sum-of-squares F test comparing slopes. **(B)** SDS-PAGE with Coomassie blue staining was performed for recombinant FLAG-affinity purified sample containing KDM2A protein. **(C)** Immunoblotting was performed with anti-FLAG M2 antibody to confirm the protein was purified, with the middle lanes left empty. **(D)** Screening was performed to determine the optimum pH for measuring the kinetics of KDM2A-catalyzed reactions. pH 8.8 was selected based on this analysis. Where velocity (V) is reported as disintegration parts per minute (dpm). **(E)** The rate of KMD2A-catalyzed reaction was measured at multiple time points to determine the range over which linearity was maintained. A 30-min reaction time was selected based on this analysis. **(F-G)** Michaelis-Menten saturation curves with Lineweaver-Burk plots as insets are shown for the kinetic analysis of KDM2A-catalyzed reactions as a function of 2-oxoglutarate (2-OG) or Fe^{2+} concentration. Plots show data for one representative run, with solid lines corresponding to the model fits to the data shown. **(H)** For Figure 7B,C, the fitted values of the Michaelis constant (K_M) and enzyme turnover rate (k_{cat}) are shown. Values are mean ± standard deviation for $n = 3$ independent biochemical measurements. **(I)** HPAF-II cells were transfected with siRNA targeting HIF-1α and HIF-2α or a control siRNA. 24 hr later, cells were moved to 1% O_2 or maintained at 21% O_2 for 120 hr. RNA was extracted, and qRT-PCR was performed for *HIF1A, EPAS1,* and *KDM2A*. *CASC3* was used as a control gene for normalization. $n = 3$, two-way ANOVA with Tukey's multiple comparisons test. **(J)** KPCY-derived cell lines 3077c4, 6419c5, and 6694c2 were treated as described in Figure 7D, and quantification of vimentin was performed. $n = 3$, one-way ANOVA. * $p < 0.05$, **** $p < 0.0001$

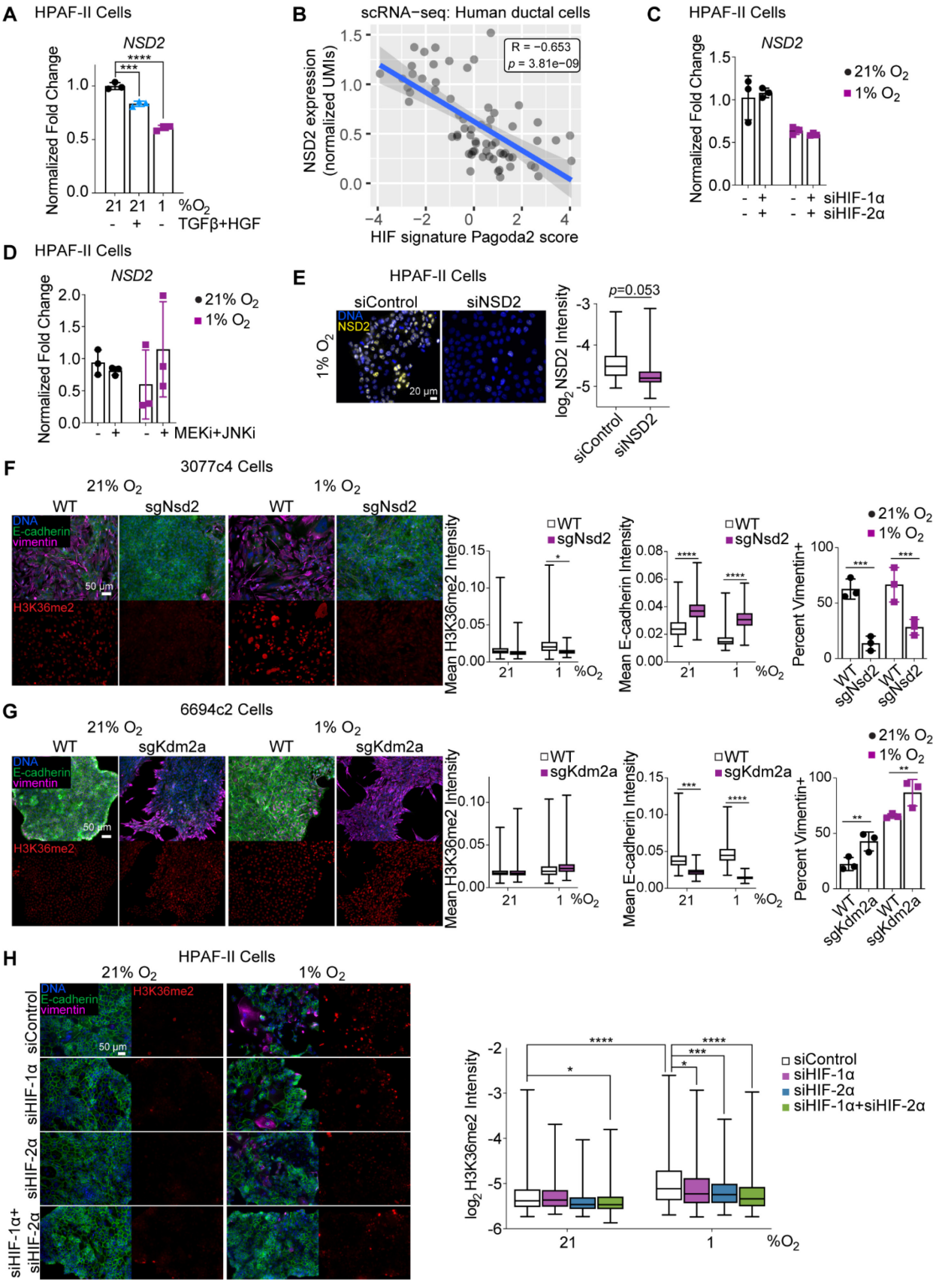
A
HPAF-II Cells
NSD2
Normalized Fold Change
****
***
21 21 1 %O2
- + - TGFβ+HGF
B
scRNA−seq: Human ductal cells
NSD2 expression (normalized UMIs)
R = −0.653
p = 3.81e−09
HIF signature Pagoda2 score
C
HPAF-II Cells
NSD2
21% O2
1% O2
siHIF-1α
siHIF-2α
D
HPAF-II Cells
NSD2
MEKi+JNKi
E
HPAF-II Cells
siControl
siNSD2
DNA
NSD2
1% O2
20 μm
p=0.053
log2 NSD2 Intensity
F
3077c4 Cells
21% O2
1% O2
WT
sgNsd2
DNA
E-cadherin
vimentin
H3K36me2
50 μm
Mean H3K36me2 Intensity
Mean E-cadherin Intensity
Percent Vimentin+
G
6694c2 Cells
sgKdm2a
H
HPAF-II Cells
siControl
siHIF-1α
siHIF-2α
siHIF-1α+ siHIF-2α
log2 H3K36me2 Intensity

Supp Figure S13. *NSD2* transcript expression is not HIF- nor MAPK-dependent, but Nsd2 or Kdm2a knockout impacts EMT in murine cells. (A) qRT-PCR was performed for *NSD2* mRNA from HPAF-II cells cultured in 21% O_2 with or without 10 ng/mL TGFβ + 50 ng/mL HGF or cultured in 1% O_2 for 120 hr. *CASC3* was used as a control gene for normalization. *n* = 3, one-way ANOVA with Tukey's multiple comparisons test. **(B)** The Pearson correlation coefficient was computed for the relationship between *NSD2* gene expression and HIF signature enrichment in human PDAC ductal cells using previously published scRNA-seq data (6). Only cells with non-zero expression of *NSD2* were retained in this analysis. **(C)** HPAF-II cells were transfected with siRNA targeting HIF-1α, HIF-2α, both HIFs, or control siRNA. 24 hr later, cells were moved to 1% O_2 or maintained at 21% O_2 for 120 hr. RNA was then extracted from cells, and qRT-PCR was performed for *NSD2*. *CASC3* was used as a control gene for normalization. *n* = 3. **(D)** qRT-PCR was performed for *NSD2* using RNA extracted from HPAF-II cells cultured for 120 hr in 21% or 1% O_2 with 1 μM CI-1040 (MEKi) and 10 μM SP600125 (JNKi) or DMSO. *CASC3* was used as a control gene for normalization. *n* = 3. **(E)** HPAF-II cells were transfected with siRNA targeting NSD2 or control siRNA. 24 hr later, cells were moved to 1% O_2 and maintained for 120 hr. Immunofluorescence microscopy was performed for nuclear NSD2. *n* = 3, mixed-effects analysis. **(F)** 3077c4 cells with *Nsd2* knockout, **(G)** 6694c2 cells with *Kdm2a* knockout, and their respective wild type counterparts were cultured for 120 hr in 21% or 1% O_2. Cells were then fixed and stained with antibodies for the indicated proteins, and immunofluorescence microscopy was performed with quantitative image analysis. *n* = 3, mixed effects analysis with Tukey's multiple comparison test. These KPCY-derived cell lines were described previously (7). **(H)** HPAF-II cells were transfected with siRNA targeting HIF-1α, HIF-2α, both HIFs, or control siRNA. 24 hr later, cells were moved to 1% O_2 or maintained at 21% O_2 for 120 hr. Cells were then fixed and stained with antibodies for the indicated proteins, and immunofluorescence microscopy with quantitative image analysis was performed. *n* = 3, one-way ANOVA with Tukey's multiple comparisons test. * $p < 0.05$, ** $p < 0.01$, *** $p < 0.001$, **** $p < 0.0001$

Supp Table S1. Software and algorithms

RESOURCE	IDENTIFIER	SOURCE OR REFERENCE
CPTAC Data via LinkedOmics	http://www.linkedomics.org/data_download/CPTAC-PDAC/	CPTAC
CPTAC Data via the Proteomic Data Commons	https://pdc.cancer.gov/pdc/browse/	CPTAC
TCGA PAAD RNA-seq Data	https://xenabrowser.net/datapages/?cohort=TCGA%20Pancreatic%20Cancer%20(PAAD)&removeHub=https%3A%2F%2Fxena.treehouse.gi.ucsc.edu%3A443	TCGA
R v4.1.2	https://www.r-project.org	R Development Core Team
Bioconductor v3.14	https://bioconductor.org/	(8)
clusterProfiler v4.0.5 (R package)	https://doi.org/doi:10.18129/B9.bioc.clusterProfiler	(9)
ComplexHeatmap v2.8.0 (R package)	https://doi.org/doi:10.18129/B9.bioc.ComplexHeatmap	(10)
ConsensusClusterPlus v1.56.0 (R package)	https://doi.org/doi:10.18129/B9.bioc.ConsensusClusterPlus	(11)
Cowplot v1.1.1 (R package)	https://wilkelab.org/cowplot/index.html	Claus O. Wilke
DreamAI v0.1.0 (R package)	https://github.com/WangLab-MSSM/DreamAI	(12)
EPIC v1.1.5 (R package)	https://github.com/GfellerLab/EPIC	(13)
ggplot2 v3.3.5 (R package)	https://rdocumentation.org/packages/ggplot2/versions/3.3.5	(14)
ggstatsplot v0.9.0 (R package)	https://www.rdocumentation.org/packages/ggstatsplot/versions/0.9.0	(15)
ggupset v0.3.0 (R package)	https://github.com/const-ae/ggupset	(16), Karl Dunkle Werner, Ahmadou Dicko, Antoine Bichat, Constantin
glmnet v4.1.-2 (R package)	https://rdocumentation.org/packages/glmnet/versions/4.1-2	(17)
GSVA v1.40.1 (R package)	https://doi.org/doi:10.18129/B9.bioc.GSVA	(18)
Hmisc v4.6-0 (R package)	https://github.com/harrelfe/Hmisc	Frank Harrell
immunedeconv v2.0.4 (R package)	https://github.com/icbi-lab/immunedeconv	(19)
msigdbr v7.4.1 (R package)	https://igordot.github.io/msigdbr/index.html	Igor Dolgalev
NMF v0.23.0 (R package)	https://www.rdocumentation.org/packages/NMF/versions/0.23.0	(20)
pagoda2 v1.0.6 (R package)	https://www.rdocumentation.org/packages/pagoda2/versions/1.0.6	(21)
survival v3.2-13 (R package)	https://rdocumentation.org/packages/survival/versions/3.2-13	Terry Therneau
Survminer v0.4.9 (R package)	https://rpkgs.datanovia.com/survminer/index.html	Alboukadel Kassambara, Marcin Kosinski, Przemyslaw Biecek
tidyHeatmap v1.3.1 (R package)	https://rdocumentation.org/packages/tidyHeatmap/versions/1.3.1	(22)

Supp Table S2. KEGG Signaling Pathways

KEGG Signaling Pathways		
Adipocytokine	HIF-1	PPAR
AMPK	Hippo	Prolactin
Apelin	IL-17	Rap1
B cell Receptor	Insulin	Ras
C-type lectin receptor	JAK-STAT	Relaxin
Calcium	MAPK	RIG-I-like Receptor
cAMP	mTOR	Sphingolipid
cGMP-PKG	Neurotrophin	T cell Receptor
Chemokine	NF-kappa B	TGF-beta
ErbB	NOD-like Receptor	TNF
Estrogen	Notch	Toll and IMD
Fc epsilon RI	Oxytocin	Toll-like Receptor
FoxO	p53	Thyroid hormone
Glucagon	Phospholipase D	VEGF
GnRH	PI3K-Akt	Wnt
Hedgehog		

Supp Table S3. qRT-PCR Primers

Target		Sequence (5' → 3')
CASC3	Forward	ACCTCGGAAAGGGCTCTTCTT
	Reverse	CGACCCTCATCCTTCCATAGC
CDH1	Forward	CATCAGGCCTCCGTTTCTG
	Reverse	GGAGTTGGGAAATGTGAGCA
VIM	Forward	TCTCTGAGGCTGCCAACCG
	Reverse	CGAAGGTGACGAGCCATTTCC
SNAI1	Forward	CTTCCAGCAGCCCTACGAC
	Reverse	CGGTGGGGTTGAGGATCT
TWIST1	Forward	CGGGAGTCCGCAGTCTTA
	Reverse	TGAATCTTGCTCAGCTTGTC
HIF1A	Forward	TGCTCATCAGTTGCCACTTC
	Reverse	TCCTCACACGCAAATAGCTG
EPAS1	Forward	GCGCTAGACTCCGAGAACAT
	Reverse	TGGCCACTTACTACCTGACCCTT
PGK1	Forward	AAGTCGGTAGTCCTTATGAGC
	Reverse	CACATGAAAGCGGAGGTTCT
SLC2A1	Forward	AGGTGATCGAGGAGTTCTAC
	Reverse	TCAAAGGACTTGCCCAGTTT
PPP1CA	Forward	GCTGCTGGCCTATAAGATCAA
	Reverse	GTCTCTTGCACTCATCGTAGAA
PPP2R2B	Forward	TGCAGCTTACTTTCTTCTGTCT
	Reverse	GTAGCCTTCTGGCCTCTTATC
PPM1D	Forward	CCTGTTAGAAGGAGCACAGTTAT
	Reverse	GTTCAGGTGACACCACAAATTC
PPP2CA	Forward	TGGAGCCTCAGCGAGCGGAG
	Reverse	GGCTCTTGACCTGGGACTCGGACAG
KDM2A	Forward	CCGATTGTGTCAGGAGCCAG
	Reverse	CACAGGACTGCTTCATGCGTC
NSD2	Forward	CCCACCATACAAGCACAT
	Reverse	TCAGACACTCCGAATCAAA

ADDITIONAL SUPPLEMENTAL METHODOLOGICAL REFERENCES

UMAP (23)

Molecular Signatures Database (MSigDB) hallmark gene set collection (24)

Kyoto Encyclopedia of Genes and Genomes (KEGG) (25,26)

Pathway and gene set overdispersion analysis (Pagoda2) (27,28)

NMF algorithm based on the Kullback-Leibler divergence (29)

Dispersion coefficient of the consensus matrix (30)

Average silhouette width (31)

Multiple comparisons testing (32)

Tumor dissociation (33)

Patient-derived xenograft model (3,34)

KPCY lineage-traced mouse model of PDAC (35-37)

SUPPLEMENTARY REFERENCES (from supplementary methods, figures, and tables)

1. Cao L, Huang C, Cui Zhou D, Hu Y, Lih TM, Savage SR*, et al.* Proteogenomic characterization of pancreatic ductal adenocarcinoma. Cell **2021**;184:5031-52 e26
2. Buonato JM, Lan IS, Lazzara MJ. EGF augments TGFbeta-induced epithelial-mesenchymal transition by promoting SHP2 binding to GAB1. J Cell Sci **2015**;128:3898-909
3. Walters DM, Stokes JB, Adair SJ, Stelow EB, Borgman CA, Lowrey BT*, et al.* Clinical, molecular and genetic validation of a murine orthotopic xenograft model of pancreatic adenocarcinoma using fresh human specimens. PLoS One **2013**;8:e77065
4. Laukka T, Myllykoski M, Looper RE, Koivunen P. Cancer-associated 2-oxoglutarate analogues modify histone methylation by inhibiting histone lysine demethylases. J Mol Biol **2018**;430:3081-92
5. Mak MP, Tong P, Diao L, Cardnell RJ, Gibbons DL, William WN*, et al.* A Patient-Derived, Pan-Cancer EMT Signature Identifies Global Molecular Alterations and Immune Target Enrichment Following Epithelial-to-Mesenchymal Transition. Clin Cancer Res **2016**;22:609-20
6. Elyada E, Bolisetty M, Laise P, Flynn WF, Courtois ET, Burkhart RA*, et al.* Cross-Species Single-Cell Analysis of Pancreatic Ductal Adenocarcinoma Reveals Antigen-Presenting Cancer-Associated Fibroblasts. Cancer Discov **2019**;9:1102-23
7. Yuan S, Natesan R, Sanchez-Rivera FJ, Li J, Bhanu NV, Yamazoe T*, et al.* Global Regulation of the Histone Mark H3K36me2 Underlies Epithelial Plasticity and Metastatic Progression. Cancer Discov **2020**;10:854-71
8. Huber W, Carey VJ, Gentleman R, Anders S, Carlson M, Carvalho BS*, et al.* Orchestrating high-throughput genomic analysis with Bioconductor. Nat Methods **2015**;12:115-21
9. Wu T, Hu E, Xu S, Chen M, Guo P, Dai Z*, et al.* clusterProfiler 4.0: A universal enrichment tool for interpreting omics data. Innovation (N Y) **2021**;2:100141
10. Gu Z, Eils R, Schlesner M. Complex heatmaps reveal patterns and correlations in multidimensional genomic data. Bioinformatics **2016**;32:2847-9
11. Wilkerson MD, Hayes DN. ConsensusClusterPlus: a class discovery tool with confidence assessments and item tracking. Bioinformatics **2010**;26:1572-3
12. Ma W, Kim S, Chowdhury S, Li Z, Yang M, Yoo S*, et al.* DreamAI: algorithm for the imputation of proteomics data. bioRxiv **2021**
13. Racle J, de Jonge K, Baumgaertner P, Speiser DE, Gfeller D. Simultaneous enumeration of cancer and immune cell types from bulk tumor gene expression data. Elife **2017**;6
14. Wickham H. 2016 ggplot2: Elegant Graphics for Data Analysis. Springer-Verlag New York.
15. Patil I. Visualizations with statistical details: The 'ggstatsplot' approach. Journal of Open Source Software **2021**;6:3167
16. Lex A, Gehlenborg N, Strobelt H, Vuillemot R, Pfister H. UpSet: Visualization of Intersecting Sets. IEEE Trans Vis Comput Graph **2014**;20:1983-92
17. Friedman J, Hastie T, Tibshirani R. Regularization Paths for Generalized Linear Models via Coordinate Descent. J Stat Softw **2010**;33:1-22
18. Hanzelmann S, Castelo R, Guinney J. GSVA: gene set variation analysis for microarray and RNA-seq data. BMC Bioinformatics **2013**;14:7
19. Sturm G, Finotello F, Petitprez F, Zhang JD, Baumbach J, Fridman WH*, et al.* Comprehensive evaluation of transcriptome-based cell-type quantification methods for immuno-oncology. Bioinformatics **2019**;35:i436-i45

20. Gaujoux R, Seoighe C. A flexible R package for nonnegative matrix factorization. BMC Bioinformatics **2010**;11:367
21. Lake BB, Chen S, Sos BC, Fan J, Kaeser GE, Yung YC*, et al.* Integrative single-cell analysis of transcriptional and epigenetic states in the human adult brain. Nat Biotechnol **2018**;36:70-80
22. Mangiola S, Papenfuss A. tidyHeatmap: an R package for modular heatmap production based on tidy principles. Journal of Open Source Software **2020**;5:2472
23. McInnes L, Healy J, Melville J. 2018 UMAP: Uniform Manifold Approximation and Projection for Dimension Reduction. arXiv <https://arxiv.org/abs/1802.03426>.
24. Liberzon A, Birger C, Thorvaldsdottir H, Ghandi M, Mesirov JP, Tamayo P. The Molecular Signatures Database (MSigDB) hallmark gene set collection. Cell Syst **2015**;1:417-25
25. Kanehisa M, Furumichi M, Tanabe M, Sato Y, Morishima K. KEGG: new perspectives on genomes, pathways, diseases and drugs. Nucleic Acids Res **2017**;45:D353-D61
26. Kanehisa M, Goto S. KEGG: kyoto encyclopedia of genes and genomes. Nucleic Acids Res **2000**;28:27-30
27. Zhang Y, Ma Y, Huang Y, Zhang Y, Jiang Q, Zhou M*, et al.* Benchmarking algorithms for pathway activity transformation of single-cell RNA-seq data. Comput Struct Biotechnol J **2020**;18:2953-61
28. Fan J, Salathia N, Liu R, Kaeser GE, Yung YC, Herman JL*, et al.* Characterizing transcriptional heterogeneity through pathway and gene set overdispersion analysis. Nat Methods **2016**;13:241-4
29. Brunet JP, Tamayo P, Golub TR, Mesirov JP. Metagenes and molecular pattern discovery using matrix factorization. Proc Natl Acad Sci U S A **2004**;101:4164-9
30. Kim H, Park H. Sparse non-negative matrix factorizations via alternating non-negativity-constrained least squares for microarray data analysis. Bioinformatics **2007**;23:1495-502
31. Rousseeuw P. Silhouettes: A graphical aid to the interpretation and validation of cluster analysis. Journal of Computational and Applied Mathematics **1987**;20:53-65
32. Benjamini Y, Hochberg Y. Controlling the False Discovery Rate: A Practical and Powerful Approach to Multiple Testing. Journal of the Royal Statistical Society **1995**;57:289-300
33. Adam M, Potter AS, Potter SS. Psychrophilic proteases dramatically reduce single-cell RNA-seq artifacts: a molecular atlas of kidney development. Development **2017**;144:3625-32
34. Michaels AD, Newhook TE, Adair SJ, Morioka S, Goudreau BJ, Nagdas S*, et al.* CD47 Blockade as an Adjuvant Immunotherapy for Resectable Pancreatic Cancer. Clin Cancer Res **2018**;24:1415-25
35. Li J, Byrne KT, Yan F, Yamazoe T, Chen Z, Baslan T*, et al.* Tumor Cell-Intrinsic Factors Underlie Heterogeneity of Immune Cell Infiltration and Response to Immunotherapy. Immunity **2018**;49:178-93 e7
36. Aiello NM, Maddipati R, Norgard RJ, Balli D, Li J, Yuan S*, et al.* EMT Subtype Influences Epithelial Plasticity and Mode of Cell Migration. Dev Cell **2018**;45:681-95 e4
37. Norgard RJ, Pitarresi JR, Maddipati R, Aiello-Couzo NM, Balli D, Li J*, et al.* Calcium signaling induces a partial EMT. EMBO Rep **2021**:e51872